ELECTROMAGNETIC CONTROL OF ELASTOMER FERROMAGNET COMPOSITE COMPONENTS FOR AUTOMOTIVE VIBRATION DAMPING

by

Nakul Verma
B.A.Sc., Simon Fraser University 2001

THESIS SUBMITTED IN PARTIAL FULFILLMENT OF
THE REQUIREMENTS FOR THE DEGREE OF

MASTER OF APPLIED SCIENCE

In the School
of
Engineering Science

SIMON FRASER UNIVERSITY

Spring 2006

APPROVAL

Name: Nakul Verma

Degree: Master of Applied Science

Title of Thesis: Electromagnetic Control of Elastomer Ferromagnet Composite Components for Automotive Vibration Damping

Examining Committee:

Chair: **Dr. Karim S. Karim**
Assistant Professor,
School of Engineering Science

Dr. Ash M. Parameswaran
Senior Supervisor
Professor,
School of Engineering Science

Dr. Andrew Rawicz
Supervisor
Professor,
School of Engineering Science

Dr. Shahram Payandeh
Internal Examiner
Professor,
School of Engineering Science

Date Defended/Approved: Apr. 12/06

ABSTRACT

The use of semi-active magnetorheological elastomer bushings in automobiles is one of many strategies to reduce vibration inside vehicles caused by structure-borne noise. However, several practical engineering challenges must be addressed before magnetorheological bushings can be seamlessly incorporated into vehicles.

This thesis comprises two projects that address some of the engineering challenges associated with practical implementation of magnetorheological bushings in cars. The first project investigates the dynamic vibration damping range of an elastomer ferromagnet composite damper, a type of magnetorheological material, under realizable electromagnetic control. The dynamic vibration damping range of the elastomer ferromagnet damper is acquired from the resonant frequency change of a vibrated proof mass comprising the elastomer ferromagnet component and a pair of off-the-shelf industrial electromagnets. The second project in this thesis models power amplifiers that are needed to power electromagnets coupled to magnetorheological bushings in an automobile.

Keywords: Magnetorheological Elastomers, Elastomer Ferromagnet Composite, Electromagnet Power Amplifiers, Sliding Mode Control

DEDICATION

To my parents and grandfather: Mr. Vinod Verma, Mrs. Anita Verma, and Mr. Ved Prakash; the only real heroes in my life.

ACKNOWLEDGEMENTS

- Dr. Ash M. Parameswaran for providing the opportunity of a lifetime, offering encouragement, for being an exceptionally patient supervisor
- Dr. Andrew Rawicz, and Dr. Shahram Payandeh for agreeing to be on my committee
- Dr. Karim for agreeing to be chair person on my committee
- Mike Sjoerdsma, my friend for starting us on an amazing project, teaching me Olympic style weight lifting, for the opportunity to go see Europe, and for painstakingly editing the first draft of my thesis
- Florian Schneider, for all his help with implementing my experimental setup
- Paul Sikora and David Miller, for offsite equipment access
- Geoff Mullins, for his help with mathematical modelling
- Hanjin Cho, for use of his home made vacuum chamber
- Bill Woods, Lynn Kool, Christine Poulin, Raj Pabla, Karen Hawthorne, and Julie Beth Fernandez, for all the help and favours over the years I cannot even begin to count up
- Bartek, Sasha and Ken in Dr. Heinrich's research group in the physics department.
- Dr. Sabir Asadov, for equipment usage and help with machining
- Rob Johstone, Ian Foulds and all my other lab friends for their friendship and all the remarkable conversations
- Golnaz Sanaie and Tony Ottaviani for their friendship and support

TABLE OF CONTENTS

LIST OF FIGURES

LIST OF TABLES

LIST OF EQUATIONS

LIST OF ACRONYMS

DAQ – Data Acquisition

DMM – Digital Multi Meter

EFC – Elastomer Ferromagnet Composite

MOSFET – Metal Oxide Semiconductor Field Effect Transistor

MR – Magnetorheological

mMRE – Magnetorheological Elastomer cured in magnetic field

MRE – Magnetorheological Elastomer

nMRE – Magnetorheological Elastomer cured without magnetic field

PID – Proportional Integral Derivative

PWM – Pulse Width Modulation

1 VIBRATION DAMPING WITH MAGNETORHEOLOGICAL COMPONENTS

1.1 Introduction

The renewed emphasis on fuel efficiency in recent years has driven automobile manufactures to build lighter cars [1]. With the use of lighter chassis and body materials, such as aluminium and carbon fibre [2-5], car manufacturers are keenly focussed on increasing fuel efficiency without compromising vehicle handling and performance. However, these innovations have certain drawbacks. Using lighter chassis materials, in particular, makes vehicles more susceptible to structure-borne noise, which varies in frequency from 0.5Hz to 50Hz [59]. Vibration can be damped out with vibration absorbing materials inside the car cabin; however, passively damping out structure-borne noise requires unrealistically large quantities of vibration absorbing materials in the car cabin [9]. Therefore, structure-borne noise in the car cabin is reduced by active and semi-active suspension systems that try to cancel out incoming structure-borne noise or by semi-active suspension systems that limit the amount of structure-borne borne noise coupled into the car cabin.

As members of the Auto 21 Network Centre of Excellence (www.auto21.ca), our research focuses on using elastomer ferromagnet composite (EFC) and magnetorheological elastomer (MRE) materials in semi-active systems that reduce structure-borne noise in cars. We have already examined the vibration damping capabilities of permanent magnet controlled magnetorheological elastomer (MRE)

components [6]. This thesis examines the vibration damping capabilities of electromagnetically controlled EFC components.

1.2 Reducing Structure-borne Noise

Often colloquially referred to as 'road noise', structure-borne noise [7] is the direct result of the contact between a vehicle's tires and the road surface. This noise is coupled into the vehicle cabin from the tires through the vehicle suspension. Along with other disturbances, such as engine noise [8], structure-borne noise contributes to driver fatigue and discomfort. Using absorbent materials to dampen structure-borne noise is impractical because the physical dimension of the absorbent material must be proportional to the wavelength of the structure borne noise. For example, it would take 2.5m of sound damping material inside the car cabin to damp out 200Hz noise [9]. Therefore, structure-borne noise damping requires active noise cancellation techniques that work inside the car cabin [10, 11] or, active and semi-active suspension systems that eliminate or limit the structure-borne noise coupled into the car cabin.

1.2.1 Active Suspension Systems

Most automobile suspension systems, consisting of spring and damper elements, inherently compromise between ride comfort and vehicle handling [12]. The structure of a passive suspension system is illustrated in Figure 1.1.

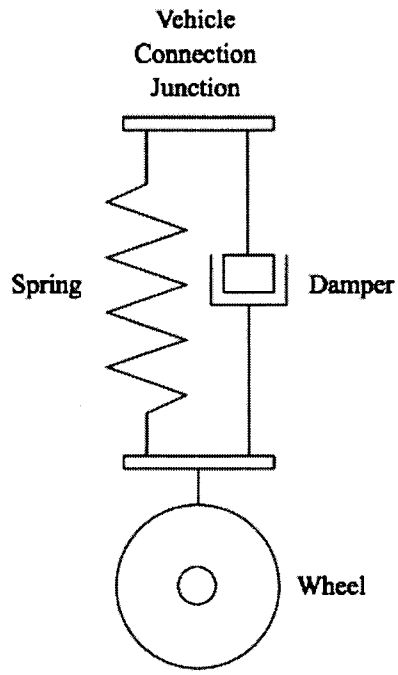

Figure 1.1: Automobile Passive Suspension

A stiff suspension will yield excellent handling but poor reduction of structure-borne noise in the vehicle cabin, whereas a softer suspension significantly reduces in-cabin structure-borne noise at the expense of vehicle handling. By adding an actuator to the spring and damper elements of a passive suspension system, an active suspension system overcomes the handling versus structure-borne noise reduction compromise inherent to a passive suspension system [15]. Depending on the element configuration, active suspension systems come in high bandwidth and low bandwidth varieties as illustrated in Figure 1.2.

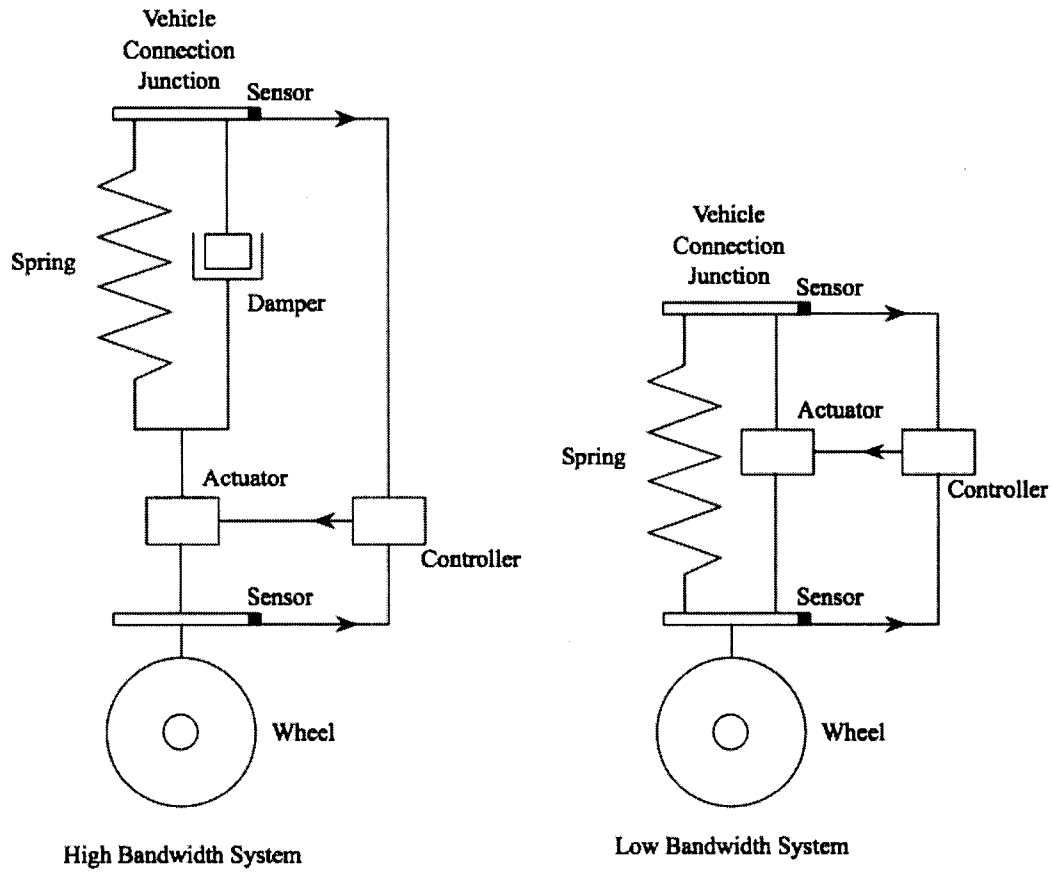

Figure 1.2: High and Low Bandwidth Active Suspension Systems

As illustrated in Figure 1.2 the high bandwidth active suspension system includes an actuator in series with a spring and damper in parallel, whereas the low bandwidth active suspension system omits the damper and replaces it with the actuator. Note that both active suspension configurations require sensors and controllers to properly control the actuator. To simplify implementation low bandwidth systems are preferable for automobiles because the high bandwidth systems require extremely sophisticated aerospace technology [13].

Although active suspension systems overcome problems associated with passive suspension systems, they do come with their own caveats. Issues regarding system

complexity and power consumption [14, 15] must be addressed before active suspensions become ubiquitous in vehicles. Also, without proper attention to controller design, active suspension systems can become unstable [12].

1.2.2 Semi-active Suspension Systems

Similar to active suspension systems, semi-active suspension systems replace the damper element of a passive suspension system with a variable damper element; i.e., a damper with a controllable damping coefficient. Semi-active suspension systems have the same advantages as active suspension systems, but without the added burden of excess power consumption [16]. Also, because semi-active suspension systems work by varying the energy absorbed by the suspension system [17, 18], they are always stable, unlike active suspension systems, which work by injecting energy into the suspension system.

Past research [19] with an electro-rheological fluid damper has demonstrated the capability of suspensions with variable damping characteristics. Also, Rakheja et al. [20] observed that the acceleration of the mass, in a spring-damper vibration system with a variable damper, increased when the damping force was in the same direction as the spring force.

1.3 Semi-active Bushings

Reducing structure-borne noise after it has propagated through the suspension of a car, shown in Figure 1.3, is an extremely difficult task. The structure-borne noise spectrum is illustrated by the frequency response, shown in Figure 1.4, of an experimental quarter car model [61] subjected to vibration from a shaker table.

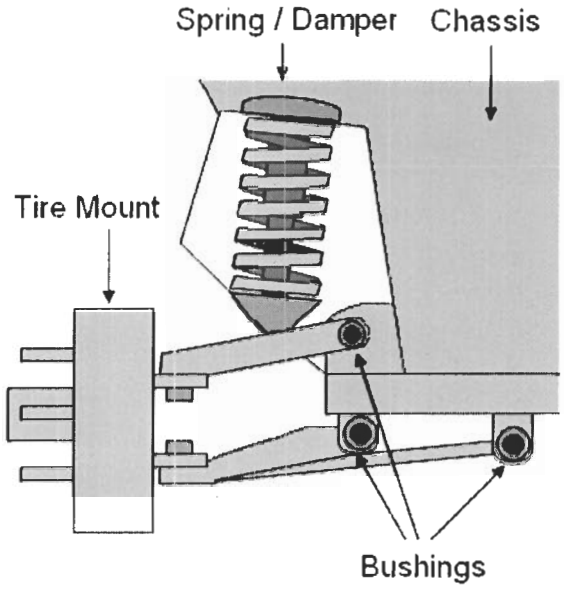

[6] © Michael Sjoerdsma, reproduced with permission

Figure 1.3: Bushings in the Suspension-Chassis Interface

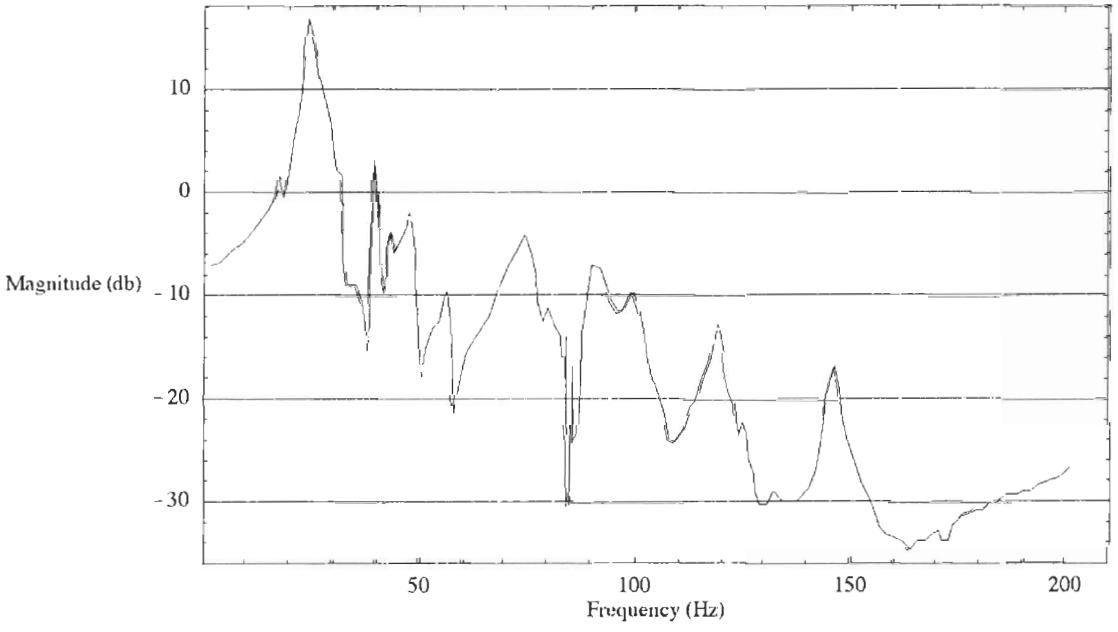

Figure 1.4: Quarter Car Model Frequency Response to Vibration [61]

Contributing factors such as tire mechanics, the suspension spring and damper elements, the suspension mounting bushings, as well as the inter-coupling between the suspension arms all effect structure-borne noise coupled into the car cabin. Because each of these contributing factors is a field of study in and of itself, as members of the vibration sub-group in the Auto21 intelligent systems group, we decided to narrow our research focus exclusively to the bushings that mate the suspension to the vehicle chassis.

The bushings that mate the suspension to the car chassis also affect structure-borne noise coupling [21]. Made mostly of rubber in commercial vehicles, bushings suffer from the same compromise as passive suspensions; i.e., a stiff bushing will yield excellent handling but poor reduction of structure-borne noise in the vehicle cabin, whereas a softer bushing significantly reduces in-cabin structure-borne noise at the expense of vehicle handling. Even if a vehicle is outfitted with an active or semi-active suspension system, the bushings will still transmit structure-borne noise into the cabin.

Rather than directly addressing the structure-borne noise problem, our research is motivated by the structure borne noise problem and focuses on vibration damping with semi-active materials. The eventual goal of our research would be to build semi-active bushings that can reduce structure-borne noise coupled through a car suspension. The initial phase of our research was conducted primarily by Mr. Michael Sjoerdsma [6].

1.4 Vibration Damping with MRE Components

Magnetorheological elastomers (MRE) are usually made of iron or iron alloy particles suspended in a rubber matrix [26]. Because MRE component stiffness can be reversibly controlled or altered, the natural frequency of a mechanical system

incorporating an MRE component can be dynamically changed [22]. Lokander et al. [23] experimentally determined that the greatest change in rheology occurs in nitrile rubber MRE components that contain 30% iron by volume. Increasing the iron content past 30% increases the stiffness of the resulting elastomer [24] beyond the maximum stiffness generated from an applied magnetic field [25].

1.4.1 MRE Theory of Operation

MRE components are created by curing the raw rubber and iron particle suspension in a magnetic field. The magnetic field is applied transverse to the intended axis of compression of the finished MRE component [26]. The applied magnetic field aligns the iron particles into chain like structures that are preserved after curing. By modelling the interaction between resident iron particles in the cured MRE and an external magnetic field, Borcea et al. [27] have shown that the cured MRE will overall compress while still elongating in the direction parallel to the applied magnetic field. They have also shown that the cured MRE strain perpendicular to the applied magnetic field is different from the cured MRE strain parallel to the applied magnetic field. Therefore, application of a magnetic field to the cured MRE component causes a change in modulus of elasticity, which in turn affects MRE component stiffness.

1.4.2 MRE Experimental Setup

The applicability of MRE components for bushings was initially investigated by fabricating two separate blocks designated as mMRE and nMRE [6]. The mMRE block was cured in a magnetic field perpendicular to the direction of vibration excitation in the experimental test jig, and the nMRE block was cured without a magnetic field. MRE

components that are cured without a magnetic field are classified as elastomer ferromagnet composite (EFC) components [30]. Both blocks were made of Sylgard Brand 184 silicone elastomer and mixed with Alfa Aesar stock #00736 iron powder. An illustration of both the mMRE and nMRE blocks is shown in Figure 1.5.

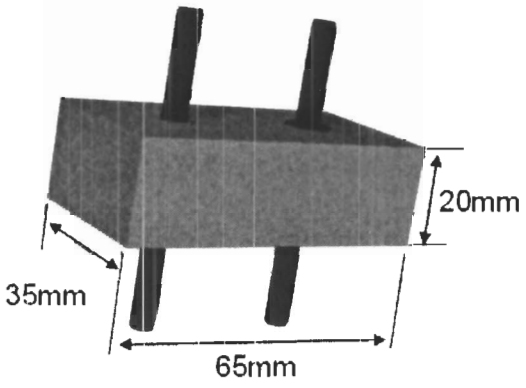

[6] © Michael Sjoerdsma, reproduced with permission

Figure 1.5: Fabricated mMRE and nMRE Blocks

The screws protruding from the top and bottom of the MRE block were used to mount the block into the experimental test jig. The experimental test jig comprised a shaker table (B&K Type 4808 Vibration Exciter) , a proof mass, four permanent magnets (Lee Valley 99K32.11) , and a pair of accelerometers (Analog Devices ADXL210). The MRE block was mounted on a bracket on the shaker table and the proof mass was mounted on a second bracket on top of the MRE block. The bracket on top of the MRE block also had space for holding the permanent magnets. A cross sectional diagram of the complete experimental test jig is illustrated in Figure 1.6.

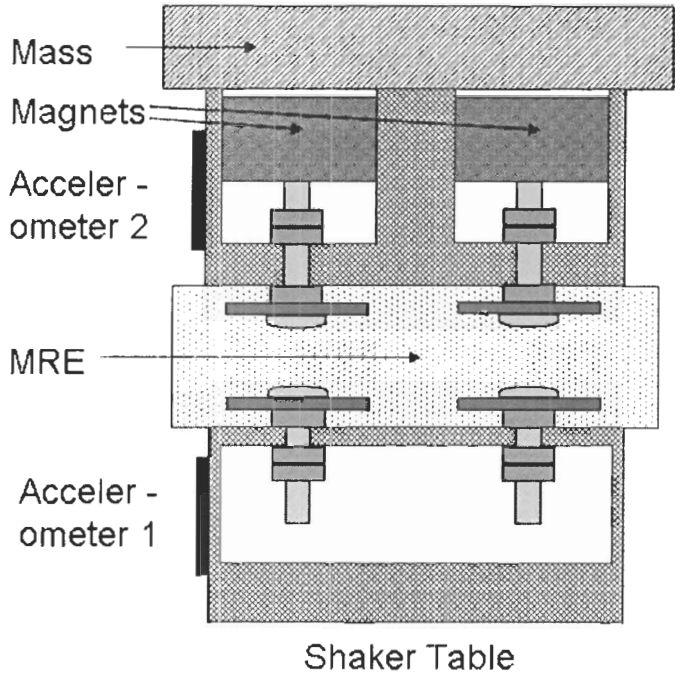

[6] © Michael Sjoerdsma, reproduced with permission

Figure 1.6: MRE Block Experimental Test Jig Cross Section

The test procedure involved exciting both the nMRE and the mMRE blocks with a 140 mVpp sinusoidal vibration input varying in frequency from 15Hz to 215Hz. This frequency sweep was repeated for both blocks with proof masses of 0.375kg, 0.575kkg, and 0.675kg, respectively. Also, each sweep with a given proof mass was repeated twice, once with magnets and once without.

1.4.3 MRE Vibration Experimental Results

The acceleration data taken at the mass on top of the bushing was divided by the acceleration data from the shaker table to calculate transmissibility for each frequency sweep. For a given proof mass, the resonant frequency changed with the presence of

magnets in the test jig. The transmissibility data exhibiting the largest change in resonant frequency for each block are illustrated in Figure 1.7 and Figure 1.8, respectively.

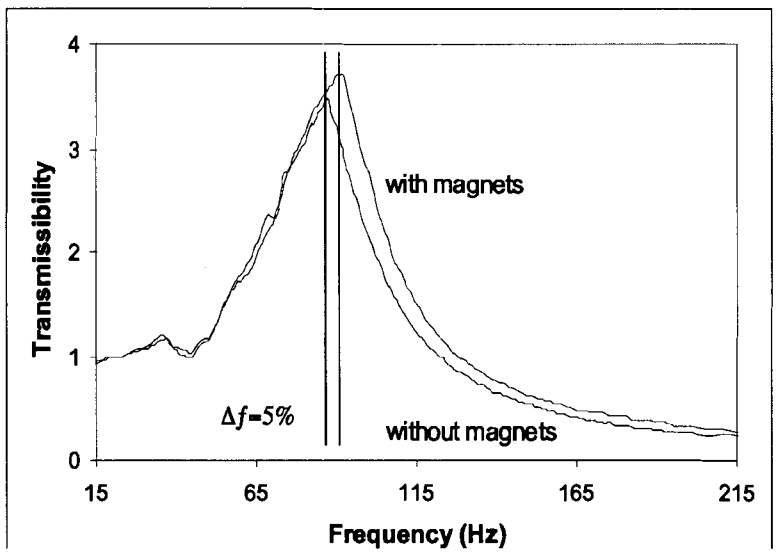

[6] © Michael Sjoerdsma, reproduced with permission

Figure 1.7: nMRE Transmissibility Plot with 0.675kg Proof Mass

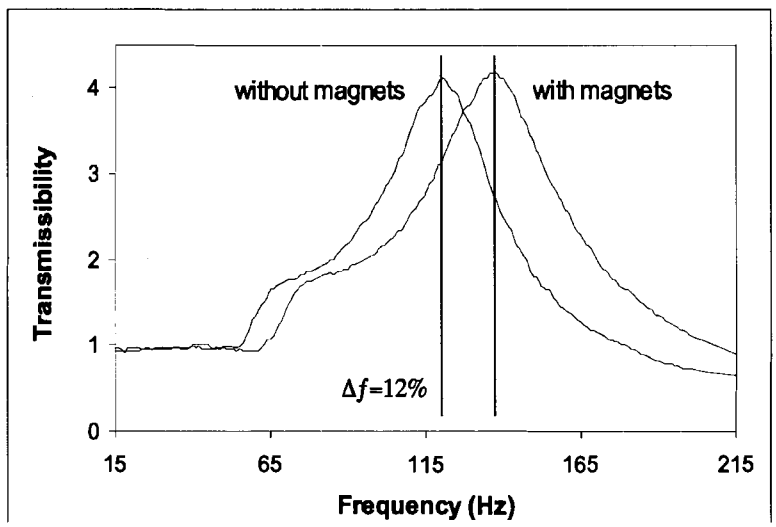

[6] © Michael Sjoerdsma, reproduced with permission

Figure 1.8: mMRE Transmissibility Plot with 0.375kg Proof Mass

Table 1.1: Fractional Change in Resonant Frequency for nMRE and mMRE Blocks

	nMRE			mMRE		
mass (g)	$f0$ (Hz)	$f1$ (Hz)	$\frac{\Delta f}{f_0}$ (%)	$f0$ (Hz)	$f1$ (Hz)	$\frac{\Delta f}{f_0}$ (%)
375	117±1	122±1	4±2	121±1	136±1	12±2
575	95±1	100±1	5±2	108±1	118±1	9±2
675	87±1	91±1	5±2	101±1	111±1	10±2

[6] © Michael Sjoerdsma, reproduced with permission

As shown in Table 1.1 the change in resonant frequency is significantly greater for the mMRE block than the nMRE block.

1.5 Thesis Focus

The focus of my thesis is to address some of the engineering challenges associated with practical implementation of magnetorheological bushings in cars. One of these challenges is to take our investigation of magnetorheological materials towards practical electromagnetic control in automobiles. Past research with magnetorheological devices has depended on extremely large and unwieldy electromagnets [28], whereas, my focus is to use magnetorheological components with smaller commercially available electromagnets. Because of the confined space and finite power source in a vehicle, any magnetorheological bushing in the vehicle suspension must be integrated with electromagnets that are small and energy efficient. Although the research covered in this thesis does not directly solve the structure-borne noise problem, it is nonetheless motivated by the structure borne noise problem. The tools and techniques investigated in

this thesis will be applied in future automobiles for solving the structure borne noise problem.

In keeping with the practical electromagnetic control focus, this thesis covers the fabrication of an EFC damper and experimental test jig in Chapter 2. Chapter 2 also summarizes the vibration experiments conducted with the EFC damper and experimental test jig. Chapter 3 presents three mathematical models that describe the results of the vibration experiments from Chapter 2. Chapter 4 covers some preliminary modelling on electromagnet power amplifiers. Finally, the concluding chapter, Chapter 5, presents some of the future work related to the experiments covered in this thesis.

2 ELECTROMAGNETIC CONTROL OF AN ELASTOMER FERROMAGNET COMPOSITE VIBRATION DAMPER

2.1 EFC Damper Experiment Design

We are interested in reducing vibration transmission through the suspension of a vehicle via electromagnetically controlled magnetorheological (MR) devices. Our first step in electromagnetically controlling magnetorheological materials was to design a suitable experimental apparatus where vibration was directly coupled through a magnetorheological material damper. This apparatus also had to incorporate a pair of electromagnets that were not only in direct physical contact with an elastomer ferromagnet composite (EFC) damper, but also provided a relatively uniform magnetic field through the EFC damper. In order to achieve these apparatus design constraints we designed the experimental apparatus illustrated in Figure 2.1.

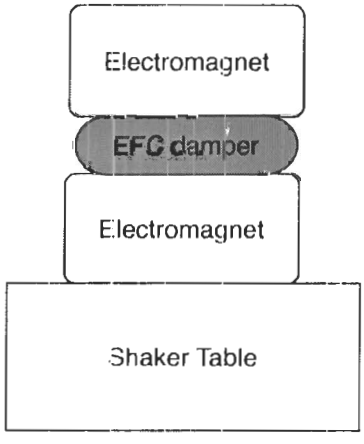

Figure 2.1: Electromagnetically Controlled EFC Damper Experiment Setup

Our experimental device would comprise an EFC damper sandwiched between a pair of evenly matched but opposingly excited electromagnets. This electromagnet pole arrangement ensures uniform field lines through the EFC damper migrating from the North pole electromagnet to the South pole electromagnet. Additionally, magnetic field fringing is minimized by making the EFC damper thickness significantly less than the electromagnet pole diameter [40]. The electromagnet and EFC damper assembly would then be mounted on a shaker table to run the necessary vibration experiments on the EFC damper.

2.1.1 EFC Damper Experimental Apparatus

The assembly process of the test jig shown in Figure 2.1 is explained in this section. The jig consists of a pair of EM-R2 12V DC electromagnets manufactured by Eriez of Canada Ltd. The EM-R2 is an industrial electromagnet for sorting/picking ferromagnetic parts made from low carbon steel. A picture and a diagram of the EM-R2 is shown in Figure 2.2 and Figure 2.3. Note the 2.68cm diameter inner circular area on the electromagnet top is the electromagnet active pole.

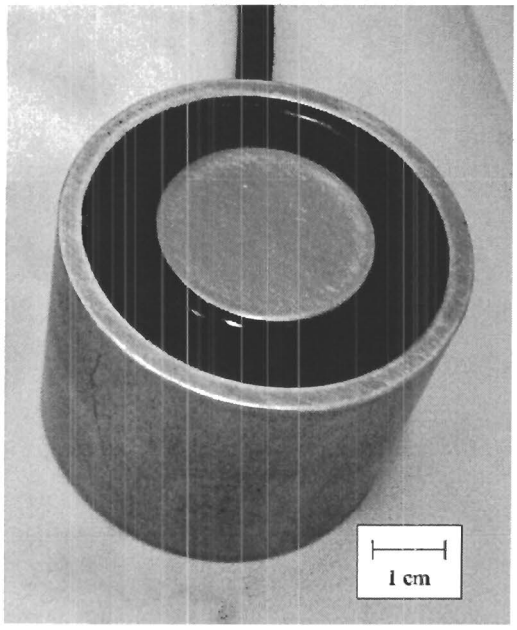

Figure 2.2: EM-R2 Electromagnet

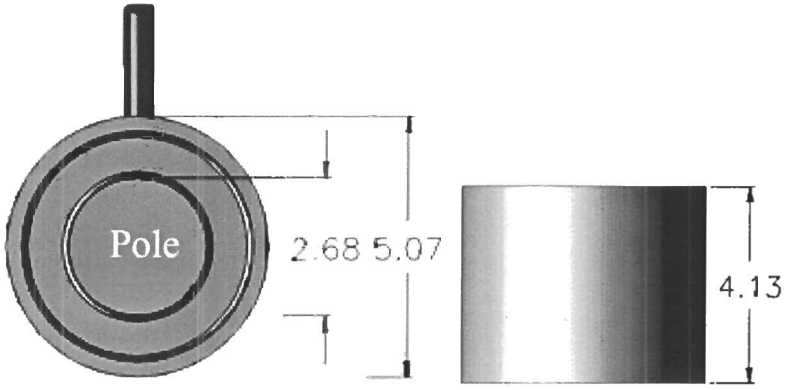

Figure 2.3: EM-R2 Electromagnet Top (L) and Front (R) Views with Dimensions in Centimetres

After selecting the electromagnets, we designed a suitable method to cast the EFC damper. The complete casting process is described in detail in Appendix A. We made our damper with silicone rubber (Sylgard 184) and 10μm spherical iron powder (Alfa Aesar stock # 00170). Because of the low field strength of the EM-R2 electromagnets, we directly glued our EFC damper to both electromagnets to maximize the magnetic field

coupling. To form a strong mechanical bond between the damper and the electromagnets, we glued the damper to both electromagnets with a primer compound (Dow Corning® 92-023) while it was being cured. Also, to maximize electromagnetic field uniformity and minimize electromagnetic field fringing we set the bushing thickness at 0.69cm, significantly less than the 2.68cm diameter EM-R2 active pole. A picture of the cured EFC damper bonded to both electromagnets is shown in Figure 2.4.

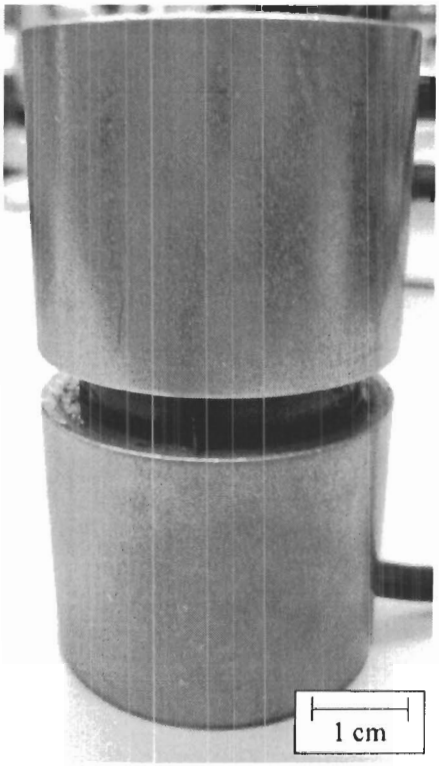

Figure 2.4: Cured EFC Damper Bonded to EM-R2 Electromagnets

The last piece of the test jig consisted of a machined aluminium plate that was used to mount the electromagnet and EFC bushing assembly onto a shaker table. A picture of the aluminium plate is shown in Figure 2.5.

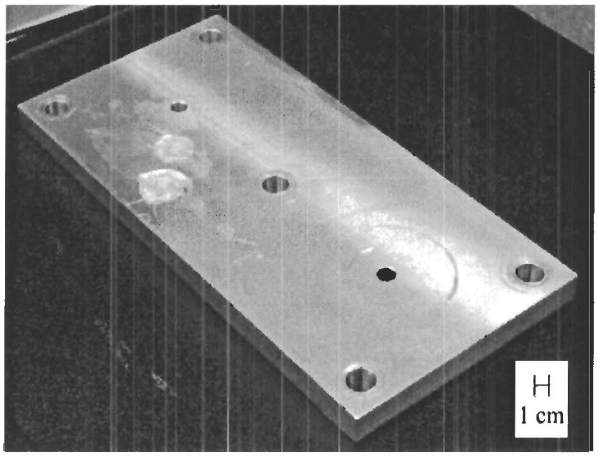

Figure 2.5: EFC Damper Test Jig Mounting Plate

Figure 2.6 shows our EFC damper test jig mounted on the shaker table we used for our experiments.

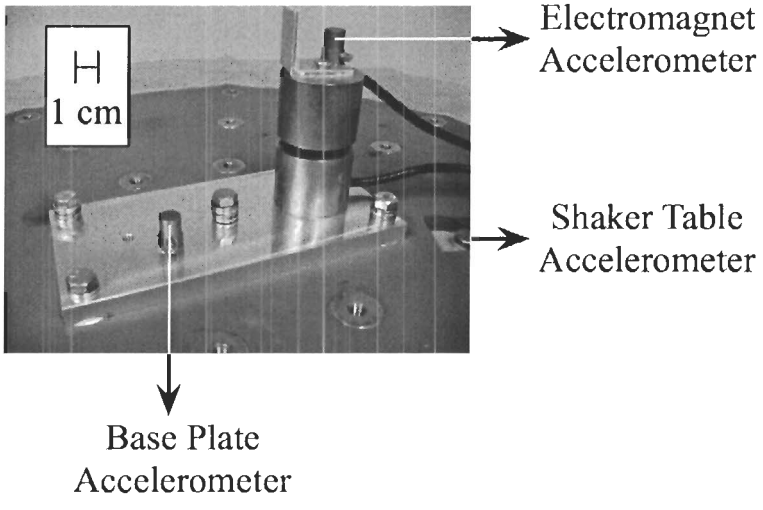

Figure 2.6: EFC Damper Test Jig on Shaker Table

We used a Thermotron DS-640-979 shaker table connected to a Dactron Laser Controller for our vibration experiments. The Dactron Laser Controller, a combination shaker table controller and data acquisition (DAQ) system, was interfaced to a PC running Dactron Shaker Controller software that, not only controlled the shaker table according to user settable test parameters, but also displayed and stored incoming data

from accelerometers connected to the Dactron Laser Controller. For our tests we measured the vibration at three places: the shaker table, the base plate, and the electromagnet mounted on top of the EFC damper. The shaker table vibration data was acquired through an accelerometer embedded in the shaker table surface and the base plate and top electromagnet vibration data were acquired through a pair of PCB Piezotronics 353B03 accelerometers. All the accelerometers are labelled in Figure 2.6. The electromagnets terminals were connected together in a complementary fashion; such that, when powered up, one electromagnet acted as a magnetic North pole and the other as a magnetic South pole. Both electromagnets were powered by a Xantrex XPD33-16 DC power supply. The power supply voltage was measured with a Fluke series 75 DMM. A complete summary of all the equipment used for our experiments is listed in Table 2.1.

Table 2.1: Equipment for EFC Damper Vibration Experiments

Device	Vendor	Version/Model Number
Shaker Table	Thermotron	DS-640-979
Shaker Table Controller and DAQ Hardware	Dactron	Laser Controller ver. 3.10
Shaker Table Controller and DAQ Software	Dactron	Shaker Controller ver. 4.7
Accelerometers	PCB Piezotronics	353B03
Electromagnet Power Supply	Xantrex	XPD33-16
DMM	Fluke	Series 75

2.1.2 EFC Damper Experimental Procedure

Initially, we intended to characterize the EFC damper in the context of a mass spring damper system [29]. Therefore, the top electromagnet in our EFC damper test jig acted as the system proof mass, and the bottom electromagnet and mounting plate acted as the input for a vibration disturbance. Our objective was to characterize the EFC damper in terms of spring and damping constants that would change as a function of the magnetic field propagating through the damper. The shaker table was operated in frequency sweep mode to provide the necessary sinusoidal vibration disturbance to the EFC damper test jig. The shaker table was configured to sweep from 10Hz to 800Hz for all out vibration experiments. We conducted our tests in two distinct phases. In phase one the shaker table frequency sweep amplitude was set at 0.5g, where g is a unit of acceleration equivalent to $9.8m/s^2$. We repeated the 0.5g frequency sweep for electromagnet terminal voltages of 0V to 16V in 4V steps. All the phase one results are graphical, but nonetheless useful because they validate the material nature of our EFC damper. In our phase two experiments the shaker table frequency sweep amplitude was set at 1g. We repeated the 1g amplitude frequency sweep for electromagnet terminal voltages of 0V to 16V in 2V steps. The phase two numerical data was analyzed in Mathematica.

As part of our experiments, we also characterized the magnetic field strength of the EM-R2 electromagnets as a function of applied terminal voltage. The complete electromagnet characterization process and results are described in Appendix B. Because the EFC damper thickness is significantly less than the electromagnet pole diameter, we assumed that the magnetic field through the EFC damper is uniform and can be estimated

as the sum of the individual electromagnet field strengths for a given terminal voltage [40]. The estimated magnetic field strength in the EFC damper for the phase two electromagnet voltages are listed in Table 2.2.

Table 2.2: Estimated Magnetic Field Strength in the EFC Damper in Teslas

Voltage (V)	Electromagnet 1 Field Strength (T) (Top of EFC damper test jig)	Electromagnet 2 Field Strength (T) (Bottom of EFC damper test jig)	Estimated EFC Damper Field Strength (T)
0	0.00100	0.00040	0.00140
2	0.00560	0.00520	0.01080
4	0.01055	0.01040	0.02095
6	0.01555	0.01575	0.03130
8	0.02060	0.02095	0.04155
10	0.02555	0.02630	0.05185
12	0.03050	0.03175	0.06225
14	0.03525	0.03660	0.07185
16	0.03980	0.04110	0.08090

2.2 EFC Damper Experimental Results

Data plots from all the phase one experiments, and a subset of the data plots from the phase two experiments are shown in sections 2.2.1 and 2.2.2. Recall, that in both experiment phases the shaker table frequency sweep was repeated multiple times with different electromagnet terminal voltages. Therefore, for the sake of brevity the plot associated with a given frequency sweep is designated by the electromagnet terminal voltage for that particular frequency sweep. For example, any data plot associated with a frequency sweep performed with 0V electromagnet terminal voltage will be designated with a '0V sweep' label.

2.2.1 EFC Damper Phase 1 Experimental Results

From our phase one experiments, we have vibration versus frequency data plots that show the vibration output of the shaker table, the mounting plate, and the top electromagnet. Both vibration and frequency are plotted on a log scale in all the data plots. All the phase one data plots are shown in Figure 2.7 to Figure 2.11.

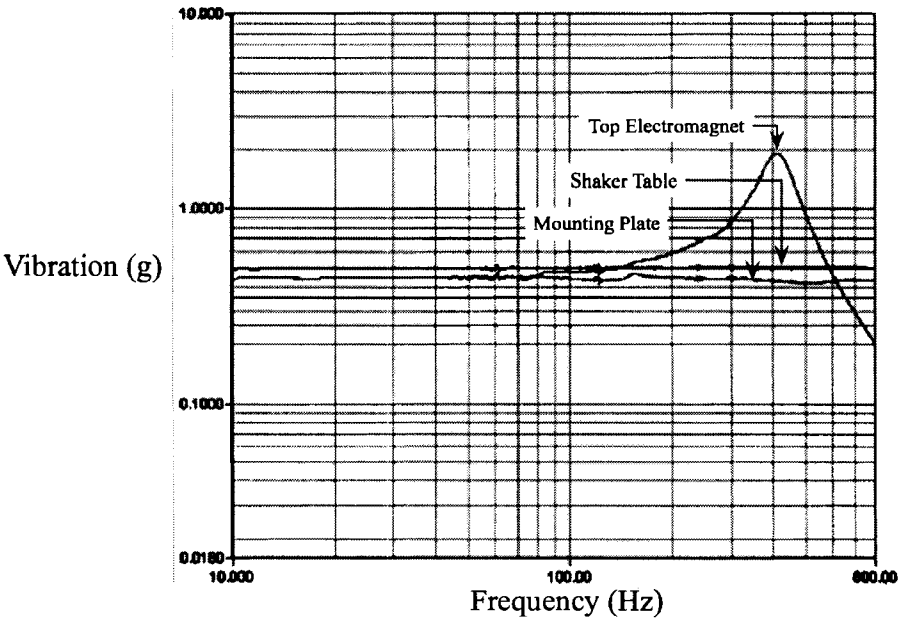

Figure 2.7: EFC Damper Test Jig and Shaker Table Frequency Response; 0V Sweep

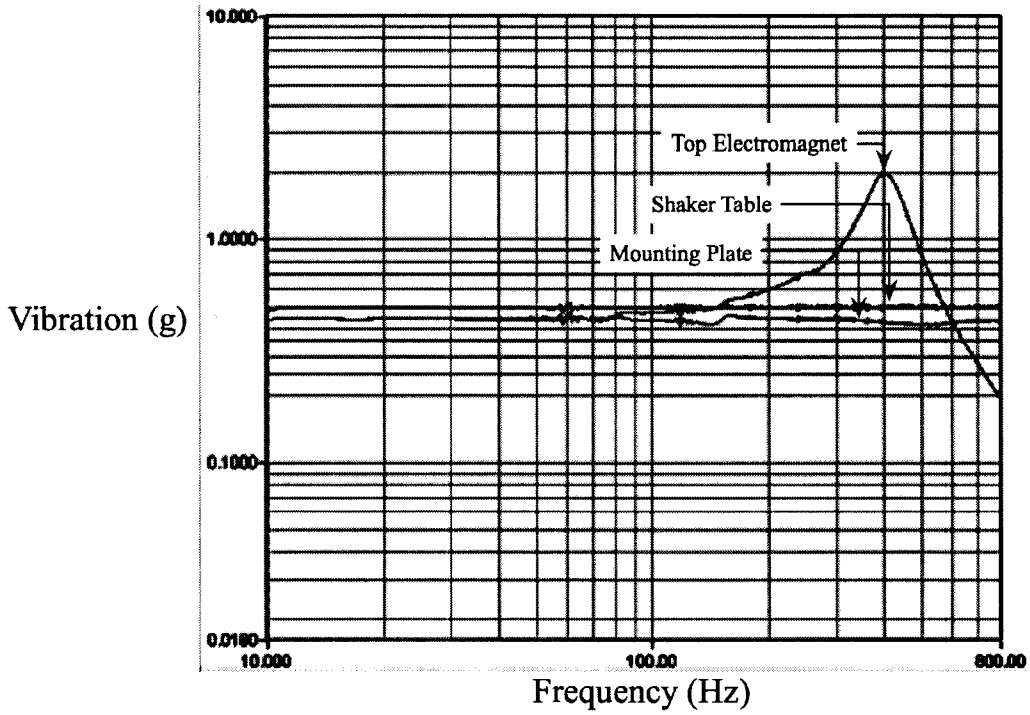

Figure 2.8: EFC Damper Test Jig and Shaker Table Frequency Response; 4V Sweep

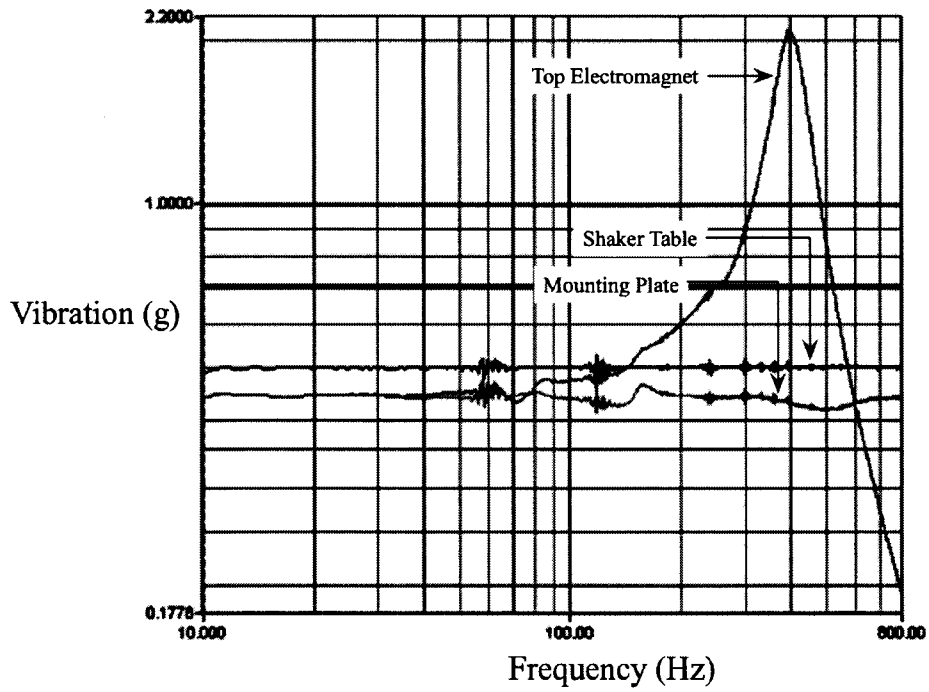

Figure 2.9: EFC Damper Test Jig and Shaker Table Frequency Response; 8V Sweep

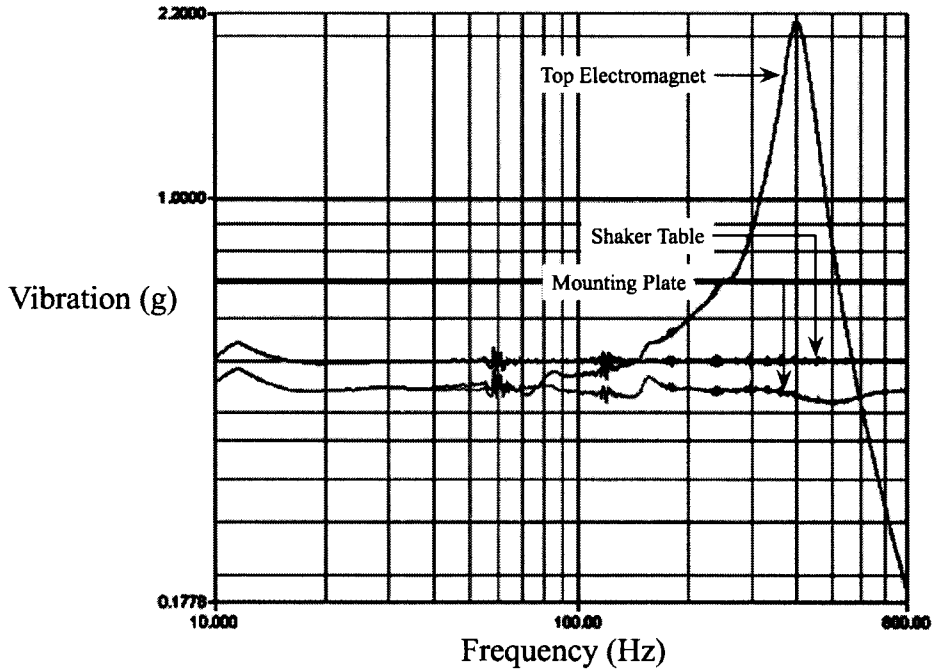

Figure 2.10: EFC Damper Test Jig and Shaker Table Frequency Response; 12V Sweep

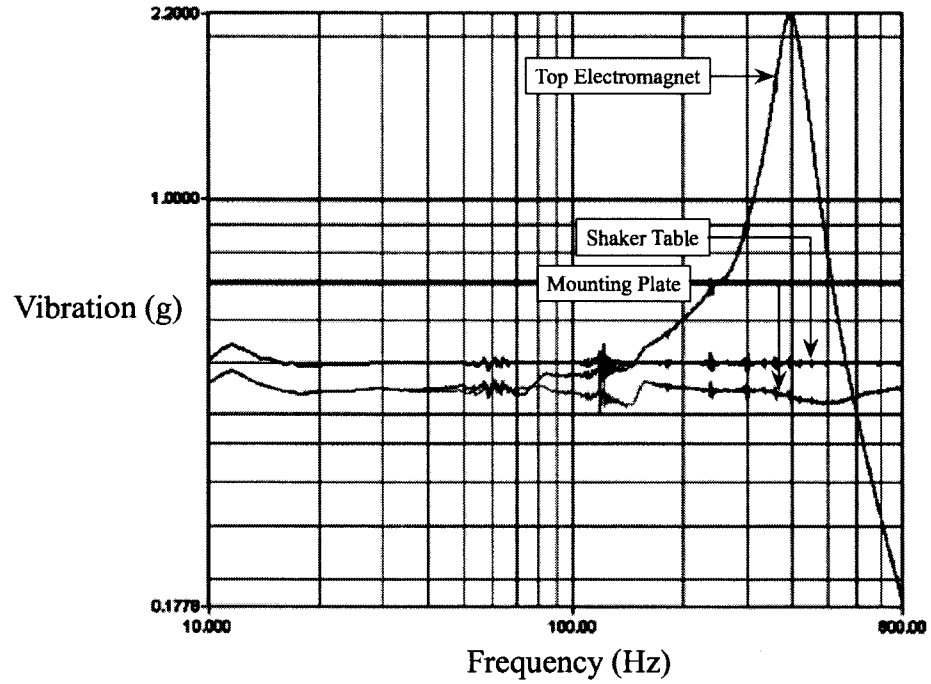

Figure 2.11: EFC Damper Test Jig and Shaker Table Frequency Response; 16V Sweep

In all our frequency sweeps, we noticed that at 60Hz, and subsequent 60Hz frequency harmonics, the shaker table vibration output was extremely noisy because of AC interference in the shaker table power amplifier.

The preliminary results show a noticeable decrease in EFC test jig resonant frequency as a function of magnetic field strength. Even more noticeable is the increased top electromagnet vibration as a function of magnetic field strength. These results, indicate that the EFC damper and stiffness both decrease as a function of increasing magnetic field strength. According to Zhou et al. [30], unlike an MRE damper, an EFC damper actually dilates in the presence of a magnetic field and correspondingly becomes less stiff. Therefore, in the context of our mass spring damper model, the system spring and damping constants both decrease as a function of increasing magnetic field strength through the EFC damper. We verified the EFC damper dilation by attaching a strain gauge to the EFC damper and observing the change in strain when the electromagnets are powered up to 16V. The EFC damper strain measuring process and results are described in Appendix C. In the end, the phase one experimental results were useful for verifying the expected behaviour of our EFC damper as a function of increasing magnetic field strength and provided a framework for the phase two experiments.

2.2.2 EFC Damper Phase 2 Experimental Results

Our phase two experiments were similar to our phase one experiments except that the shaker table frequency sweep amplitude was set at 1g, the frequency sweeps were repeated for electromagnet terminal voltages of 0V to 16V in 2V steps, and we acquired numerical vibration. The numerical vibration data was in the form of frequency in hertz versus acceleration in g, which was downloaded from the PC connected to the shaker

table controller and DAQ system. The shaker table DAQ system acquired 1024 data points for each frequency sweep. Because we conducted nine frequency sweeps, and each frequency sweep yielded three datasets corresponding to the shaker table frequency response, the EFC damper test jig base plate frequency response, and the EFC damper test jig top electromagnet frequency response, we have twenty-seven frequency response datasets. All the datasets are plotted in Appendix D and the 0V sweep dataset plots are shown in Figure 2.12 and Figure 2.13.

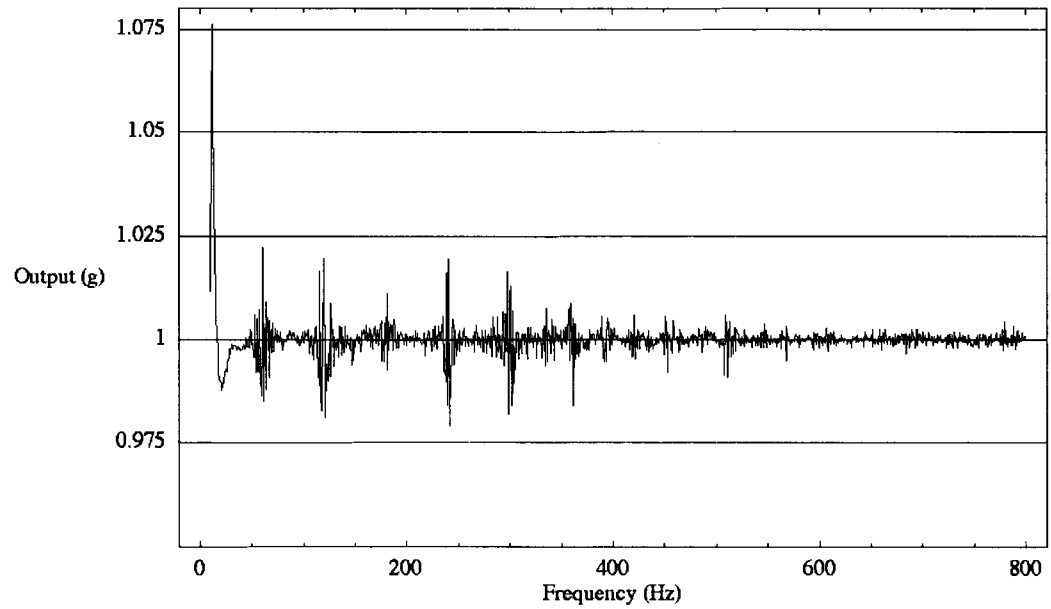

Figure 2.12: Shaker Table Frequency Response, 0V Sweep

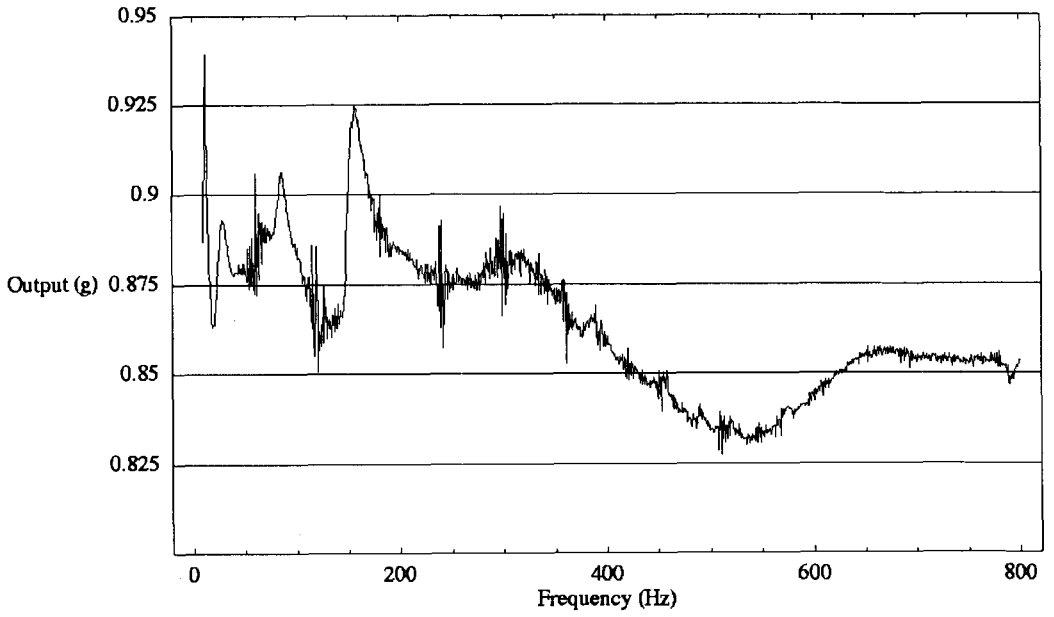

Figure 2.13: EFC Damper Test Jig Base Plate Frequency Response, 0V Sweep

To clearly illustrate the EFC damper test jig frequency response change as a function of magnetic field strength, Figure 2.14 shows a composite data plot of the non-normatilzed top electromagnet frequency response for the 0V, 8V, and 16V sweeps.

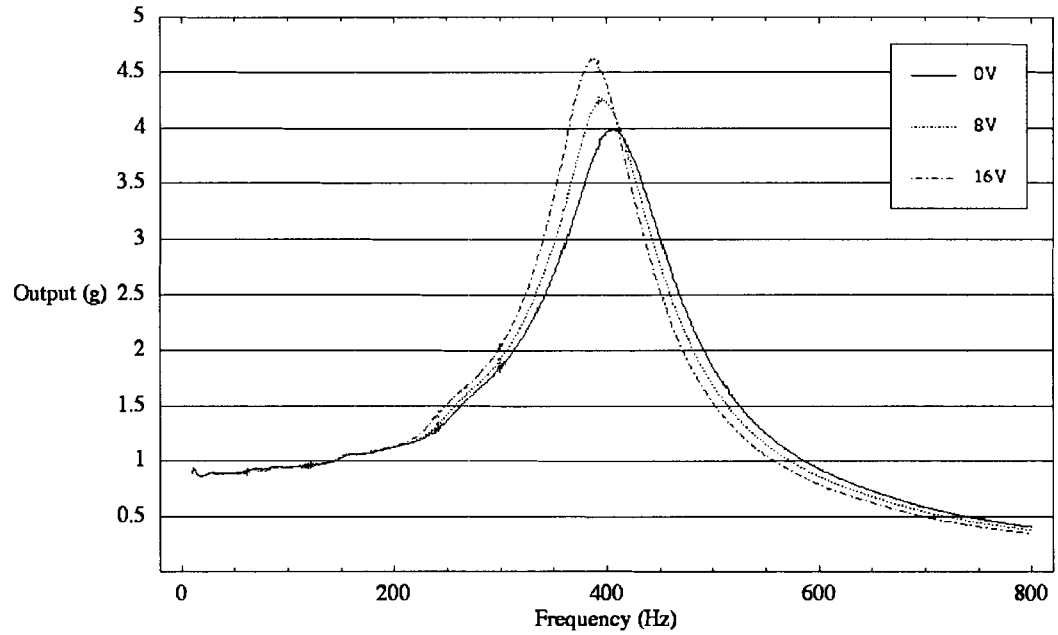

Figure 2.14: Non-normalized Top Electromagnet Frequency Response for 0V, 8V, and 16V Sweeps

The effects of the 60Hz AC noise interference in the shaker table power amplifier manifests itself as 60Hz and subsequent harmonic frequency noise spikes in the shaker table, base plate, and top electromagnet frequency responses. The frequency response of the top electromagnet clearly shows the decreasing resonant frequency of the EFC damper test jig as a function of increasing magnetic field strength through the EFC damper. Additionally, the increasing amplitude of the top electromagnet frequency response curves as a function of increasing magnetic field strength is clearly illustrated. The next chapter discusses the mathematical models that describe the behaviour of the EFC damper test jig, as well as the physical properties of the EFC damper.

3 MATHEMATICAL MODELLING OF THE ELASTOMER FERROMAGNET COMPOSITE DAMPER

The data from the phase two experiments was imported into Mathematica and fit to mathematical models that describe the system level operation of the EFC damper. Because we chose transfer function equations as the mathematical models, we decided to model the EFC damper test jig base plate as the transfer function input and the top electromagnet as the transfer function output. Therefore, the transfer function equations were fit to the normalized transmissibility data between the top electromagnet (transfer function equation output) and the EFC damper test jig base plate (transfer function equation input). The transmissibility data for the 0V, 8V, and 16V frequency sweeps is plotted together in Figure 3.1. Only the transfer function equations and plots relating to the 0V, 8V, and 16V frequency sweeps are derived and shown in this chapter. All the transfer function equations and plots relating to the phase two frequency sweeps are in Appendix D. We applied three different models to the phase two experimental data, which are explained in detail in sections 3.1 and 3.2.

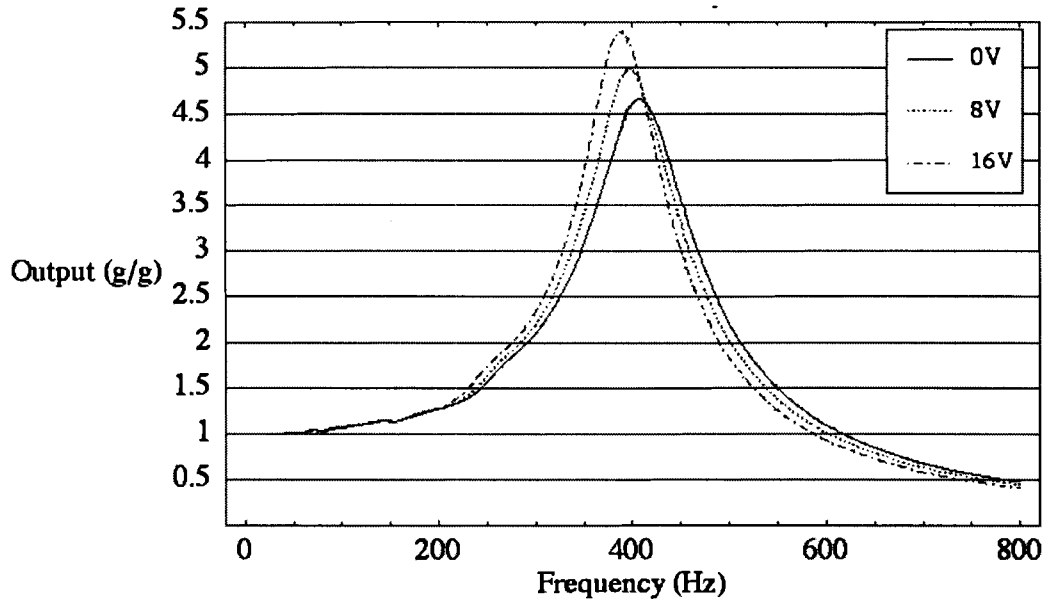

Figure 3.1: Normalized Transmissibility Data Plots for the 0V, 8V, and 16V Frequency Sweeps

3.1 Classical Second Order Linear Mass Spring Damper Model

The first model we applied characterized the EFC damper test jig in the context of a mass spring damper system. A diagram of a mass spring damper system is illustrated in Figure 3.2, and the Laplace transfer function equation is

$$\frac{X_1[s]}{X_2[s]} = \frac{Cs + k}{Ms^2 + Cs + k} \qquad \textbf{Equation 3.1}$$

where, k is the stiffness of the system spring in N/m, C is the damping constant of the system damper in N•sec/m, and M is the value of the system proof mass in kg, which would be the top electromagnet and accelerometer in the case of the EFC test jig. Finally, X_1 and X_2 represent the displacement, in metres, of the system proof mass and the system base, respectively.

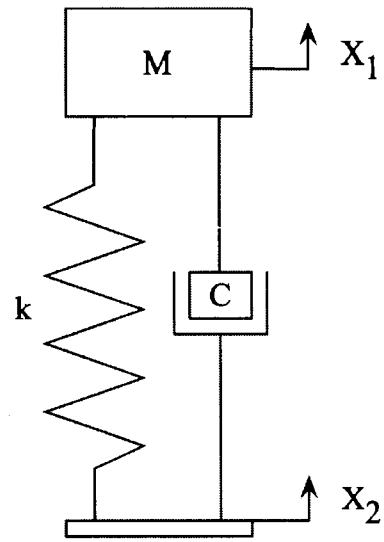

Figure 3.2: Classical Mass Spring Damper System

The derived transmissibility data from our experiments was fit to

$$\left| \frac{C\,j\omega + k}{M\,j\omega^2 + C\,j\omega + k} \right| \qquad \textbf{Equation 3.2}$$

which is the magnitude of Equation 3.1 with $s = j\omega$ where, j is the complex number and ω is angular frequency in radians/second.

For the model fit k, and C were both treated as the unknown parameters, and, M, was set to the combined mass of the top electromagnet, and the accelerometer and miscellaneous hardware mounted on the top electromagnet. The combined mass of the top electromagnet and the hardware mounted on it was measured on an Ohaus Dial-O-Gram balance, with and without the attached electromagnet cable; this yielded two mass figures of 540.9 grams and 529.6 grams, respectively. Because the contribution of the electromagnet cable to the EFC damper test jig proof mass could not be measured, the two measured mass figures were averaged to yield a combined electromagnet and mounted hardware mass of 535.25 grams. The mass of the accelerometer was the

nominal value given in its datasheet [31] of 10.5 grams. Therefore, the total proof mass of the EFC damper test jig, *M*, was 545.7grams.

By default, when fitting data to a model, Mathematica uses the linear least squares fit algorithm for linear model functions, and the Levenberg-Marquardt least squares algorithm for non-linear model functions. For the 0V, 8V, and 16V transmissibility datasets, Mathematica calculated the spring and damping constants using Equation 3.2 for each transmissibility dataset as summarized in Table 3.1.

Table 3.1: Returned Spring and Damper Constants from the Mass Spring Damper Model Fit to the Transmissibility Data

Electromagnet Voltage (V)	k (N/m)	C (N•sec/m)
0	3.754×10^6	311.2
8	3.567×10^6	283.9
16	3.380×10^6	253.9

Recall that in the presence of an increasing magnetic field, an EFC component will dilate and become less stiff. Therefore, the decreasing spring and damping constants of the EFC damper are consistent with the behaviour of an EFC component in a magnetic field. A composite plot of the magnitude function and its matching transmissibility dataset for the 0V sweep is shown in Figure 3.3.

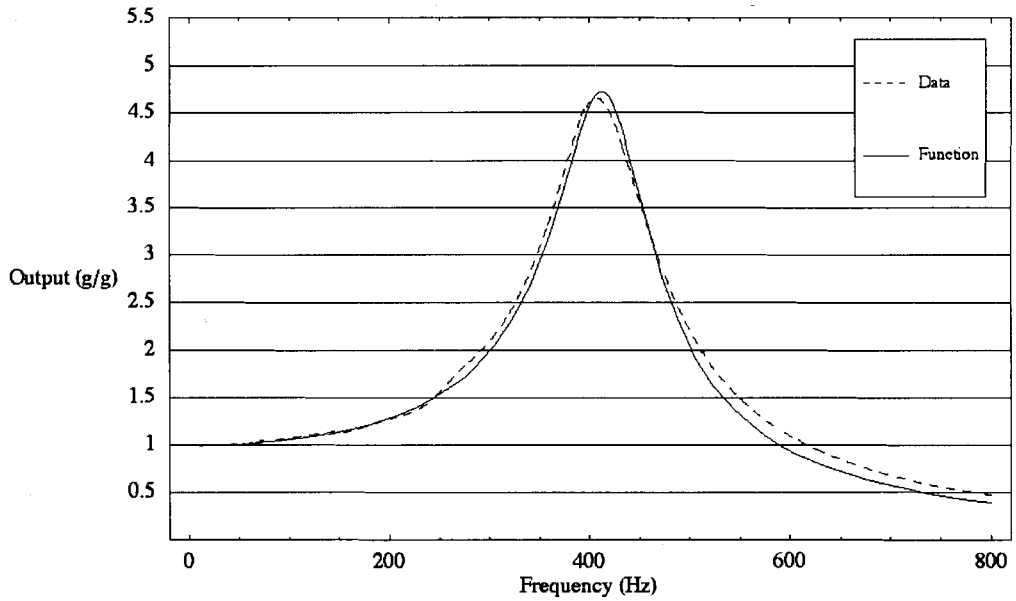

Figure 3.3: 0V Sweep Transmissibility Dataset and Second Order Magnitude Function Plot

The fit between the 0V sweep transmissibility dataset and its corresponding second order magnitude function is coarse at best. From 10Hz until about 450Hz the function leads the dataset and past 450Hz the function progressively lags the dataset. The exact disparity between the 0V sweep dataset and its corresponding function is analyzed by examining the dataset to function error.

3.1.1 Second Order Model Error Analysis

The percentage fit error between the 0V sweep transmissibility dataset and its corresponding second order magnitude function is shown in Figure 3.4. The percentage fit error is calculated by

$$100 * \left| \frac{f - d}{d} \right| \qquad \textbf{Equation 3.3}$$

where, f is the second order magnitude function value, and d is the transmissibility dataset value for a given frequency.

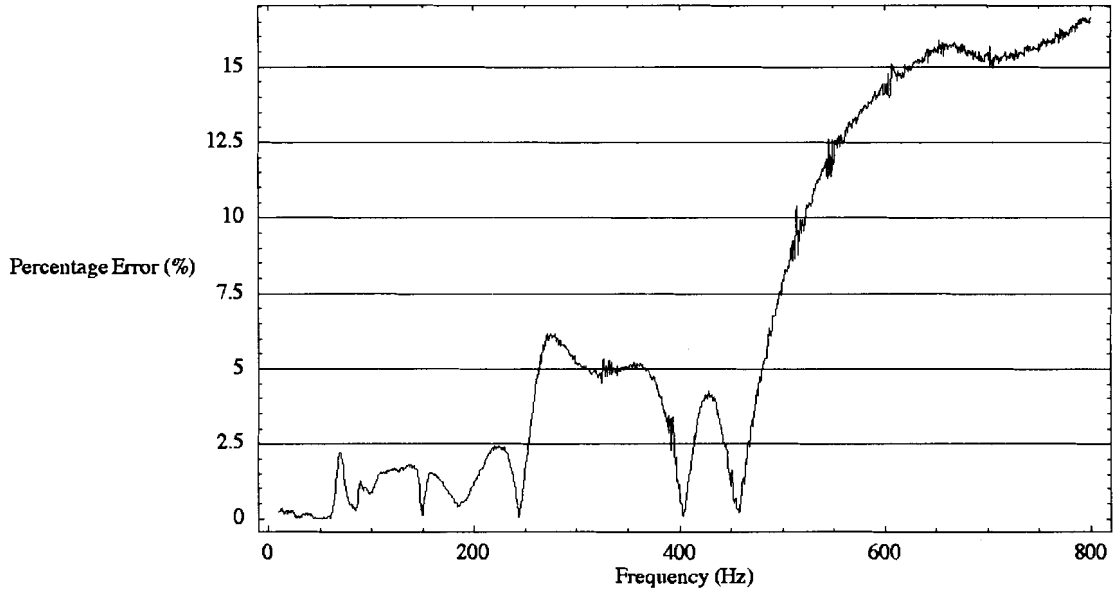

Figure 3.4: Percentage Fit Error of the Mass Spring Damper Model for the 0V Sweep Transmissibility Dataset

In spite of a definite correlation between the 0V sweep transmissibility dataset and its fitted mass spring damper function, overall the mass spring damper model fails to accurately describe the behaviour of the EFC damper test jig. From 450Hz to 800Hz, the sheer scale of the percentage error, reaching a maximum at 16%, clearly indicates that the mass spring damper model cannot accurately model the EFC damper test jig. Because of these modelling inaccuracies, we applied more sophisticated models to the transmissibility datasets.

3.2 Viscoelastic Material Model

A viscoelastic material is defined as a material that dissipates energy during physical deformation; most rubbers and polymers are considered viscoelastic materials. Specifically, internal molecular interactions in the material during deformation lead to stiffness and energy dissipation. Consequently, a viscoelastic material will respond with a phase delayed harmonically varying strain when subjected to a harmonically varying stress. Additionally, when subjected to vibration, the stiffness and energy dissipation in a viscoelastic material will manifest itself as damping [29]. Zhou [22] and Jolly et al. [32] allude to the viscoelastic nature of MR materials. Because the EFC damper is made of a viscoelastic material, we decided to use a viscoelastic material model to characterize it. Jones [29] covers the complex modulus and fractional derivative models. The complex modulus model is a frequency domain model that describes the stress and strain behaviour of a harmonically excited viscoelastic material. The fractional derivative model is a time domain model that describes the stress and strain behaviour of a viscoelastic material. Jones also covers classical viscoelastic models, such as the Maxwell and Voigt models, that describe the behaviour of a viscoelastic material in terms of series and/or parallel spring and damper elements. Jones also proposes an ideal single degree of freedom system similar to a second order mass spring damper system except that the spring and damping constants are replaced by a function k^*, which is the complex stiffness of a viscoelastic material in N/m. A diagram of the ideal single degree of freedom system is illustrated in Figure 3.5 where, M is the system proof mass in kg, and X_1 and X_2 represent the displacement, in metres, of the system proof mass and the system base, respectively.

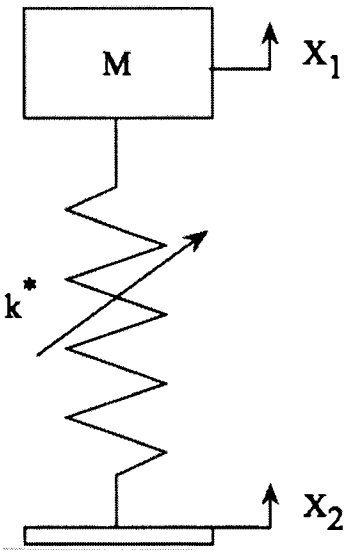

Figure 3.5: Viscoelastic Material Model

The complex stiffness, k^*, is further broken into two terms

$$k^* = k[\omega](1 + j\eta[\omega]) \qquad \textbf{Equation 3.4}$$

where, $k[\omega]$ is the real stiffness component function in N/m, and $\eta[\omega]$ is the dimensionless energy loss component function. Both the real and complex components may be functions of frequency, which means that the viscoelastic material is time variant, and consequently nonlinear. We decided to fit our data to a model based on the Figure 3.5 single degree of freedom system. The viscoelastic model we applied to the transmissibility datasets is given by

$$\left| \frac{k[\omega](j\eta[\omega] + 1)}{M(j\omega)^2 + k[\omega](j\eta[\omega] + 1)} \right| \qquad \textbf{Equation 3.5}$$

The transmissibility datasets were fit to two separate viscoelastic models. However, in the first viscoelastic model, the complex stiffness was a linear function of frequency, and in the second viscoelastic model, the complex stiffness was a quadratic

function of frequency. The results from fitting the transmissibility datasets to the two viscoelastic models are illustrated and analyzed sections 3.2.1 and 3.2.2.

3.2.1 Linear Viscoelastic Material Model

In the linear viscoelastic model the EFC damper stiffness and damping change linearly with frequency. For the linear viscoelastic model, the viscoelastic material complex stiffness, k^*,

$$k^* = k_1 \omega + k_0 + j(C_1 \omega + C_0) \qquad \textbf{Equation 3.6}$$

as well as the components of k^*,

$$k[\omega] = k_1 \omega + k_0 \qquad \textbf{Equation 3.7}$$

and

$$\eta[\omega] = \frac{C_1 \omega + C_0}{k_1 \omega + k_0} \qquad \textbf{Equation 3.8}$$

are assumed to be linear functions of frequency.

The linear viscoelastic model was fit to all the transmissibility datasets, but only the 0V, 8V, and 16V datasets are analyzed here. The stiffness function equations, generated from the model fit, are given by

$$2.098\times10^{6}+(5.171\times10^{2})\,\omega, \qquad \textbf{Equation 3.9}$$

$$1.985\times10^{6}+(5.095\times10^{2})\,\omega, \text{ and} \qquad \textbf{Equation 3.10}$$

$$1.985\times10^{6}+(5.095\times10^{2})\,\omega. \qquad \textbf{Equation 3.11}$$

for the 0V, 8V, and 16V datasets, respectively. And, the loss function equations, generated from the model fit, are given by

$$\frac{1.956\times10^{6}-(4.758\times10^{2})\,\omega}{2.098\times10^{6}+(5.171\times10^{2})\,\omega}, \qquad \textbf{Equation 3.12}$$

$$\frac{1.978\times10^{6}-(5.292\times10^{2})\,\omega}{1.985\times10^{6}+(5.095\times10^{2})\,\omega}, \text{ and} \qquad \textbf{Equation 3.13}$$

$$\frac{1.835\times10^{6}-(5.147\times10^{2})\,\omega}{1.982\times10^{6}+(4.678\times10^{2})\,\omega}. \qquad \textbf{Equation 3.14}$$

for the 0V, 8V, and 16V datasets, respectively.

A composite plot of each dataset and its matching linear viscoelastic model function, as well as composite plots of the real stiffness and complex loss functions are shown in Figure 3.6 to Figure 3.10.

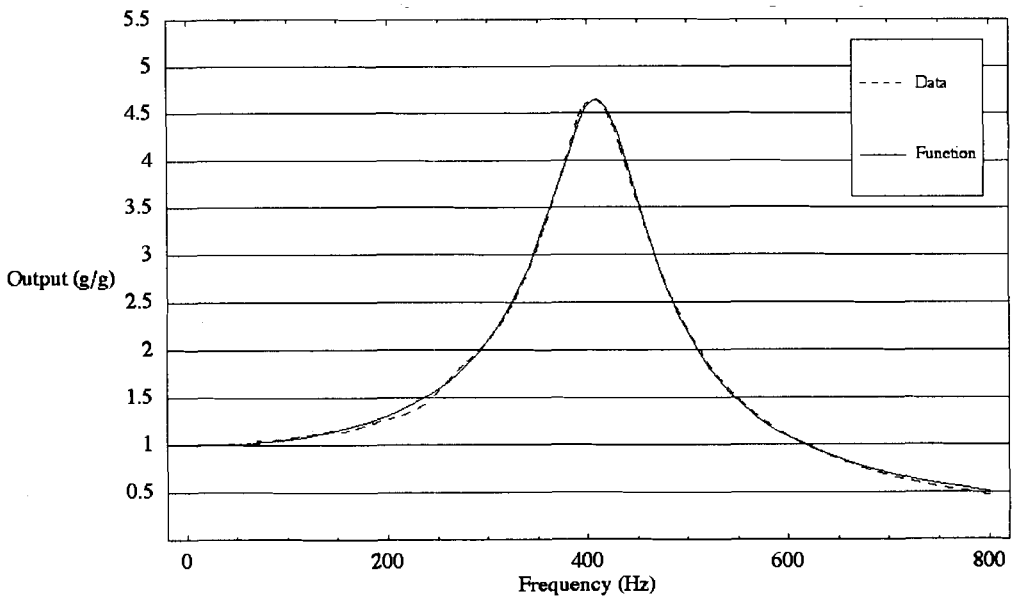

Figure 3.6: 0V Sweep Transmissibility Dataset and Linear Viscoelastic Magnitude Function Plot

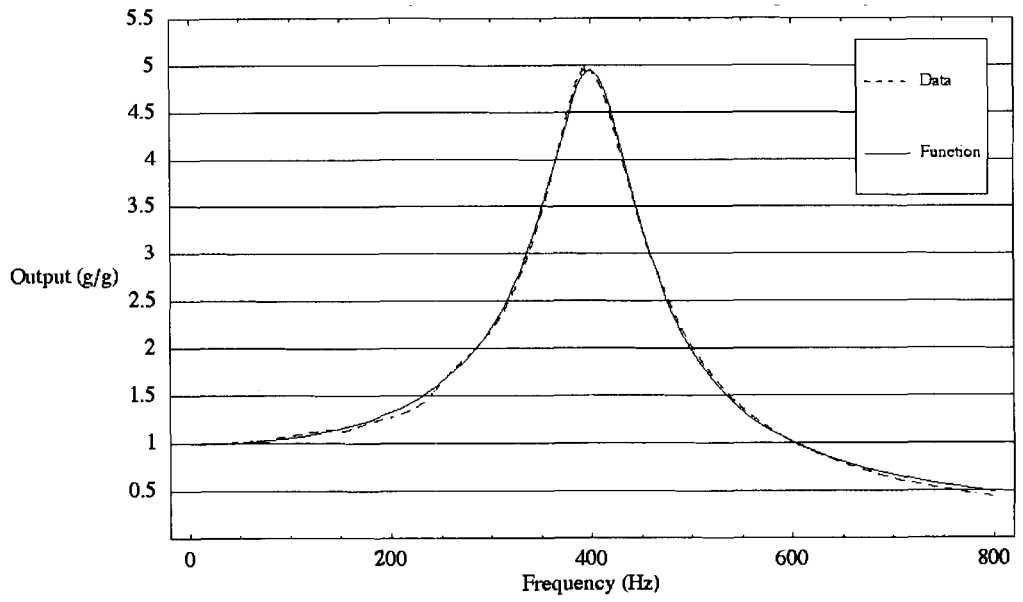

Figure 3.7: 8V Sweep Transmissibility Dataset and Linear Viscoelastic Magnitude Function Plot

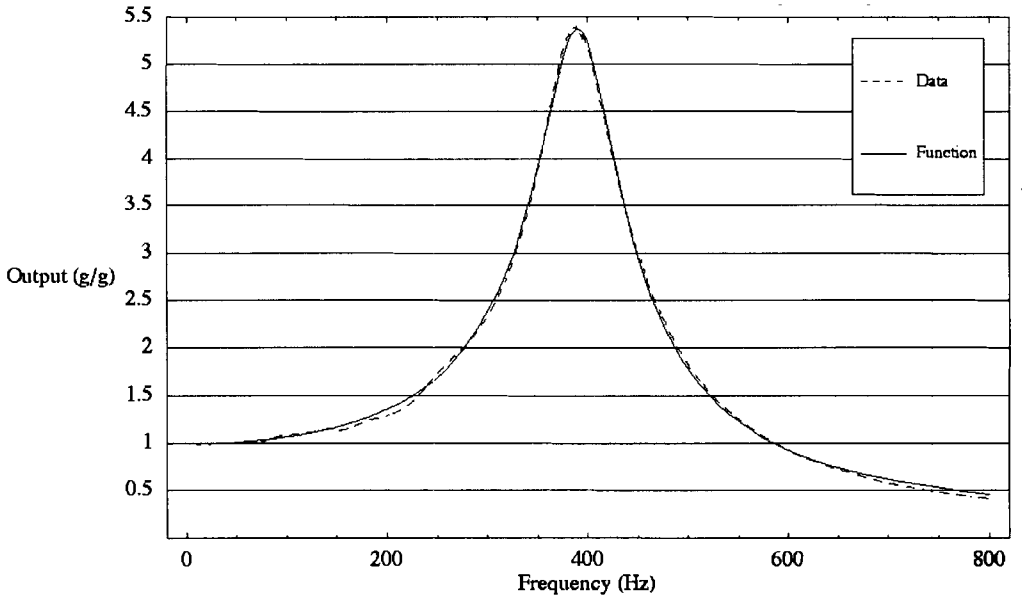

Figure 3.8: 16V Sweep Transmissibility Dataset and Linear Viscoelastic Magnitude Function Plot

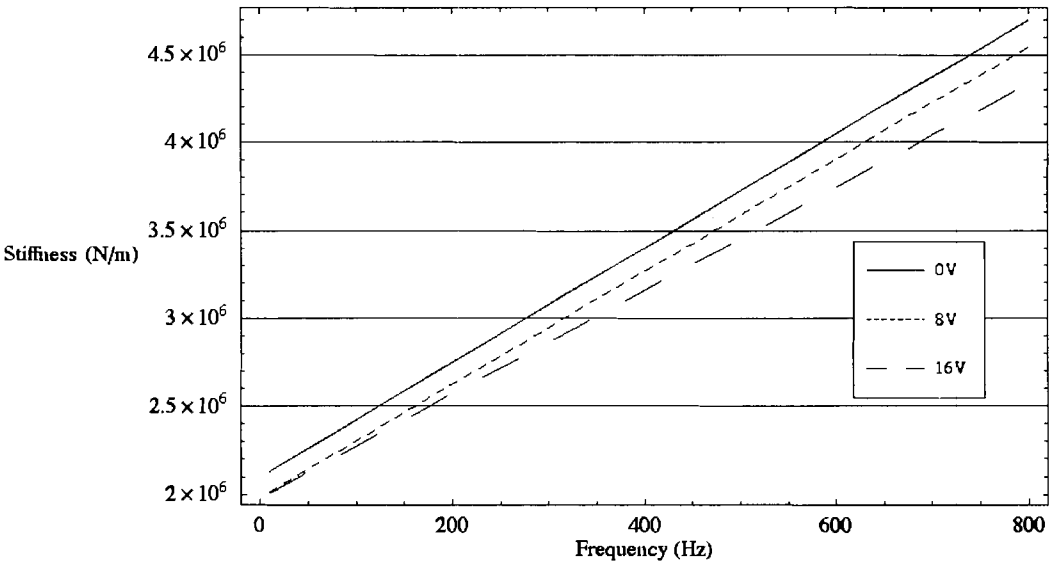

Figure 3.9: Real Stiffness Functions of the EFC Damper Linear Viscoelastic Model for the 0V, 8V, and 16V Sweep Transmissibility Datasets

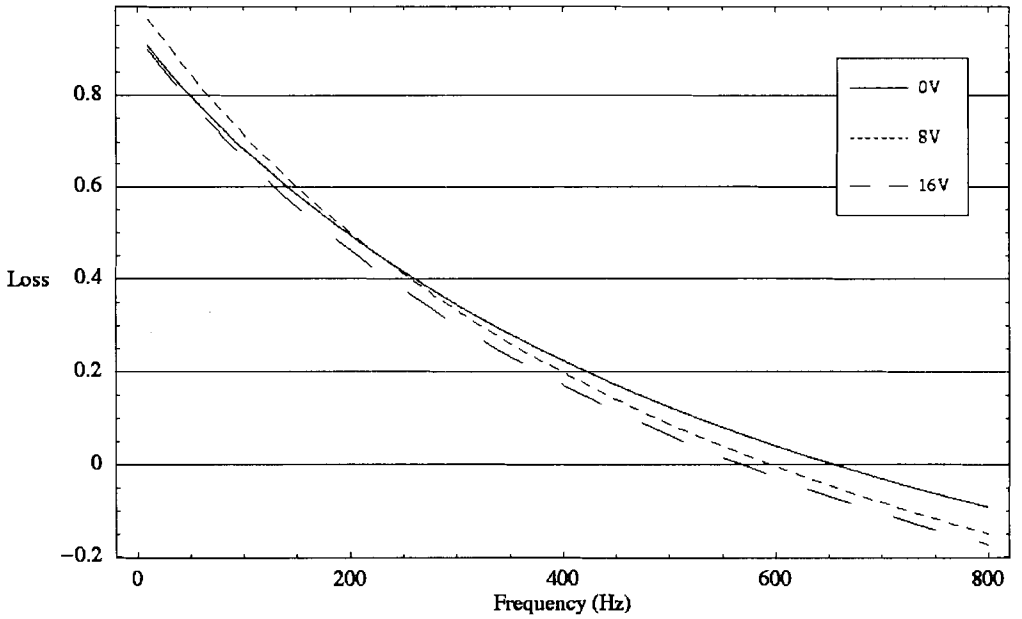

Figure 3.10: Complex Loss Functions of the EFC Damper Linear Viscoelastic Model for the 0V, 8V, and 16V Sweep Transmissibility Datasets

By inspection alone, the linear viscoelastic model fits the transmissibility datasets significantly better than the mass spring damper model. Although, the linear viscoelastic magnitude function values are greater than the transmissibility dataset values from 700Hz to 800Hz, overall, the linear viscoelastic magnitude function values track the transmissibility dataset values. The dramatically large changes in both the stiffness and loss parameter functions explains the large inaccuracies in trying to model the EFC damper test jig in the context of a time invariant mass spring damper system. Whereas, the loss parameter function decreases as a function of frequency, and decreases overall as a function of magnetic field strength. The acquired resonant frequencies and transmissibility magnitudes from the linear viscoelastic magnitude functions are shown in Table 3.2.

Table 3.2: **Acquired Resonant Frequencies from the Linear Viscoelastic Transmissibility Model**

Electromagnet Voltage (V)	Resonant Frequency (Hz)	Transmissibility Magnitude	Resonant Frequency Percentage Change (%)
0	409.3	4.647	N/A
8	399.8	4.950	-2.324
16	390.2	5.364	-4.649

The final column in Table 3.2 illustrates the percentage change in resonant frequency between the 0V sweep and each subsequent sweep. Because of the low field strength of the electromagnets, the change in resonant frequency between the 0V and 16V transmissibility datasets is 4.7%. However, this change is significant, nonetheless because it proves that off-the-shelf electromagnets can change the stiffness of an EFC damper.

3.2.1.1 Linear Viscoelastic Model Error Analysis

The percentage fit error plots for the linear viscoelastic model are shown in Figure 3.11 to Figure 3.13. The percentage fit error is calculated in the same manner as for the mass spring damper model.

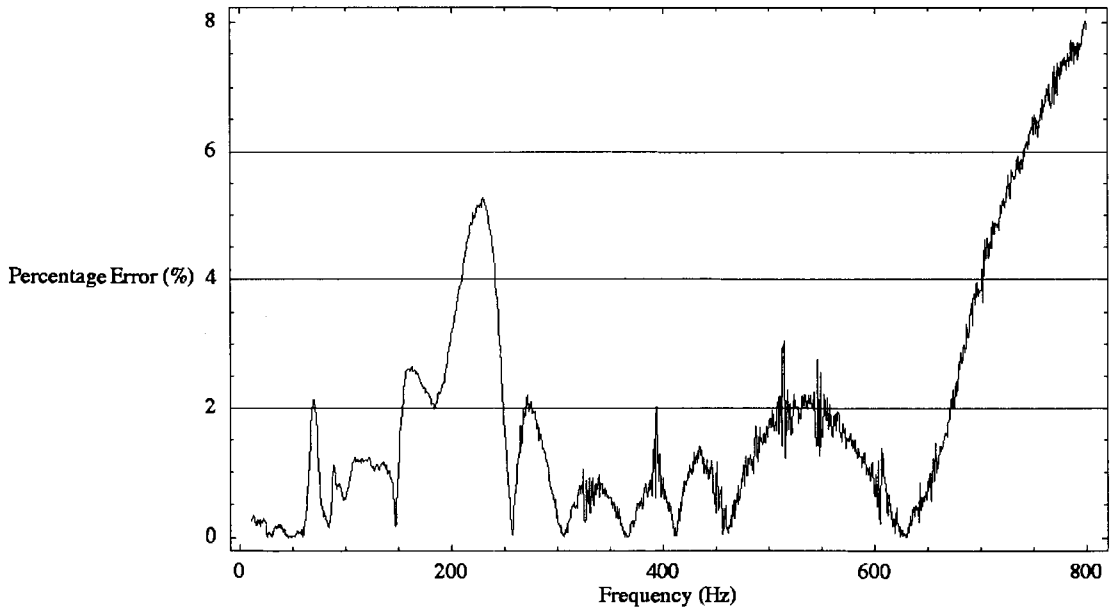

Figure 3.11: Percentage Fit Error of the Linear Viscoelastic Model for the 0V Sweep Transmissibility Dataset

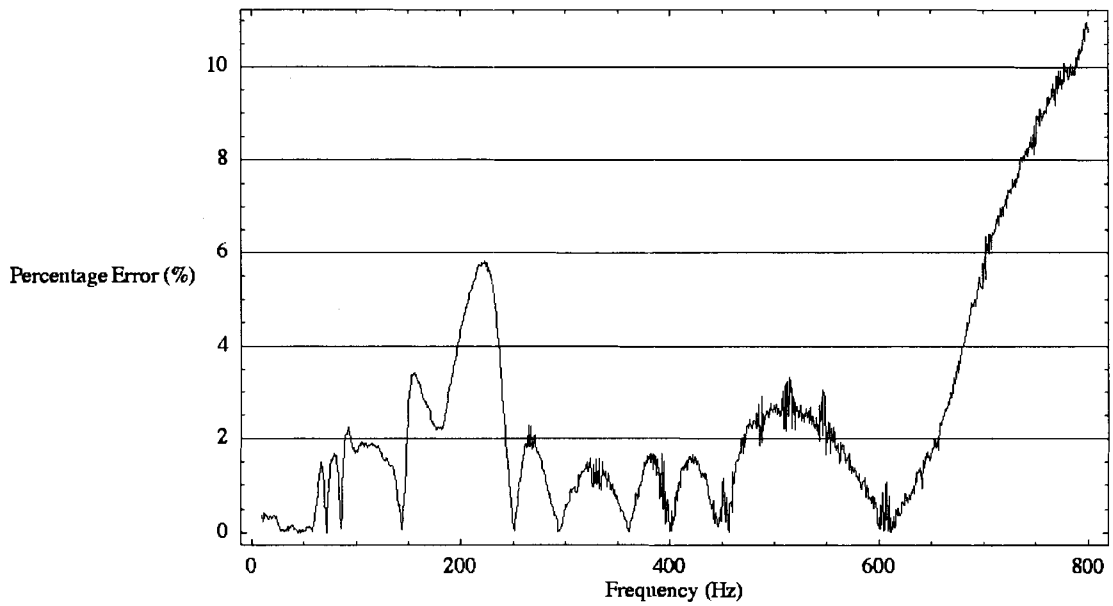

Figure 3.12: Percentage Fit Error of the Linear Viscoelastic Model for the 8V Sweep Transmissibility Dataset

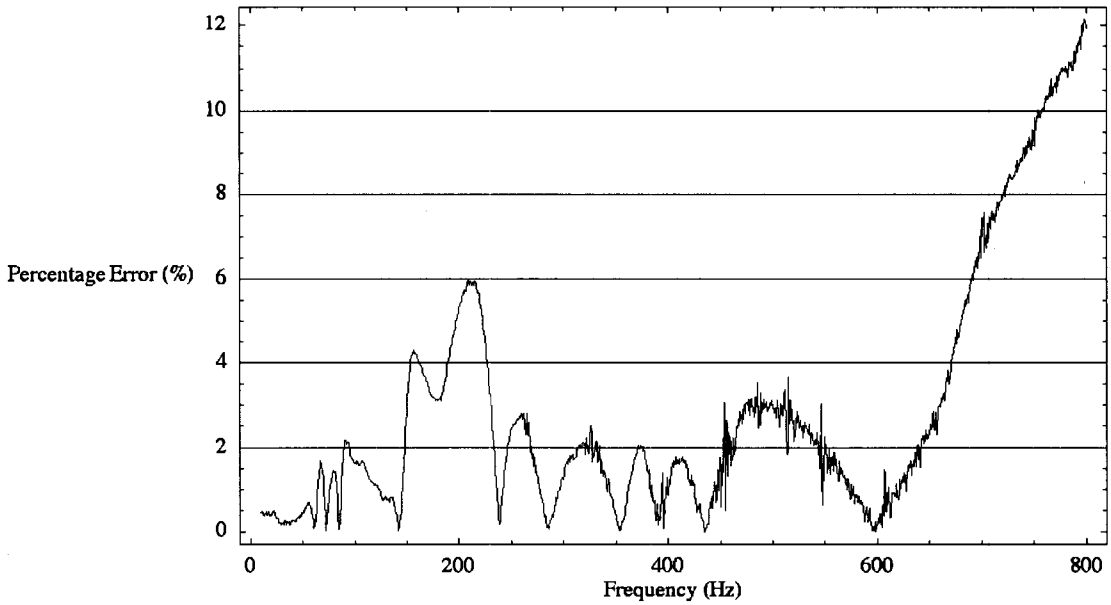

Figure 3.13: Percentage Fit Error of the Linear Viscoelastic Model for the 16V Sweep Transmissibility Dataset

The percentage fit error of the linear viscoelastic model also shows an improvement over the percentage fit error of the mass spring damper model; again, in the 0V sweep case where the error at 800Hz changes from 15%, for the mass spring damper model, to 7.8% for the linear viscoelastic model. However, the percentage fit error of the linear viscoelastic model is 10.7% at 800Hz for the 8V sweep, and 12.4% at 800 Hz for the 16V sweep. Because our desired percentage fit error was 5%, we applied the quadratic viscoelastic model to our transmissibility datasets.

3.2.2 Quadratic Viscoelastic Material Model

In the quadratic viscoelastic model the EFC damper stiffness and damping change quadratically with frequency. For the quadratic viscoelastic model, the complex stiffness, k^*,

$$k^* = k_2 \omega^2 + k_1 \omega + k_0 + j(C_2 \omega^2 + C_1 \omega + C_0) \qquad \textbf{Equation 3.15}$$

as well as the components of k^*,

$$k[\omega] = k_2 \omega^2 + k_1 \omega + k_0 \qquad \textbf{Equation 3.16}$$

and

$$\eta[\omega] = \frac{C_2 \omega^2 + C_1 \omega + C_0}{k_2 \omega^2 + k_1 \omega + k_0} \qquad \textbf{Equation 3.17}$$

are assumed to be quadratic functions of frequency.

As with the linear viscoelastic model, the quadratic viscoelastic model was fit to all the transmissibility datasets, but only the 0V, 8V, and 16V datasets are analyzed here.

The stiffness function equations, generated from the model fit, are given by

$$3.121 \times 10^6 + (3.835 \times 10^2)\omega - (3.308 \times 10^{-2})\omega^2, \qquad \textbf{Equation 3.18}$$

$$2.934 \times 10^6 + (4.011 \times 10^2)\omega - (3.655 \times 10^{-2})\omega^2, \text{ and} \qquad \textbf{Equation 3.19}$$

$$2.716 \times 10^6 + (4.308 \times 10^2)\omega - (4.276 \times 10^{-2})\omega^2. \qquad \textbf{Equation 3.20}$$

for the 0V, 8V, and 16V datasets, respectively. And, the loss function equations, generated from the model fit, are given by

$$\frac{3.327\times10^{6}-(2.185\times10^{3})\omega+(2.242\times10^{-1})\omega^{2}}{3.121\times10^{6}+(3.835\times10^{2})\omega-(3.308\times10^{-2})\omega^{2}}, \qquad \textbf{Equation 3.21}$$

$$\frac{3.652\times10^{6}-(2.399\times10^{3})\omega+(2.622\times10^{-1})\omega^{2}}{2.934\times10^{6}+(4.011\times10^{2})\omega-(3.655\times10^{-2})\omega^{2}}, \text{ and} \qquad \textbf{Equation 3.22}$$

$$\frac{3.453\times10^{6}-(2.277\times10^{3})\omega+(2.504\times10^{-1})\omega^{2}}{2.716\times10^{6}+(4.308\times10^{2})\omega-(4.276\times10^{-2})\omega^{2}}. \qquad \textbf{Equation 3.23}$$

for the 0V, 8V, and 16V datasets, respectively.

A composite plot of each transmissibility dataset and its matching quadratic viscoelastic model function, as well as composite plots of the real stiffness and complex loss functions, are shown in Figure 3.14 to Figure 3.17.

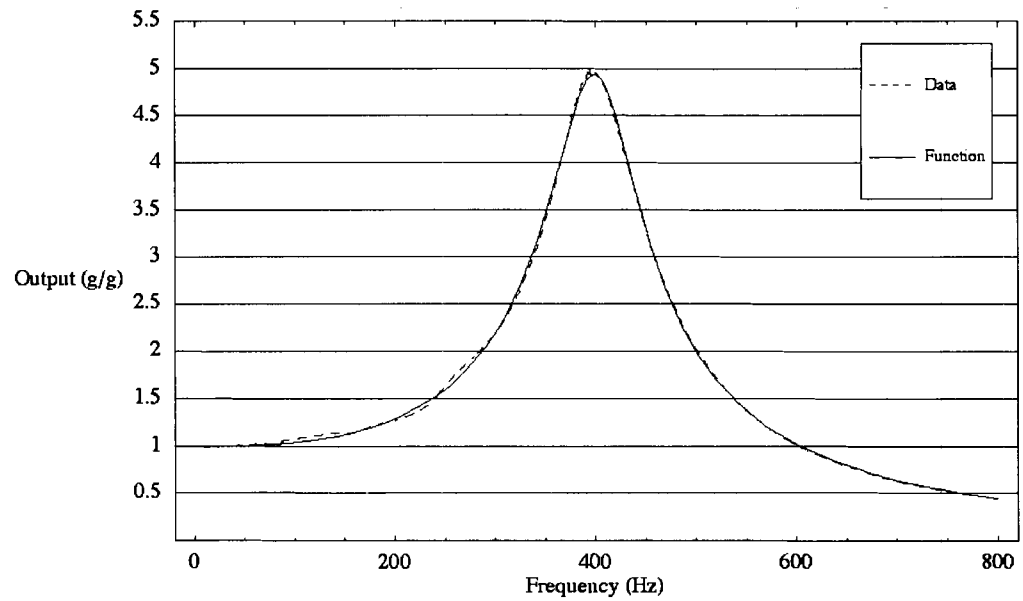

Figure 3.14: 0V Sweep Transmissibility Dataset and Quadratic Viscoelastic Magnitude Function Plot

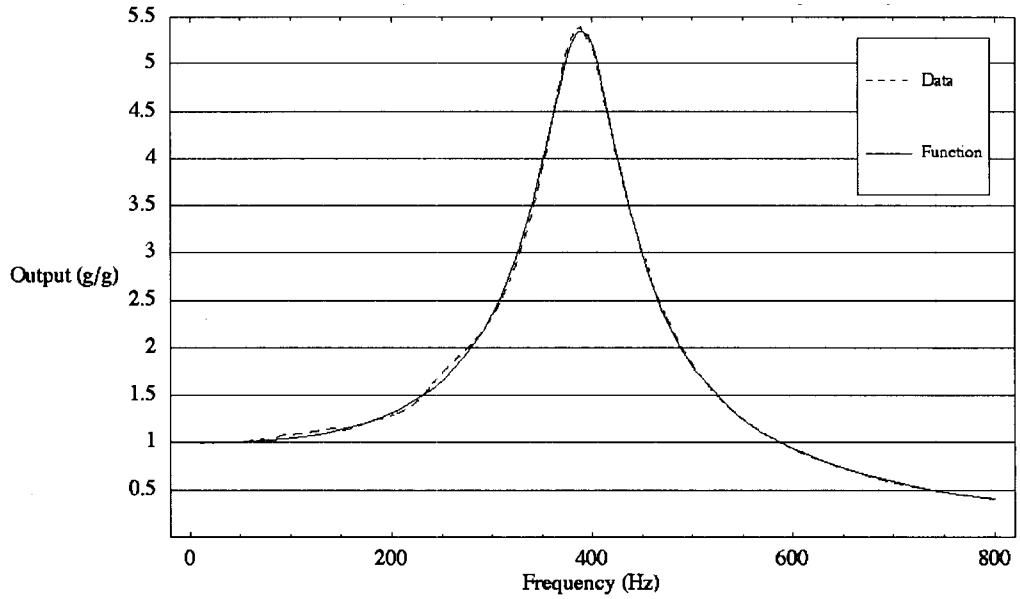

Figure 3.15: 16V Sweep Transmissibility Dataset and Quadratic Viscoelastic Magnitude Function Plot

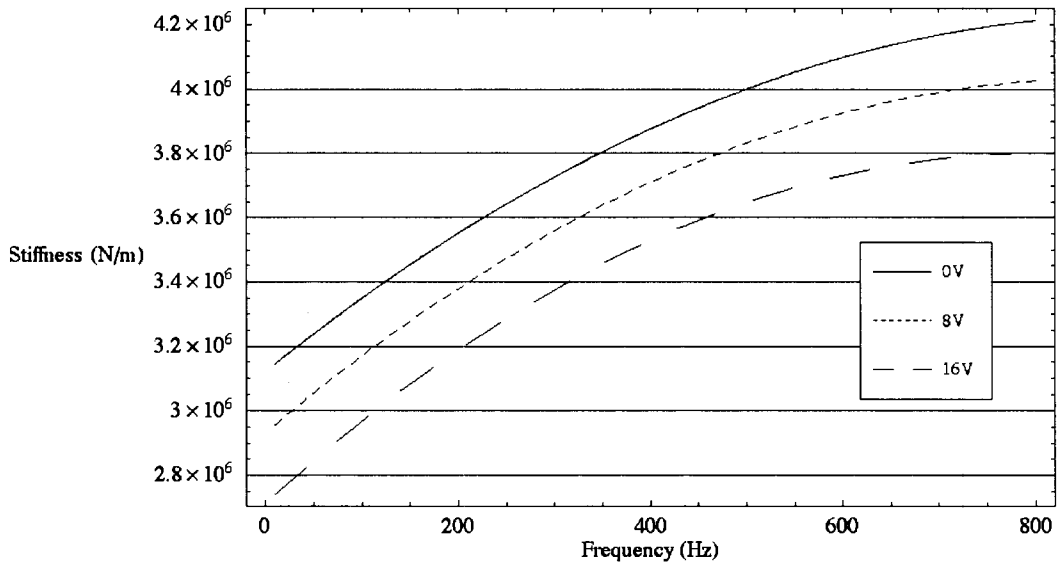

Figure 3.16: Real Stiffness Functions of the EFC Damper Quadratic Viscoelastic Model for the 0V, 8V, and 16V Sweep Transmissibility Datasets

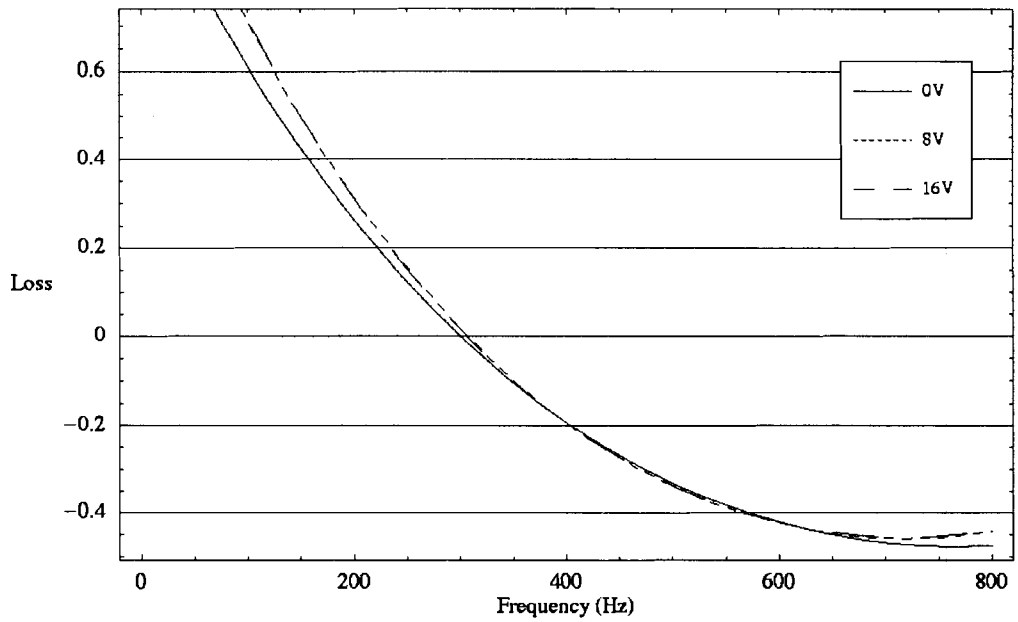

Figure 3.17: Complex Loss Functions of the EFC Damper Quadratic Viscoelastic Model for the 0V, 8V, and 16V Sweep Transmissibility Datasets

By inspection, the quadratic viscoelastic model appears to fit the transmissibility datasets as well as the linear viscoelastic model. However, unlike the linear viscoelastic model, the quadratic viscoelastic magnitude function values successfully track the transmissibility dataset values from 700Hz to 800Hz. The quadratic stiffness parameter function, similar to its linear counterpart, increases as a function of frequency, but decreases overall as a function of magnetic field strength. And, the quadratic loss parameter function, similar to its linear counterpart, decreases as a function of frequency, but unlike its linear counterpart, the quadratic loss parameter is unaffected by magnetic field strength. The quadratic loss parameter functions' immunity to magnetic field strength is exemplified by the 0V sweep and 8V sweep quadratic loss parameter function, which track each other consistently as shown in Figure 3.17. The acquired resonant

frequencies and transmissibility magnitudes from the quadratic viscoelastic magnitude functions are shown in Table 3.3.

Table 3.3: Acquired Resonant Frequencies from the Quadratic Viscoelastic Model

Electromagnet Voltage (V)	Resonant Frequency (Hz)	Transmissibility Magnitude	Resonant Frequency Percentage Change (%)
0	408.5	4.633	N/A
8	398.9	4.935	-2.353
16	389.5	5.349	-4.657

As with the linear viscoelastic model, the change in resonant frequency between the 0V and 16V transmissibility datasets is 4.7%. Comparing the resonant frequencies from both viscoelastic models, as shown in Table 3.4, shows that both the linear and quadratic viscoelastic models yield similar results.

Table 3.4: Comparison of the Acquired Resonant Frequencies from the Linear and Quadratic Viscoelastic Models

Electromagnet Voltage (V)	Linear Viscoelastic Resonant Frequency (Hz)	Quadratic Viscoelastic Resonant Frequency (Hz)
0	409.3	408.5
8	399.8	398.9
16	390.2	389.5

3.2.2.1 Quadratic Viscoelastic Model Error Analysis

The percentage fit error plots for the quadratic viscoelastic model are shown in Figure 3.18 to Figure 3.20.

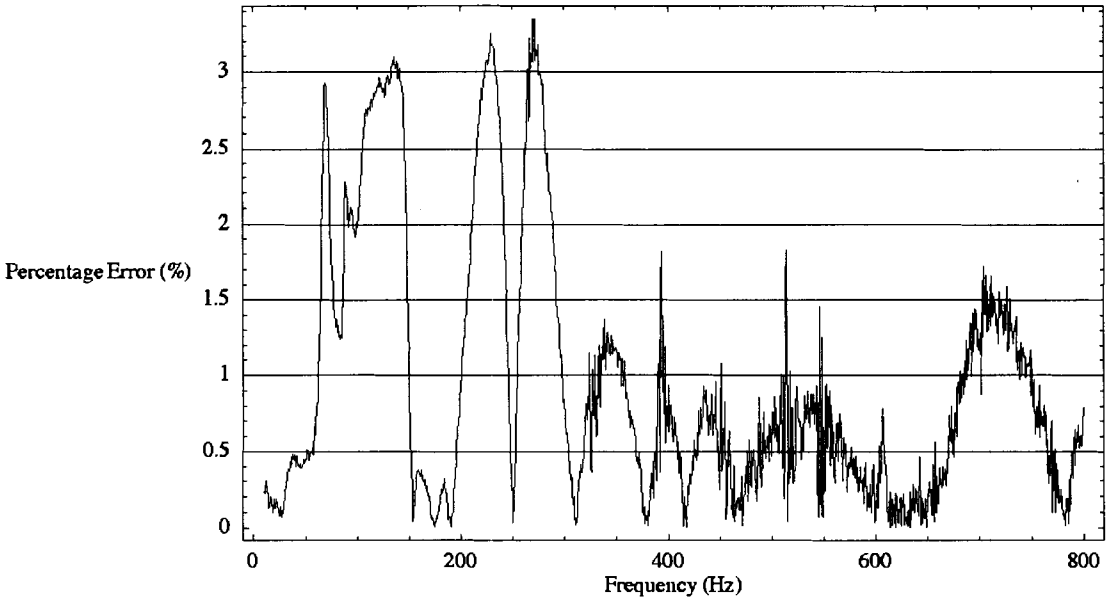

Figure 3.18: Percentage Fit Error of the Quadratic Viscoelastic Model for the 0V Sweep Transmissibility Dataset

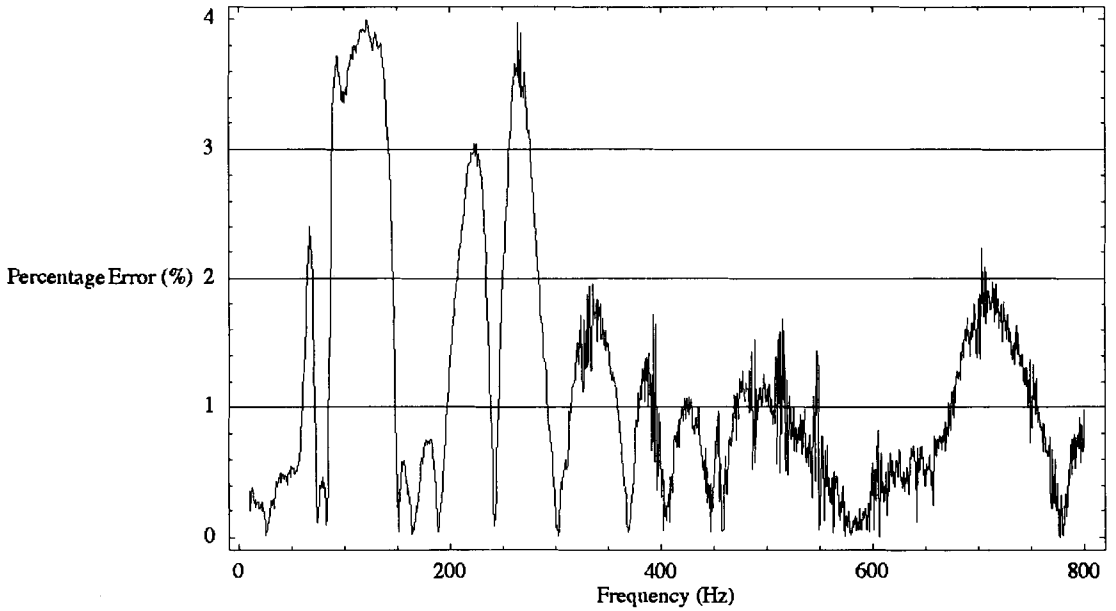

Figure 3.19: Percentage Fit Error of the Quadratic Viscoelastic Model for the 8V Sweep Transmissibility Dataset

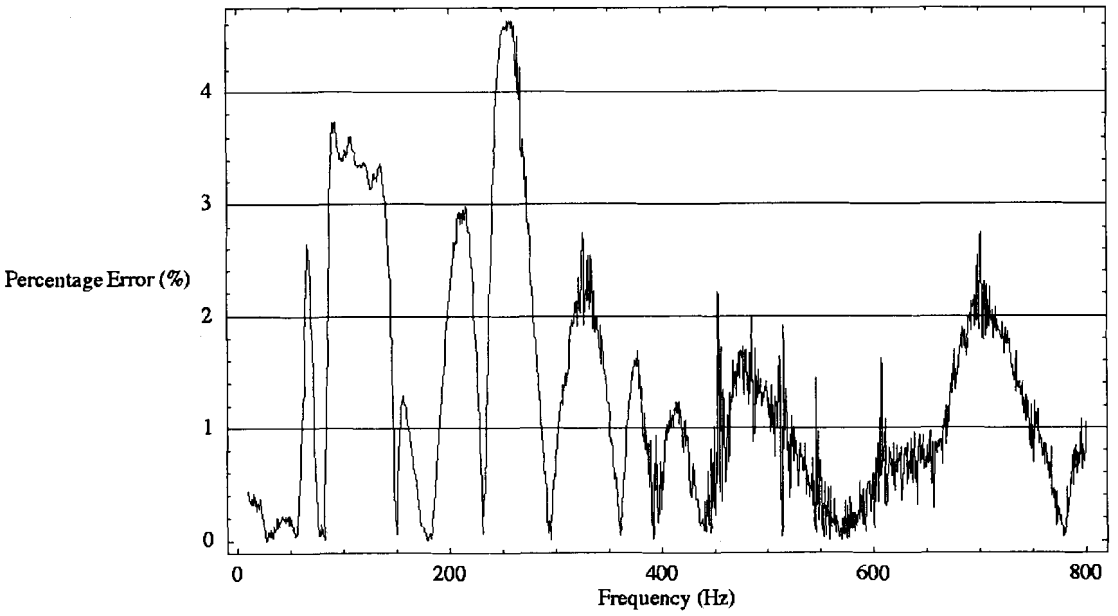

Figure 3.20: Percentage Fit Error of the Quadratic Viscoelastic Model for the 16V Sweep Transmissibility Dataset

The percentage fit error of the quadratic viscoelastic model is well within our desired 5% margin. The worst-case percentage fit error in the 16V sweep transmissibility dataset is at 4.8%. By comparison, worst-case percentage fit error for the linear viscoelastic model in the 16V sweep transmissibility dataset is at 12.4%. Therefore, given the significant improvement in percentage error, the quadratic viscoelastic model was determined to be the most accurate of the three models at describing the system level behaviour of the EFC damper.

3.3 EFC Damper Summary and Academic Contributions

As previously mentioned, because of the relatively low magnetic field strength of the EM-R2 electromagnets, it was impossible to see a large shift in the resonant frequency of the EFC damper test jig. The maximum shift in resonant frequency amounts to a 4.7% change from about 408.5Hz to 389.5Hz in the 0V and 16V frequency

sweeps, respectively. Also, the most accurate model that describes the changing physical properties of the EFC damper is non-linear. Regardless, the results from the EFC damper test jig experiments are extremely useful and promising. Firstly, the results show the capabilities of EFC components. Although, there are quite a few publications detailing the vibration damping capabilities of MRE components [33] – [37], the amount of research devoted to the vibration damping capabilities of EFC components is paltry by comparison. Secondly, the results are promising because they do show that off-the-shelf industrial electromagnets can be used to control an MR material component.

4 ELECTROMAGNET POWER AMPLIFIER MODELLING

4.1 Motivation for Power Amplifier Modelling

Implementing a semi-active MR material bushing in an automobile suspension, for structure-borne noise reduction, would require a controllable magnetic field to adjust the bushing stiffness. The controllable magnetic filed could be generated by an electromechanical assembly that moves rare earth magnets closer to or further from the semi-active bushing. Alternatively, electromagnets, directly coupled to the semi-active bushing, can be electronically controlled to generate a variable magnitude magnetic field. As part of our focus on electromagnetic control of MR material components, we researched the electronic control of electromagnets, specifically the power amplifiers for the electromagnets coupled to an MR material component. This part of our project on MR material vibration damping components is still at a very preliminary stage and, therefore, the power amplifier models presented in this chapter are based on ideal circuit elements. The focus of the power electronics modelling, as presented in this chapter, is on power amplifier feedback controller design. Specifically, large signal stable feedback controllers that have been derived directly from the power amplifier state equations. At this preliminary stage, the power amplifier modelling only encompasses a single feedback control design technique. All the power amplifiers and controllers were modelled in a power electronics simulation package called PSIM [60], a very popular power electronics simulator in both industry and academia. In addition, as in chapter 3, Mathematica was used for all mathematical derivations.

4.2 Power Amplifier Guidelines

Before beginning the power amplification modelling we came up a with a set of preliminary power amplifier guidelines, which are listed as follows:

- Power amplifier input voltage – 12V and/or 42V.

  The power amplifier input voltages were chosen to match current 12V car battery systems and the automotive industry's potential move towards 42V car battery systems in the future [38], [39].

- Power amplifier output voltage range – 1V to 20V.

  The power amplifier output voltage range was chosen to match the EM-R2 electromagnet terminal voltages from the EFC damper test jig experiments.

- Power amplifier load – series connected 65mH inductor and 25Ω resistor.

  This load was chosen to match the measured inductance and resistance of the EM-R2 electromagnet coil.

- Constant DC output current.

  Because the power amplifier load is based on the parameters of the EM-R2 DC electromagnet, I decided that the power amplifier must provide a fixed steady state output current for a fixed steady state output voltage.

4.3 Proposed Power Amplifier Topologies

Based on the power amplifier guidelines, we selected suitable power electronic topologies that could be used as power amplifiers. The chosen power electronics topologies are presented and explained in section 4.3.1.

4.3.1 DC-DC Converter

The power amplifier options are both based on DC-DC converter circuits. We avoided linear amplifiers because of their large size and low efficiency [40]. Additionally, we considered DC motor control amplifiers but could not use them because of their discontinuous current delivery [40].

Usually, by pulsing current through an intermediate inductive energy storage element [40], a DC-DC converter will convert a given input voltage to a regulated higher/lower/same magnitude output voltage with the same or opposite polarity. The output voltage range and polarity are functions of the chosen DC-DC converter circuit topology. For our electromagnet power amplifiers, we chose a step down, or buck DC-DC converter and a negative polarity output, or buck-boost DC-DC converter.

4.3.1.1 42V Buck Converter Power Amplifier

Because a buck converter steps down the input voltage to a lower output voltage, the buck converter power amplifier was modelled exclusively with a 42V input source. A schematic of the buck converter power amplifier circuit, illustrating key parameters and variables, is shown in Figure 4.1.

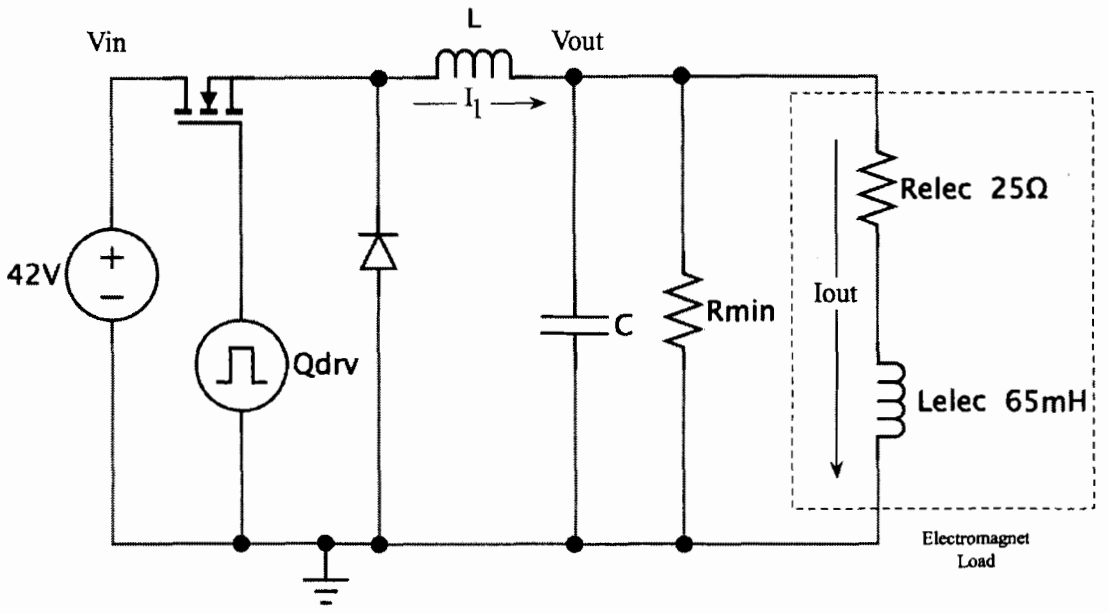

Figure 4.1: 42V Buck Converter Power Amplifier Circuit

In the buck converter circuit, the output voltage, V_{out}, is generated by pulsing current through the energy storage inductor, L. The output filter capacitor, C, reduces voltage ripple in the output voltage, V_{out}, and the larger the output filter capacitor, the smaller the output voltage ripple. The buck power amplifier output load is represented by the electromagnet load, the series connected resistor, R_{elec}, and inductor, L_{elec}, as well as a nominal resistance, R_{min}, in parallel with the electromagnet load. The nominal resistance, R_{min}, is included to provide a continuous current load to the buck power amplifier circuit because without continuous current draw, the energy storage inductor magnetic field collapses [40] and the buck power amplifier dynamic range is severely reduced.

The key buck converter parameters are given by

$$\frac{V_{out}}{V_{in}} = D \qquad \textbf{Equation 4.1}$$

which is the buck converter transfer function [40], and

$$L = \frac{(V_{in} - V_{out})\,D}{2\,\Delta i_L\,f_s} \qquad \textbf{Equation 4.2}$$

which is the energy storage inductor, L, design equation [40] where, V_{in} is the input voltage, V_{out} is the output voltage, f_s is the MOSFET switching signal frequency, D is the MOSFET switching signal duty cycle, and, Δi_L is the energy storage inductor ripple current peak value. The MOSFET switching signal frequency, f_s, was arbitrarily set to 10kHz. The energy storage inductor value was calculated from Equation 4.2 by iteratively changing the energy storage inductor ripple current peak value, Δi_L, until we arrived at a nominal inductor value of 3mH. The nominal resistance, R_{min}, was chosen to keep buck power amplifier in continuous conduction mode and arbitrarily set to 20Ω. Finally, the filter capacitor, C, was chosen to minimize output voltage ripple and arbitrarily set to 100μF. The buck power amplifier feedback controller designs and subsequent PSIM simulations are covered in sections 4.4 and 4.5.

4.3.1.2 Buck-Boost Converter Power Amplifier

Unlike the buck converter power amplifier, the buck-boost converter power amplifier inverts a positive input voltage to produce a negative output voltage. The output voltage magnitude of the buck-boost converter can be higher, lower, or equivalent to the input voltage magnitude. Therefore, the buck-boost power amplifier is modelled with both 12V and 42V input sources. A schematic of the buck-boost converter power amplifier circuit, illustrating key parameters and variables, is shown in Figure 4.2.

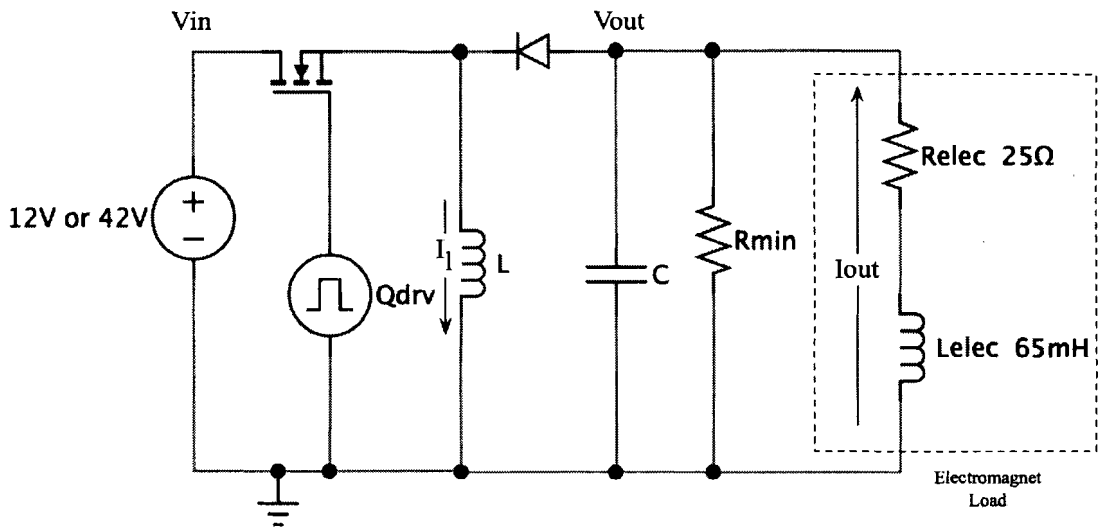

Figure 4.2: Buck-Boost Converter Power Amplifier Circuit

As with the buck converter circuit, output voltage, V_{out}, of the buck-boost converter circuit, is generated by pulsing current through the energy storage inductor, L. The output filter capacitor, C, reduces voltage ripple in the output voltage, V_{out}, and the larger the output filter capacitor, the smaller the output voltage ripple. The buck-boost power amplifier output load is represented by the electromagnet load, the series connected resistor, R_{elec}, and inductor, L_{elec}, as well as a nominal resistance, R_{min}, in parallel with the electromagnet load. Again, as with the buck power amplifier, the nominal resistance, R_{min}, is included to provide a continuous current load to the buck-boost power amplifier circuit because without continuous current draw the energy storage inductor magnetic field collapses [40] and the buck- boost power amplifier dynamic range is severely reduced.

The key buck converter parameters are given by

$$\frac{V_{out}}{V_{in}} = \frac{-D}{1-D} \qquad \textbf{Equation 4.3}$$

which is the buck-boost converter transfer function [40], and

$$L = \frac{V_{in}\, D}{2\,\Delta i_L\, f_s} \qquad \textbf{Equation 4.4}$$

which is the energy storage inductor, L, design equation [40] where, V_{in} is the input voltage, V_{out} is the output voltage, f_s, is the MOSFET switching signal frequency, D is the MOSFET switching signal duty cycle, and, Δi_L is the energy storage inductor ripple current peak value. The MOSFET switching signal frequency, f_s, was arbitrarily set to 10kHz. The energy storage inductor value was calculated from Equation 4.4 by iteratively changing the energy storage inductor ripple current peak value, Δi_L, until we arrived at a nominal inductor value of 3mH. The nominal resistance, R_{min}, was chosen to keep buck power amplifier in continuous conduction mode and arbitrarily set to 20Ω. Finally, the filter capacitor, C, was chosen to minimize output voltage ripple and arbitrarily set to between 100μF and 500μF. The buck-boost power amplifier feedback controller designs and subsequent PSIM simulations are covered in sections 4.4 and 4.5.

4.4 Design of the Power Amplifier Feedback Controller

Standard DC-DC converter feedback controller design is based on the DC-DC converter small signal model [41]. Although, the desired output voltage of some DC-DC converters can be changed or varied by user input, the DC-DC converter feedback controller is designed to maintain a fixed output voltage within ±10% due to system perturbations. While these small signal based feedback controllers work well for DC-DC

converters, they cannot be used for a power amplifier, which lacks a static operating output voltage. Therefore, the first step in designing the feedback controller was to find feedback control design techniques better suited to the buck and buck-boost power amplifiers.

An investigation of literature on DC-DC converters with large signal stability lead to two sets of feedback control design techniques. The first set of feedback control techniques are all based on large signal DC-DC converter models. Kawasaki et al. [42] and Chen et al. [43] design their controllers based on the bilinear large signal models of various DC-DC converter topologies, which are derived based on the switching action that intermittently pulses current through the energy storage element in a DC-DC converter. Leyva et al. [44] derived a feedback controller based on passivity conditions for the large signal model of a boost topology DC-DC converter.

The second set of feedback control techniques are based on the application of sliding mode control to DC-DC converter circuits. Both Nguyen et al.[45] and Wu et al. [46] indirectly implement sliding mode feedback controllers for the buck topology DC-DC converter. Whereas, Nguyen et al. explore proportional-integrald-derivative (PID) sliding mode feedback controllers for the buck converter, Wu et al. present a time averaged state space large signal model of the buck converter, which they subsequently analyzed to produce a pulse width modulation (PWM) controller via pole placement. Lin et al. [47] present the application of sliding mode control to a reduced order model of the buck converter. Finally, Mahdavi et al. [48] present sliding mode controllers for the buck converter, the boost converter, the buck-boost converter, and the Cúk converter, a topology which uses a capacitor as the engery storage element. We decided to use the

techniques presented by Mahdavi et al. because they were extremely easy to implement in PSIM. The control equations derived from using techniques presented by Mahdavi et al. were directly applied in the PSIM simulations. The basics of sliding mode control, as well as our various feedback controller designs are presented in the sections 4.4.1 and 4.4.2.

4.4.1 Sliding Mode Control

Sliding mode control is a field of study in and of itself. Because sliding mode control is beyond the scope of this thesis, only a very simple explanation of sliding mode control is given here. More detailed information on sliding mode control is covered by Utkin et al., Young et al. and Sira-Ramirez [49] – [55].

Sliding mode control works by enforcing a system level condition or set of conditions, *s*, [56]; for example, by forcing a system output or state variable to a desired or reference value. The sliding mode feedback controller uses some form of switching action to maintain the desired system output or state variable value. The mathematical definition is given by

$$s = 0 \qquad \textbf{Equation 4.5}$$

where, *s*, represents a set of system outputs or state variables forced to a desired value and the necessary constraint on *s* for the existence of sliding mode control is given by

$$s\dot{s} < 0 \qquad \textbf{Equation 4.6}$$

where, $\dot{s}$, is the derivative of *s* with respect to time.

As an example, Mahdavi et al. set the output voltage of a DC-DC converter to a desired value with

$$s = V_{out}[t] - K = 0 \qquad \textbf{Equation 4.7}$$

where, V_{out} is the DC-DC converter output voltage, and K is the desired output voltage. The necessary sliding mode existence constraint is then given by

$$(V_{out}[t] - K)\ \dot{V}_{out}[t] < 0 \qquad \textbf{Equation 4.8}$$

The mathematical form of the sliding mode feedback controllers for the various power amplifiers are given in section 4.4.2.

4.4.2 Power Amplifier Sliding Mode Feedback Controllers

We decided to design two types of feedback controllers for the 42V buck, 12V buck-boost, and 42V buck-boost power amplifiers. The voltage sliding mode feedback controller controls the power amplifier output voltage while ignoring the existence of the electromagnet load, whereas the current sliding mode feedback controller directly controls the current in the electromagnet load. The voltage sliding mode controllers are identical to those proposed by Mahdavi et al., and we derived the current sliding mode controllers using the same techniques as Mahdavi et al. The four different sliding mode feedback controllers are derived and shown in sections 4.4.2.1 to 4.4.2.4.

4.4.2.1 Voltage Sliding Mode Feedback Controller for the 42V Buck Power Amplifier

Mahdavi et al. show that the buck converter state space equations are given by

$$\dot{I}_L[t] = \frac{-V_{out}[t]}{L} + \frac{D[t]\,V_{in}[t]}{L} \qquad \textbf{Equation 4.9}$$

$$\dot{V}_{out}[t] = \frac{I_L[t]}{C} - \frac{V_{out}[t]}{C\,R_{min}} \qquad \textbf{Equation 4.10}$$

where, V_{in} is the input voltage, V_{out} is the output voltage, D is the MOSFET switching signal duty cycle, L is the energy storage inductor, I_l is the energy storage inductor current, C is the output filter capacitor, and R_{min} is treated as the buck converter load. The sliding mode condition is defined in terms of the desired output voltage, K, and the actual output voltage, V_{out}, as shown in Equation 4.7. Additionally, the corresponding sliding mode constraint inequality is then given by Equation 4.8. Mahdavi et al. then propose a 'convergence relationship'

$$\dot{V}_{out}[t] = -\lambda\,(V_{out}[t] - K), \qquad \textbf{Equation 4.11}$$

which mathematically satisfies the sliding mode constraint inequality shown in Equation 4.8.

The controller equation is generated by back substituting Equation 4.11 through the buck converter state equations and solving for the MOSFET switching signal duty cycle function, D. The 'convergence factor', λ, in Equation 4.11, affects the power amplifier settling time. The voltage sliding mode feedback controller equation for the buck converter power amplifier, as derived by Mahdavi et al. and implemented in our PSIM simulations is given by

$$D[t] = \frac{K + a\,(V_{out}[t] - K)}{V_{in}[t]}, \text{ where}$$

$$a = L C \lambda^2 - \frac{L \lambda}{R_{min}} + 1 .$$

Equation 4.12

4.4.2.2 Current Sliding Mode Feedback Controller for the 42V Buck Power Amplifier

By treating the electromagnet current as a state variable, we derived a set of buck converter state space equations given by

$$\dot{I}_L[t] = \frac{-V_{out}[t]}{L} + \frac{D[t]\,V_{in}[t]}{L}$$

Equation 4.13

$$\dot{V}_{out}[t] = \frac{I_L[t]}{C} - \frac{I_{out}[t]}{C} - \frac{V_{out}[t]}{C\,R_{min}}$$

Equation 4.14

$$\dot{I}_{out}[t] = \frac{-R_{elec}\,I_{out}[t]}{L_{elec}} + \frac{V_{out}[t]}{L_{elec}}$$

Equation 4.15

where, V_{in} is the input voltage, V_{out} is the output voltage, D is the MOSFET switching signal duty cycle, L is the energy storage inductor, I_l is the energy storage inductor current, I_{out} is the electromagnet current, L_{elec} is the electromagnet inductance, R_{elec} is the electromagnet resistance, C is the output filter capacitor, and R_{min} is the nominal resistance in parallel with the electromagnet. Because of our interest in directly controlling the electromagnet current, the sliding mode condition is defined in terms of the desired electromagnet current, K, and the actual electromagnet current, I_{out}, as given by

$$s = I_{out}[t] - K = 0 \qquad \textbf{Equation 4.16}$$

and, the corresponding sliding mode constraint inequality is then given by

$$(I_{out}[t] - K)\, \dot{I}_{out}[t] < 0. \qquad \textbf{Equation 4.17}$$

We used a convergence relationship, given by

$$\dot{I}_{out}[t] = -\lambda\,(I_{out}[t] - K), \qquad \textbf{Equation 4.18}$$

that mathematically satisfies the sliding mode constraint inequality shown in Equation 4.17. By back substituting the Equation 4.18 convergence relationship through the 42V buck power amplifier state space equations, the actual controller equation is yielded by solving for the MOSFET switching signal duty cycle, *D*. The current sliding mode feedback controller equation for the buck power amplifier, implemented in our PSIM simulations is given by

$$D[t] = \frac{(L\,\lambda\,a\,(K - I_{out}[t]) + R_{min}\,V_{out}[t])}{R_{min}\,V_{in}[t]}, \text{ where} \qquad \textbf{Equation 4.19}$$

$$a = (R_{clec} + R_{min} - (L_{elec} + C\,R_{clec}\,R_{min})\,\lambda + C\,L_{clec}\,R_{min}\,\lambda^2).$$

4.4.2.3 Voltage Sliding Mode Feedback Controller for the Buck-Boost Power Amplifier

Mahdavi et al. show that the buck-boost converter state space equations are given by

$$\dot{I}_L[t] = \frac{(1 - D[t])\, V_{out}[t]}{L} + \frac{D[t]\, V_{in}[t]}{L} \qquad \textbf{Equation 4.20}$$

$$\dot{V}_{out}[t] = \frac{(D[t] - 1)\, I_L[t]}{C} - \frac{V_{out}[t]}{C\, R_{min}} \qquad \textbf{Equation 4.21}$$

where, V_{in} is the input voltage, V_{out} is the output voltage, D is the MOSFET switching signal duty cycle, L is the energy storage inductor, I_l is the energy storage inductor current, C is the output filter capacitor, and R_{min} is treated as the buck-boost converter load. As with the buck converter, the sliding mode condition is defined in terms of the desired output voltage, K, and the actual output voltage, V_{out}, as shown in Equation 4.7. Additionally, the corresponding sliding mode constraint inequality and matching convergence relationship is then given by Equation 4.8 and Equation 4.11, respectively.

The controller equation is generated by back substituting Equation 4.11 through the buck converter state equations and solving for the MOSFET switching signal duty cycle function, D. The voltage sliding mode feedback controller equation for the buck-boost converter power amplifier, as derived by Mahdavi et al. and implemented in our PSIM simulations is given by

$$D[t] = 1 + \frac{V_{in}[t] + \sqrt{V_{in}^2[t] + a\ (V_{out}[t] - V_{in}[t])\,(V_{out}[t] - K)}}{2\ (V_{out}[t] - V_{in}[t])},$$

where **Equation 4.22**

$$a = 4\,L\,C\,\lambda - \frac{4\,L}{R_{min}}.$$

4.4.2.4 Current Sliding Mode Feedback Controller for the Buck-Boost Power Amplifier

By treating the electromagnet current as a state variable, we derived a set of buck-boost converter state space equations given by

$$\dot{I}_L[t] = \frac{V_{out}[t]}{L} + \frac{-D[t]\,V_{out}[t]}{L} + \frac{D[t]\,V_{in}[t]}{L} \qquad \textbf{Equation 4.23}$$

$$\dot{V}_{out}[t] = \frac{-I_L[t]}{C} + \frac{D[t]\,I_L[t]}{C} - \frac{I_{out}[t]}{C} - \frac{V_{out}[t]}{C\,R_{min}} \qquad \textbf{Equation 4.24}$$

$$\dot{I}_{out}[t] = \frac{-R_{elec}\,I_{out}[t]}{L_{elec}} + \frac{V_{out}[t]}{L_{elec}} \qquad \textbf{Equation 4.25}$$

where, V_{in} is the input voltage, V_{out} is the output voltage, D is the MOSFET switching signal duty cycle, L is the energy storage inductor, I_l is the energy storage inductor current, I_{out} is the electromagnet current, L_{elec} is the electromagnet inductance, R_{elec} is the electromagnet resistance, C is the output filter capacitor, and R_{min} is the nominal resistance in parallel with the electromagnet. Because of our interest in directly controlling the electromagnet current we used the same sliding mode condition, Equation 4.16, constraint equality, Equation 4.17, and convergence relationship, Equation 4.18, as the current sliding mode controller for the buck power amplifier. By back substituting the Equation 4.18 convergence relationship through the buck-boost power amplifier state space equations, the actual controller equation is yielded by solving for the MOSFET switching signal duty cycle, D. The current sliding mode feedback controller equation for the buck-boost power amplifier, implemented in our PSIM simulations is given by

$$D[t] = \frac{\left(2 R_{min} V_{out}[t] - R_{min} V_{in}[t] + b \sqrt{(-2 R_{min} V_{out}[t] + R_{min} V_{in}[t])^2 - 4 R_{min} (V_{out}[t] - V_{in}[t])}\right)}{2 R_{min} (V_{out}[t] - V_{in}[t])},$$

where **Equation 4.26**

$$b = \sqrt{((I_{out}[t] - K) L \lambda (-R_{elec} + L_{elec} \lambda) + R_{min} (V_{out}[t] + (I_{out}[t] - K) L \lambda (-1 + C \lambda (R_{elec} - L_{elec})))}.$$

4.5 PSIM Power Amplifier Simulations

As a simulation package, PSIM is extremely easy to use; all circuits can be entered as electronic or electrical schematics and the package provides additional control and mathematical blocks such as summers, multipliers, dividers, integrators, differentiators, as well as arbitrary mathematical blocks that allow user defined mathematical functions. Therefore, for a given power amplifier, the circuits and circuit elements, shown in Figure 4.1 and Figure 4.2, were represented by an electronic schematic, and the controller equations from section 4.4 were represented by the control and mathematical blocks.

4.5.1 PWM Circuit

The MOSFET switching signal for all the power amplifiers was generated by a PWM circuit that converts the duty cycle signal of the sliding mode feedback controller to a PWM signal. A Schematic of the PWM circuit configured to produce a 50% duty cycle square wave is shown in Figure 4.3.

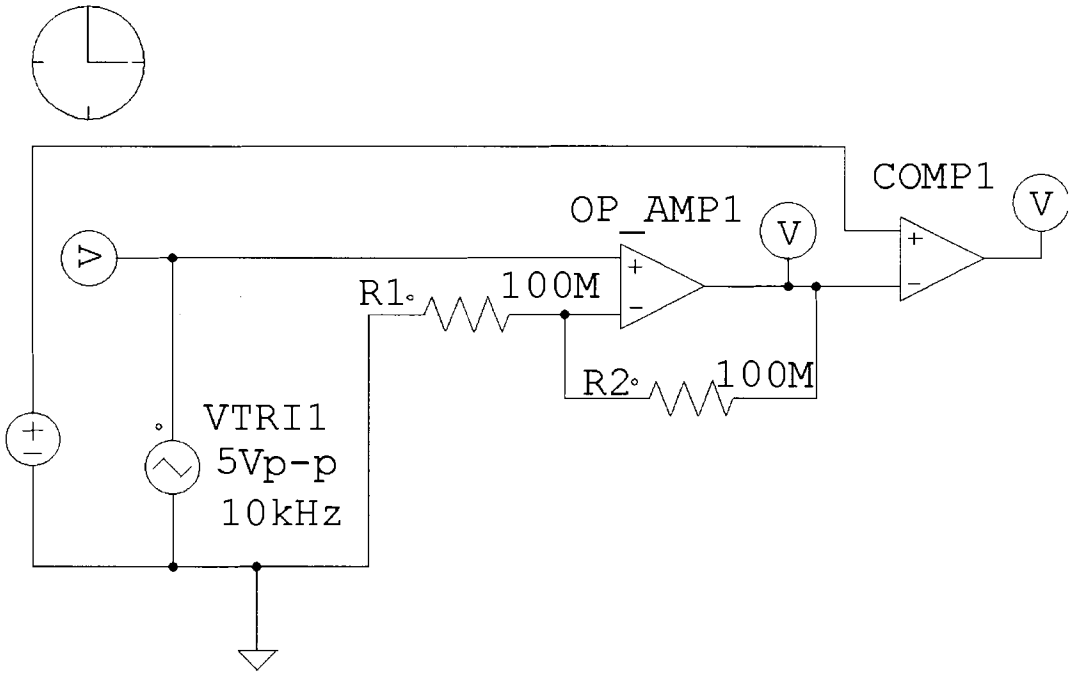

Figure 4.3: Schematic of PWM Circuit Schematic

The PWM circuit consists of a 10KHz, 5Vpp triangular signal generator, which is buffered by a non-inverting op-amp amplifier with a gain of 2V/V. The resulting 10Vpp triangular signal is compared against the duty cycle signal from the sliding mode feedback controller to produce a square wave with the appropriate duty cycle, an example of which is illustrated in Figure 4.4. The Figure 4.4 50% duty cycle is produced by comparing the 10Vpp triangular signal against a 5V DC voltage source.

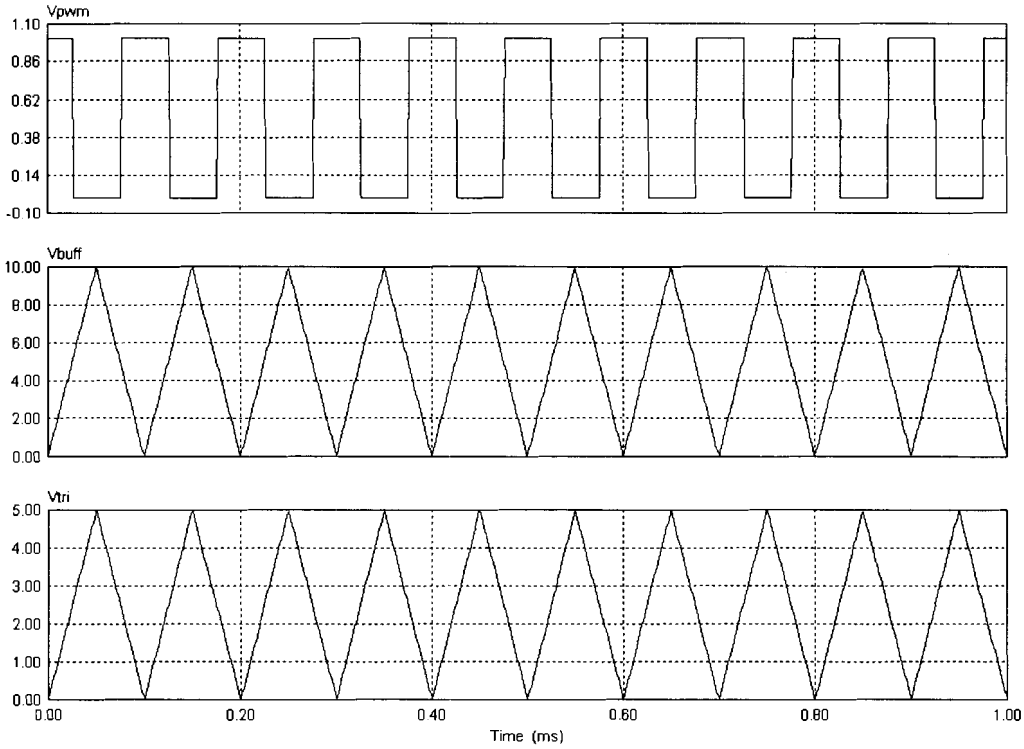

Figure 4.4: PWM Circuit Waveforms
Vtri – 10kHz, 5Vpp Triangular Wave Form
Vbuff – Buffered 10kHz, 5Vpp Triangular Wave Form
Vpwm – 10kHz, 50% Duty Cycle Square Wave

4.5.2 PSIM Simulation Process

Each power amplifier simulation was run for 0.5 seconds and of consisted of two successive transient responses. The first transient response occurred at power amplifier startup, and the second transient response was generated by instantly reducing the power amplifier input voltage by as much as 50% at 0.25 seconds. Additionally, PSIM has a built in parameter sweeping function, which was used to simultaneously produce three separate output voltages or currents in each simulation.

The power amplifiers operate stably for only certain ranges of the convergence factor, λ. Simulating a power amplifier with a non-stable λ value resulted in a near zero output voltage or electromagnet load current. Therefore, each simulation was run twice

with two different λ values. The results of each power amplifier simulation are presented in sections 4.5.3 to 4.5.8.

4.5.3 42V Buck Power Amplifier with Voltage Sliding Mode Feedback Controller

A schematic of the 42V buck power amplifier and its voltage sliding mode feedback controller is shown in Figure 4.5.

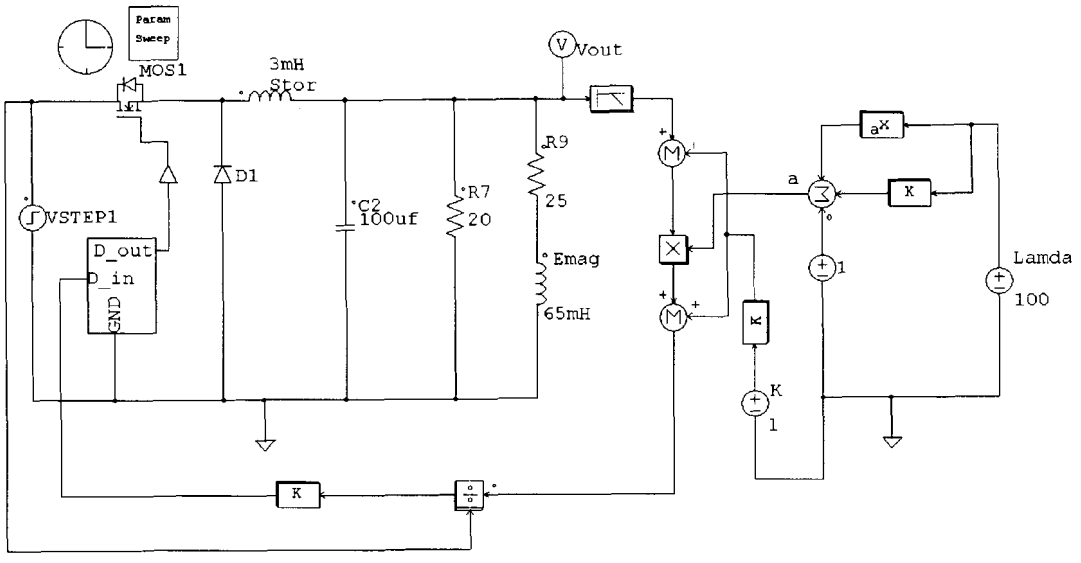

Figure 4.5: Voltage Mode Controlled 42V Buck Power Amplifier Schematic

The simulation parameters for this power amplifier were:

- Input voltage drop at 0.25 seconds – 42V to 21V.
- Output voltages produced – 1V, 10.5V, and 20V.
- Convergence factor, λ, values tested – 100, and 800.

The output voltage and electromagnet load current waveforms for each simulation are shown in Figure 4.6 and Figure 4.7.

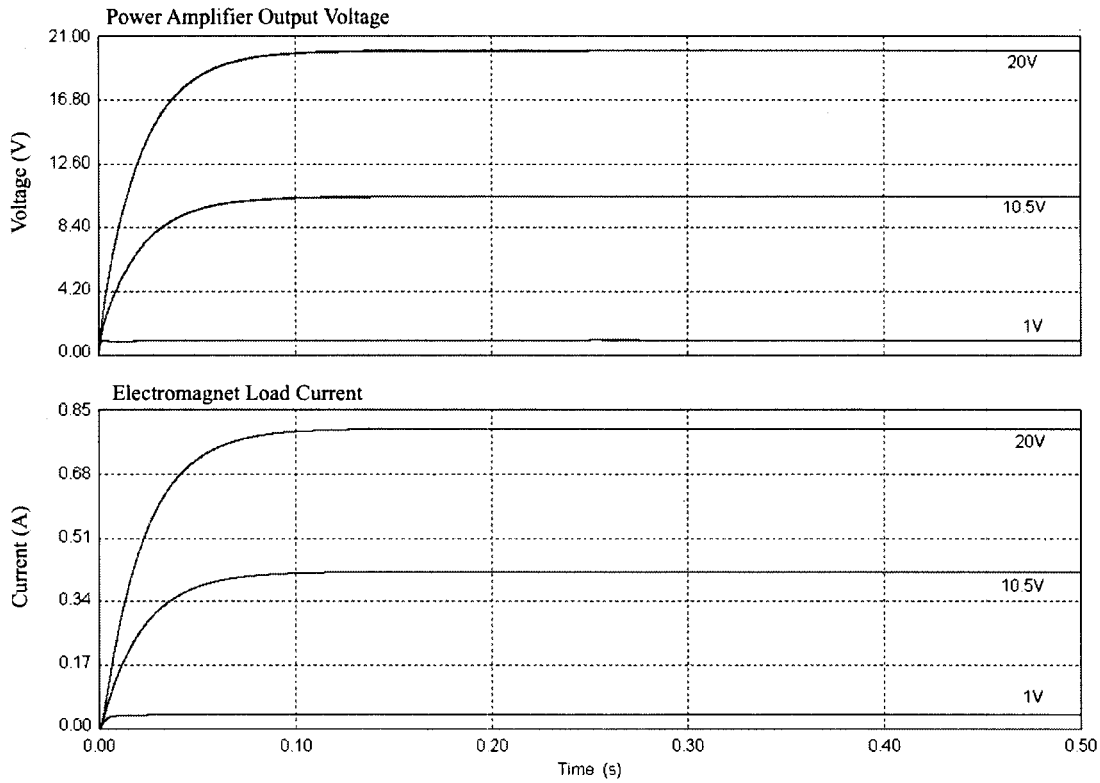

Figure 4.6: Voltage Mode Controlled 42V Buck Power Amplifier Output Voltage and Electromagnet Load Current, $\lambda = 100$

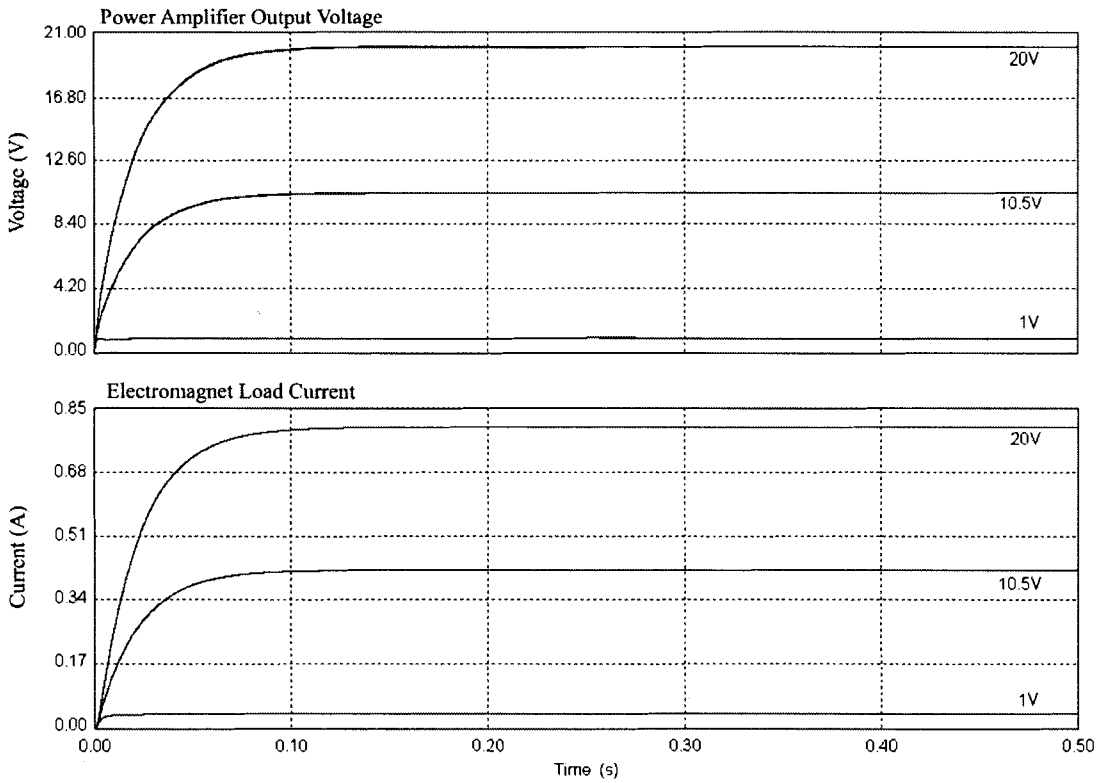

Figure 4.7: Voltage Mode Controlled 42V Buck Power Amplifier Output Voltage and Electromagnet Load Current, $\lambda = 800$

The voltage mode buck power amplifier's resilience against the change in input voltage from 42V to 21V that occurs at 0.25 seconds is most evident in the simulation results. With the exception of a low amplitude transient artefact in the power amplifier voltage output at 1V, there is no change in the power amplifier output voltage or electromagnet load current. Also, changing the convergence factor, λ, has little or no effect on the power amplifier startup time or transients. In both simulations, the power amplifier output voltage and electromagnet load current respond as if the power amplifier were an over-damped system.

4.5.4 42V Buck Power Amplifier with Current Sliding Mode Feedback Controller

A schematic of the 42V buck power amplifier and its current sliding mode feedback controller is shown in Figure 4.8.

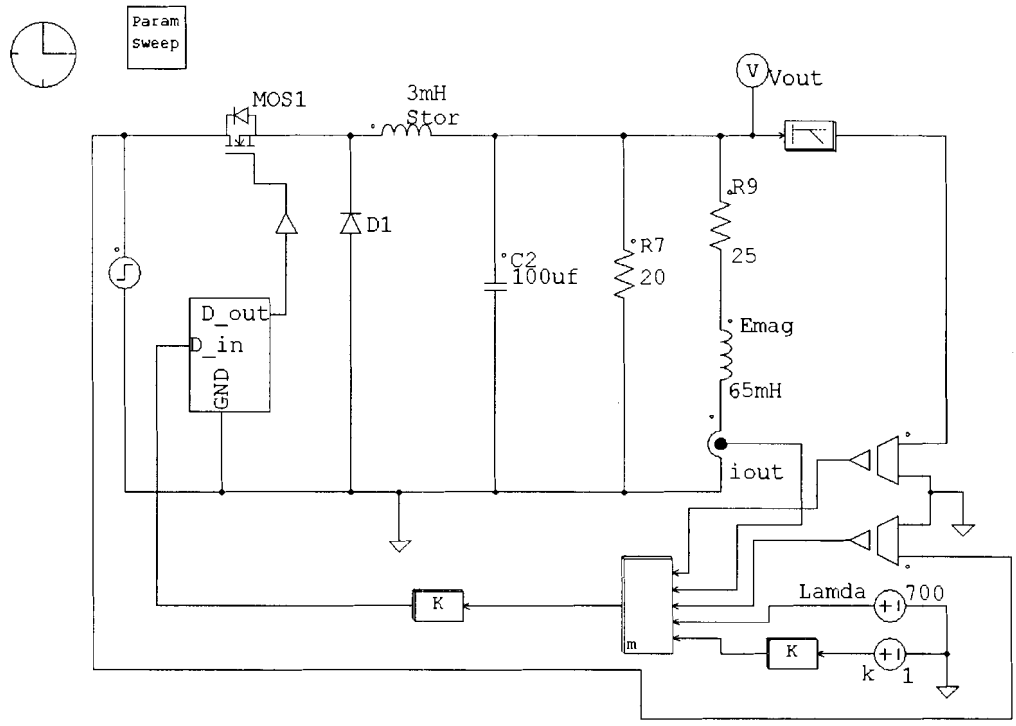

Figure 4.8: Current Mode Controlled 42V Buck Power Amplifier Schematic

The simulation parameters for this power amplifier were:

- Input voltage drop at 0.25 seconds – 42V to 30V.
- Output currents produced – 0.04A, 0.52A, and 1A.
- Convergence factor, λ, values tested – 100, and 700.

The electromagnet load current and output voltage waveforms for each simulation are shown in Figure 4.9 and Figure 4.10.

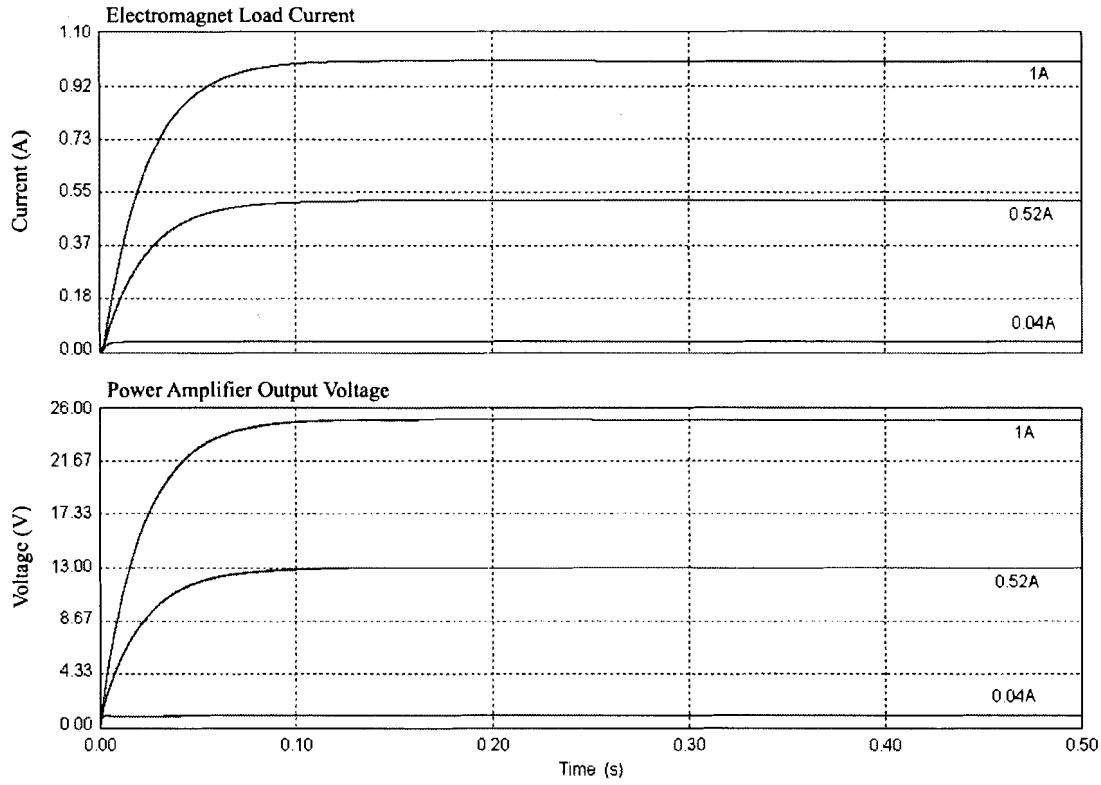

Figure 4.9: Current Mode Controlled 42V Buck Power Amplifier Electromagnet Load Current and Output Voltage, $\lambda = 100$

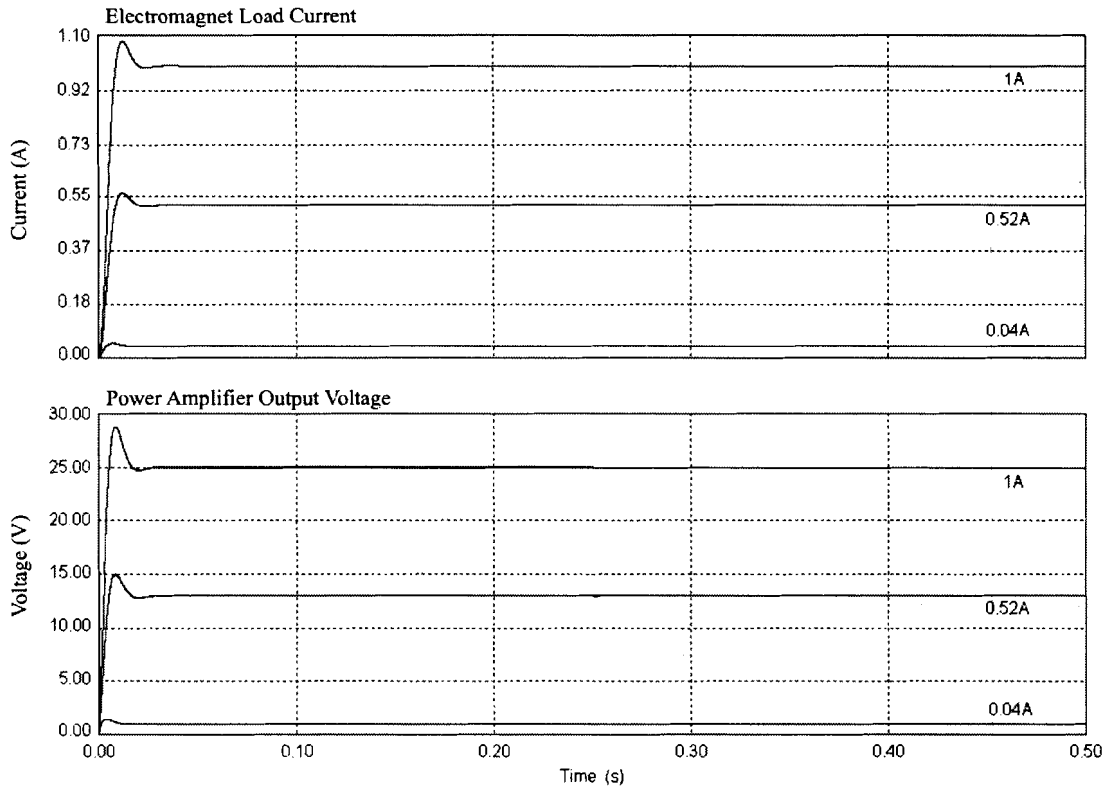

Figure 4.10: Current Mode Controlled 42V Buck Power Amplifier Electromagnet Load Current and Output Voltage, $\lambda = 700$

As with the voltage mode buck power amplifier, the current mode buck power amplifier's resilience against the change in input voltage from 42V to 30V that occurs at 0.25 seconds is most evident in the simulation results. With the exception of a low amplitude transient artefact in the power amplifier voltage output at 1V, there is no change in the power amplifier output voltage or electromagnet load current. But, unlike the voltage mode buck power amplifier, increasing the convergence factor, λ, changes the power amplifier from an over-damped to an under-damped system. Specifically, increasing the λ value increases the electromagnet load current and output voltage rise times at the expense of added overshoot.

4.5.5 12V Buck-Boost Power Amplifier with Voltage Sliding Mode Feedback Controller

A schematic of the 12V buck-boost power amplifier and its voltage sliding mode feedback controller is shown in Figure 4.11.

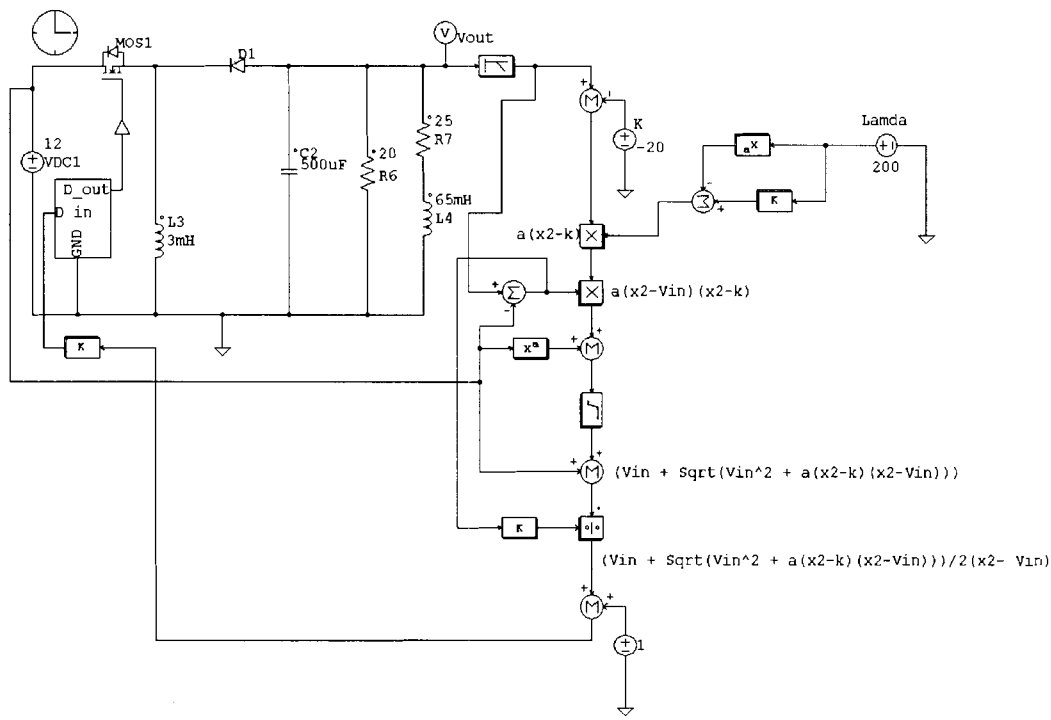

Figure 4.11: Voltage Mode Controlled 12V Buck-Boost Power Amplifier Schematic

The simulation parameters for this power amplifier were:

- Input voltage drop at 0.25 seconds – 12V to 6V.
- Output voltages produced – -1V, -10.5V, and -20V.
- Convergence factor, λ, values tested – 200, and 1600.

The output voltage and electromagnet load current waveforms for each simulation are shown in Figure 4.12 and Figure 4.13.

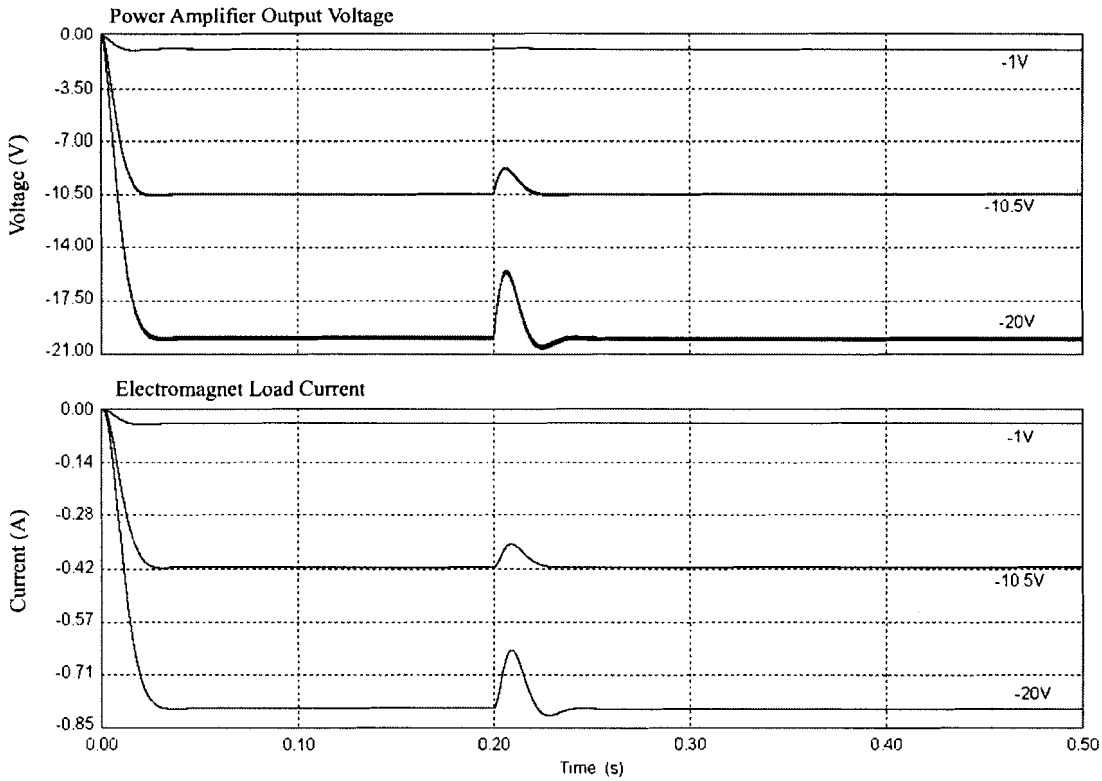

Figure 4.12: Voltage Mode Controlled 12V Buck-Boost Power Amplifier Output Voltage and Electromagnet Load Current, $\lambda = 200$

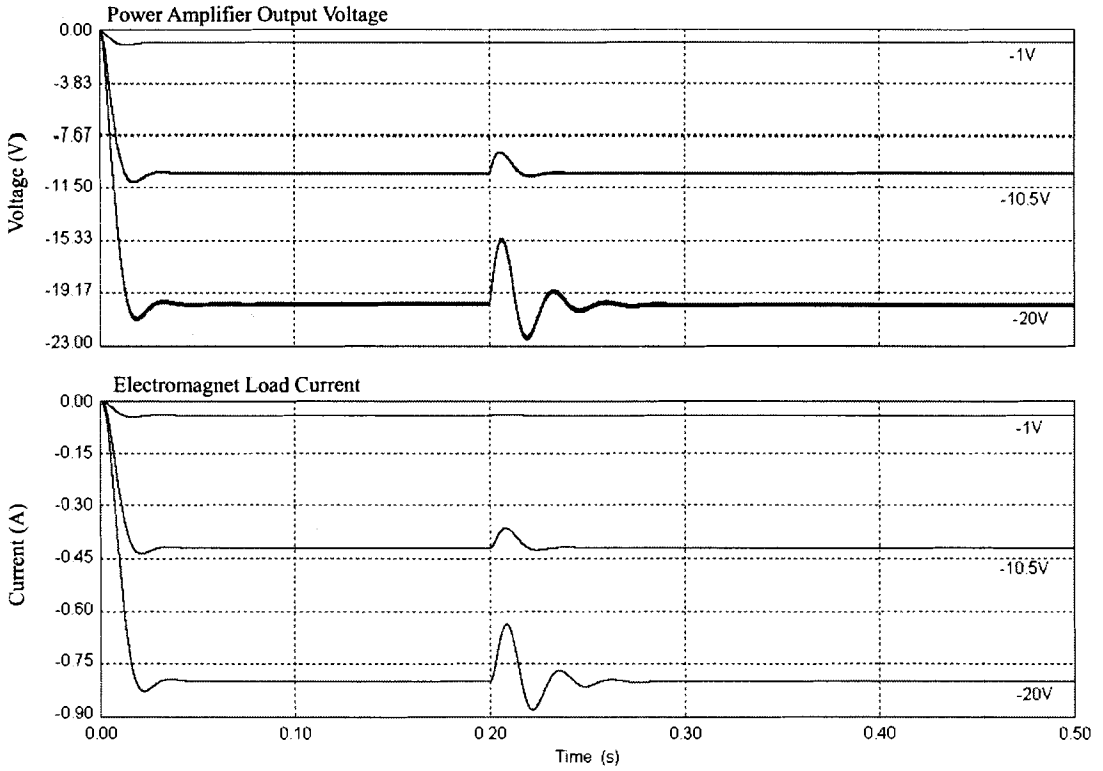

Figure 4.13: Voltage Mode Controlled 12V Buck-Boost Power Amplifier Output Voltage and Electromagnet Load Current, $\lambda = 1600$

Unlike the buck power amplifiers, the 12V voltage mode buck-boost power amplifier reacts adversely to large drops in input voltage. Significant transient disturbances are noticeable in the power amplifier output voltage and electromagnet load current when the input voltage changes from 12V to 6V at 0.25 seconds. With respect to the convergence factor, λ, the power amplifier always responds like an under-damped system. However, increasing the λ value increases the power amplifier output voltage and load current rise times at the expense of added overshoot and a longer settling time.

4.5.6 12V Buck-Boost Power Amplifier with Current Sliding Mode Feedback Controller

A schematic of the 12V buck-boost power amplifier and its current sliding mode feedback controller is shown in Figure 4.14.

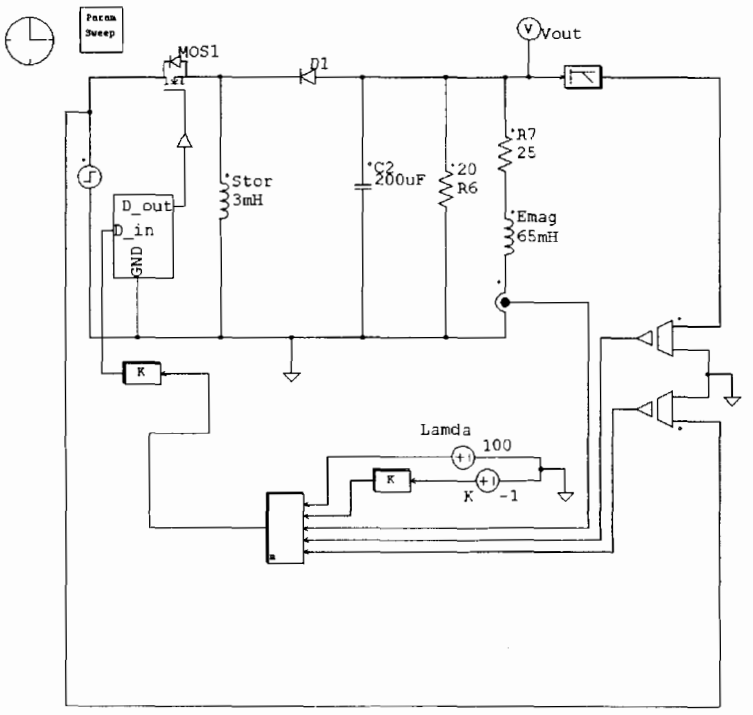

Figure 4.14: Current Mode Controlled 12V Buck-Boost Power Amplifier Schematic

The simulation parameters for this power amplifier were:

- Input voltage drop at 0.25 seconds – 12V to 6V.
- Output currents produced – -0.04A, -0.52A, and -1A.
- Convergence factor, λ, values tested – 100, and 400.

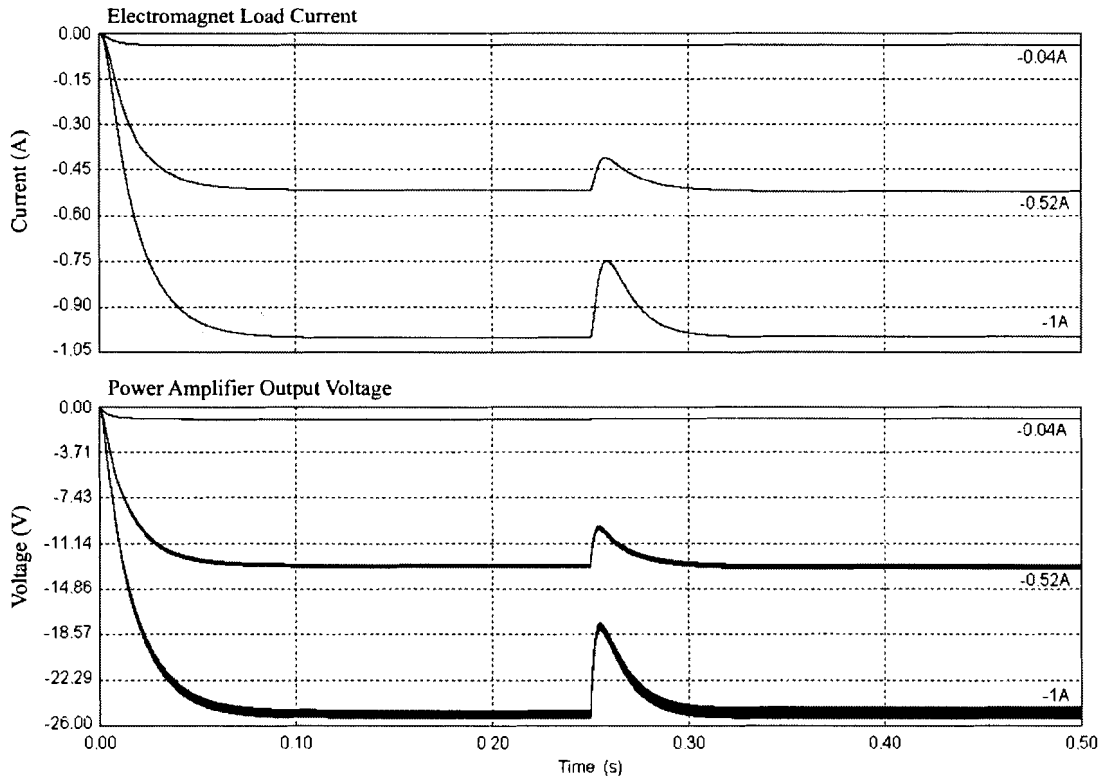

Figure 4.15: Current Mode Controlled 12V Buck-Boost Power Amplifier Electromagnet Load Current and Output Voltage, $\lambda = 100$

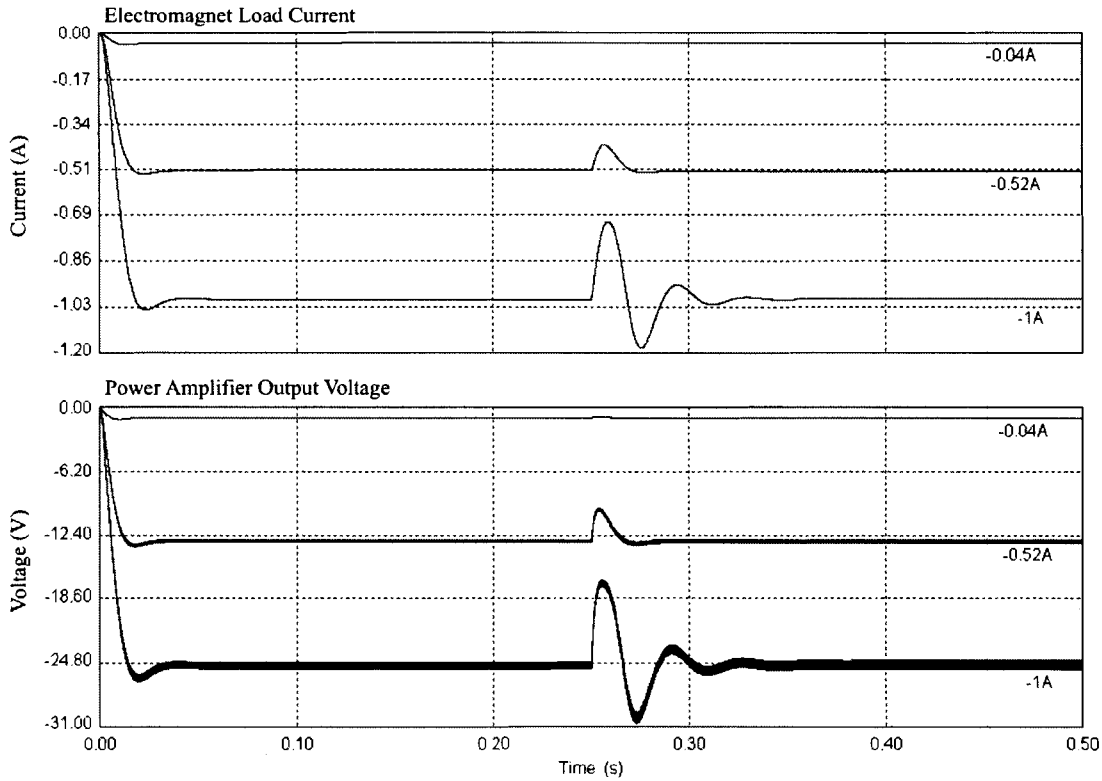

Figure 4.16: Current Mode Controlled 12V Buck-Boost Power Amplifier Electromagnet Load Current and Output Voltage, $\lambda = 400$

Just like its voltage mode counterpart, the 12V current mode buck-boost power amplifier reacts adversely to large drops in input voltage. Significant transient disturbances are noticeable in the power amplifier electromagnet load current and output voltage when the input voltage changes from 12V to 6V at 0.25 seconds. With respect to the convergence factor, λ, the power amplifier response changes from an over-damped system to an under-damped system as λ increases from 100 to 400. Therefore, increasing the λ value increases the power amplifier electromagnet load current and output voltage rise times at the expense of added overshoot and a longer settling time.

4.5.7 42V Buck-Boost Power Amplifier with Voltage Sliding Mode Feedback Controller

A schematic of the 42V buck-boost power amplifier and its voltage sliding mode feedback controller is shown in Figure 4.17.

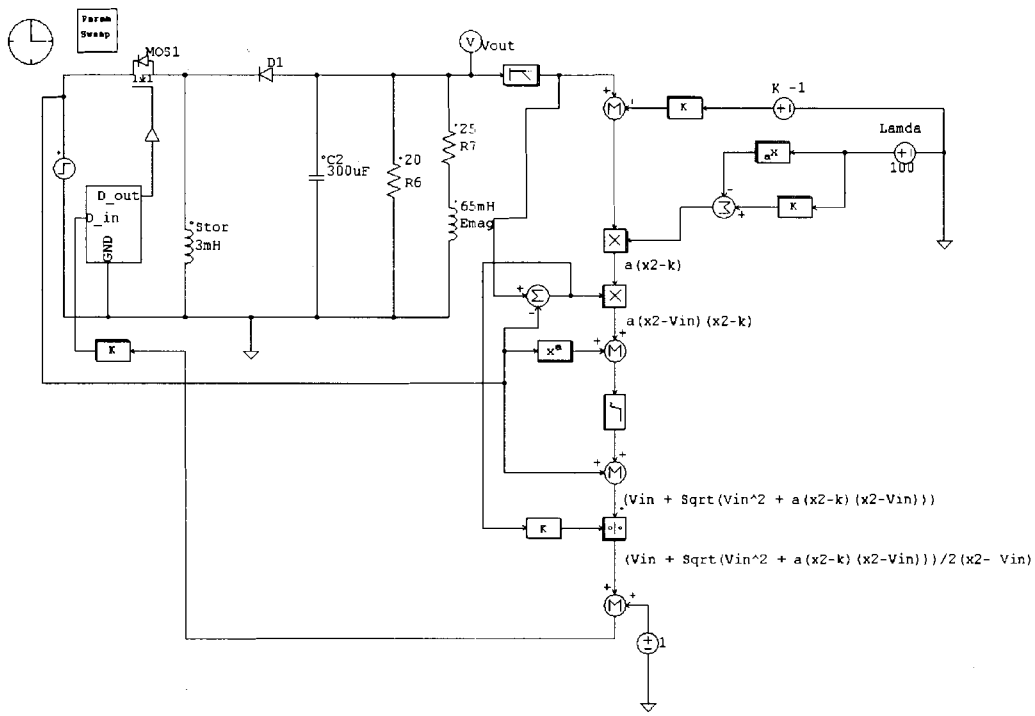

Figure 4.17: Voltage Mode Controlled 42V Buck-Boost Power Amplifier Schematic

The simulation parameters for this power amplifier were:

- Input voltage drop at 0.25 seconds – 42V to 21V.
- Output voltages produced – -1V, -10.5V, and -20V.
- Convergence factor, λ, values tested – 40, and 100.

The output voltage and electromagnet load current waveforms for each simulation are shown in Figure 4.18 and Figure 4.19.

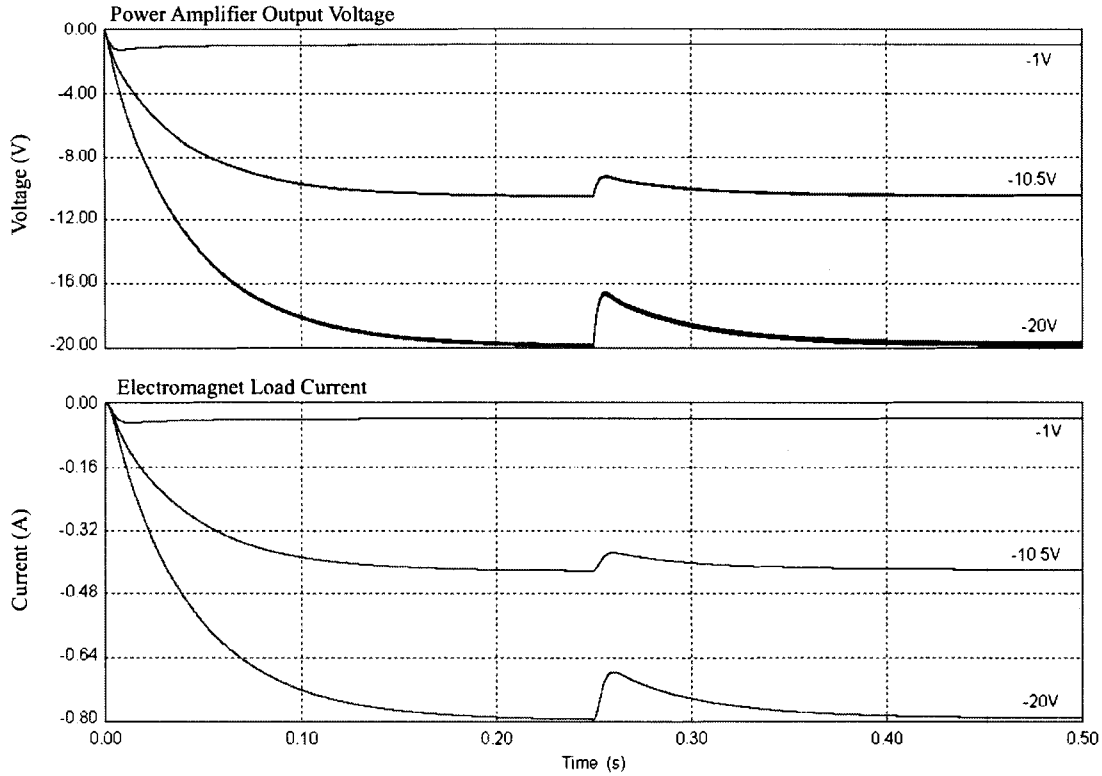

Figure 4.18: Voltage Mode Controlled 42V Buck-Boost Power Amplifier Output Voltage and Electromagnet Load Current, $\lambda = 40$

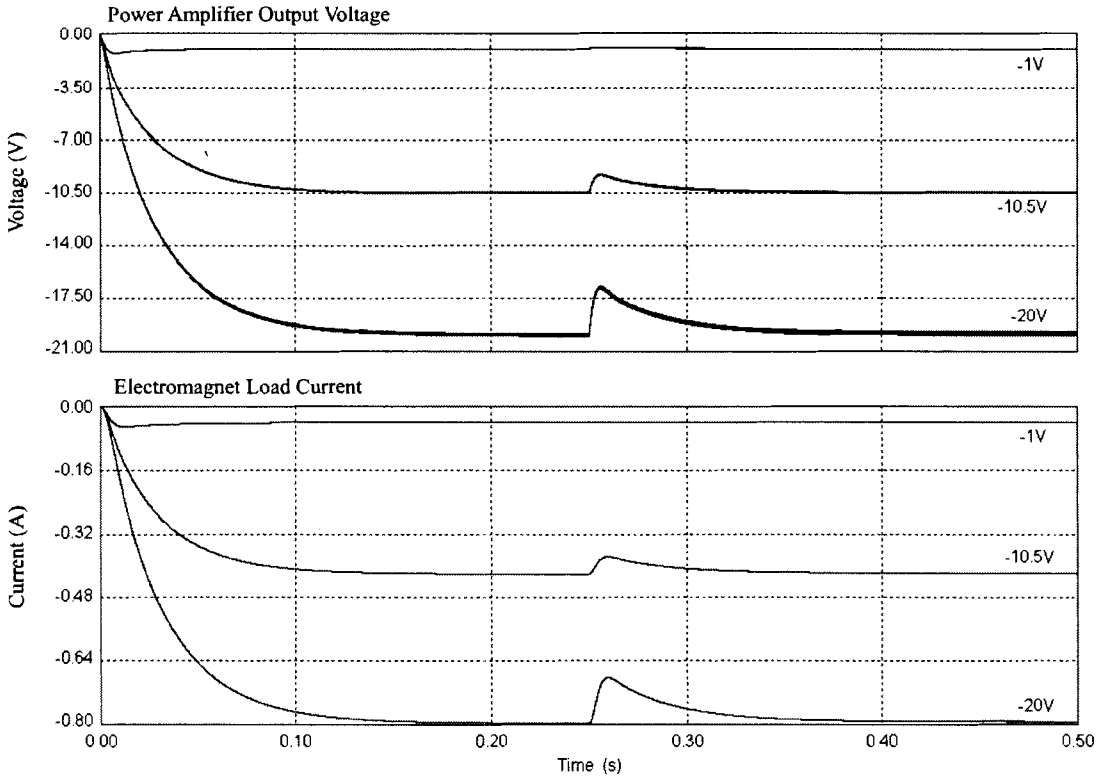

Figure 4.19: Voltage Mode Controlled 42V Buck-Boost Power Amplifier Output Voltage and Electromagnet Load Current, $\lambda = 100$

Just like its 12V counter part, the 42V voltage mode buck-boost power amplifier reacts adversely to large drops in input voltage. Significant transient disturbances are noticeable in the power amplifier output voltage and electromagnet load current when the input voltage changes from 42V to 21V at 0.25 seconds. With respect to the convergence factor, λ, the power amplifier always responds like an over-damped system.

4.5.8 42V Buck-Boost Power Amplifier with Current Sliding Mode Feedback Controller

A schematic of the 42V buck-boost power amplifier and its current sliding mode feedback controller is shown in Figure 4.20.

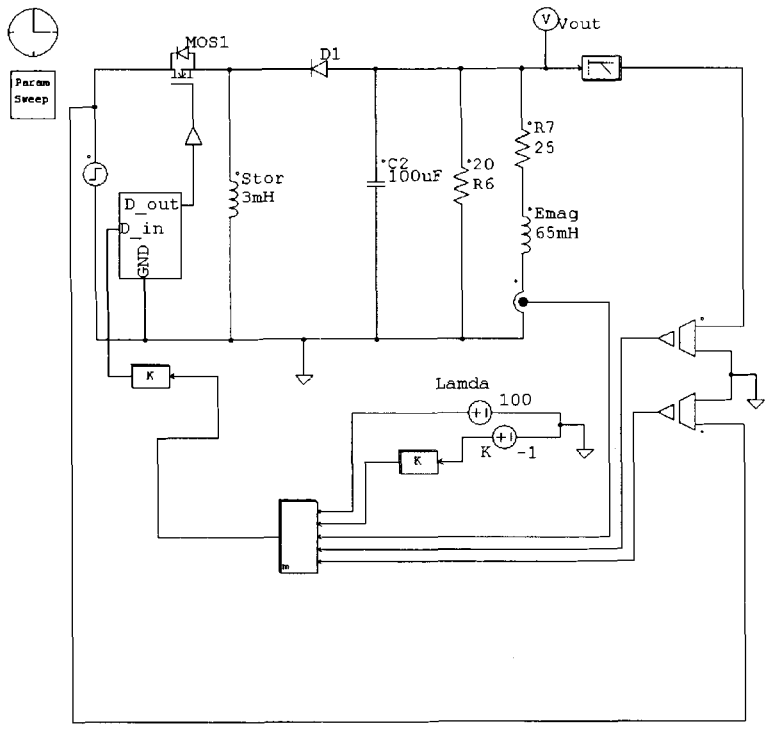

Figure 4.20: Current Mode Controlled 42V Buck-Boost Power Amplifier Schematic

The simulation parameters for this power amplifier were:

- Input voltage drop at 0.25 seconds – 42V to 21V.
- Output currents produced – -0.04A, -0.52A, and -1A.
- Convergence factor, λ, values tested – 100, and 500.

The electromagnet load current and output voltage waveforms for each simulation are shown in Figure 4.21 and Figure 4.22.

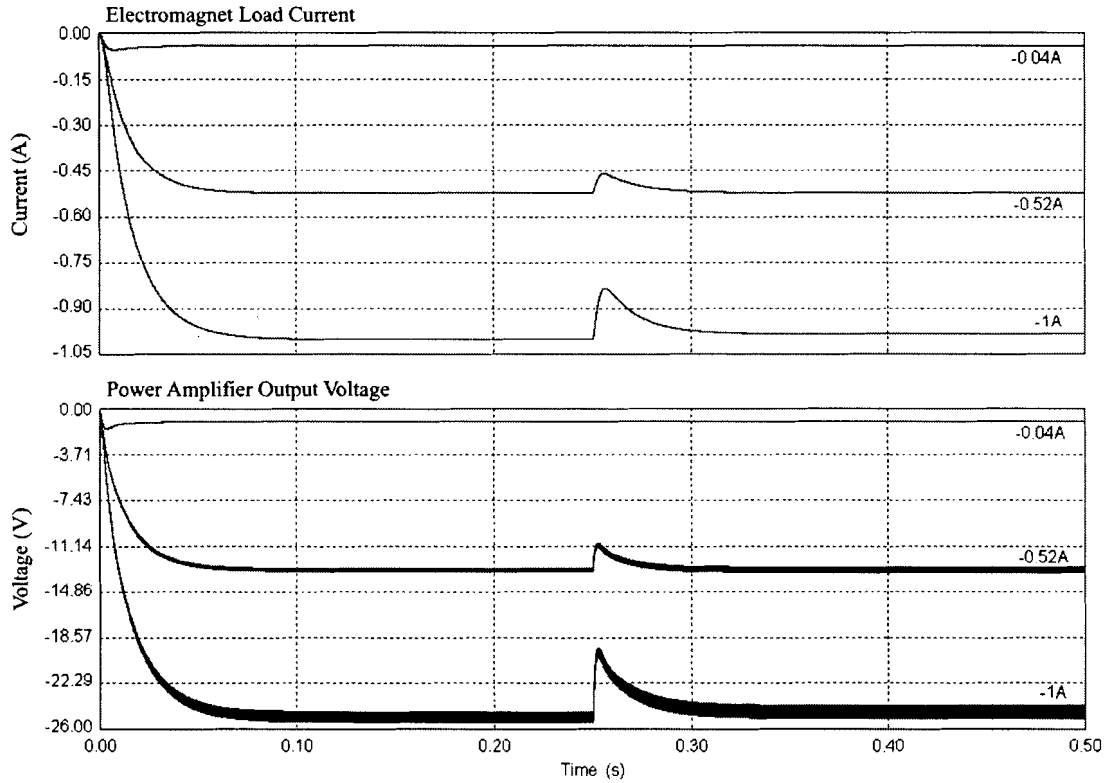

Figure 4.21: Current Mode Controlled 42V Buck-Boost Power Amplifier Electromagnet Load Current and Output Voltage, $\lambda = 100$

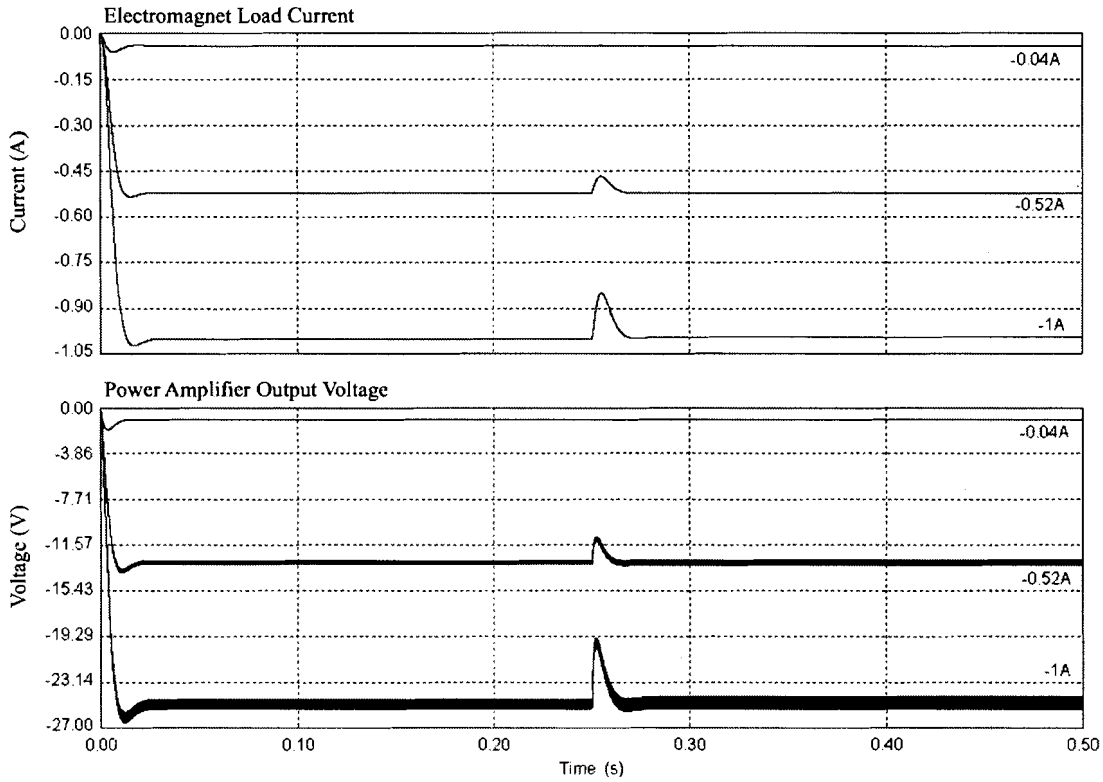

Figure 4.22: Current Mode Controlled 42V Buck-Boost Power Amplifier Electromagnet Load Current and Output Voltage, $\lambda = 500$

Just like its voltage mode counterpart, the 42V current mode buck-boost power amplifier reacts adversely to large drops in input voltage. Significant transient disturbances are noticeable in the power amplifier output voltage and electromagnet load current when the input voltage changes from 42V to 21V at 0.25 seconds. With respect to the convergence factor, λ, the power amplifier response changes from an over-damped system to an under-damped system as λ increases from 100 to 500. Therefore, increasing the λ value increases the electromagnet output voltage and load current rise times at the expense of added overshoot and a longer settling time.

4.6 Electromagnet Power Amplifier Modelling Summary and Academic Contributions

The preliminary results gathered so far from the power amplifier modelling are extremely encouraging. The buck power amplifiers are the most robust, showing no transients due to large signal input voltage disturbances, but their only caveat is that they depend on 42V battery systems that are still not prevalent in automobiles. By comparison, the buck-boost power amplifiers, the only useable power amplifiers with current 12V automobile battery systems, do show significant transients due to large signal input voltage disturbances. However, with the correct control parameters, these disturbances can be minimized. Overall, the sliding mode feedback control techniques from Mahdavi et al. proved extremely effective with respect to large signal stability of all the power amplifier models.

5 CONCLUSION

5.1 MR Material Components Future Work

The most important factor in continuing our research on MR materials relates to magnetic field generation. Because of the energy density requirements associated with the electromagnets, more research will be focussed on increasing electromagnet efficiency. Also, in the interests of energy efficiency and size it would be prudent to examine rare earth magnets as a magnetic field source. By moving the rare earth magnets closer to or farther from the MR material bushing, via a mechanical assembly, a magnetic field of varying strength could be coupled through the MR material bushing. Additionally, we will build a MRE damper and test in the same manner as the EFC damper with a pair of off-the-shelf electromagnets. In the long run, our research into MR material components will culminate in tools and techniques that can be applied towards solving the structure-borne noise problem in future automobiles.

5.2 Power Amplifier Modelling Future Work

Because of our focus on MR material bushings and components, the electromagnet power amplifier modelling work must continue in parallel as part of the MR material project. For the immediate future, it would be prudent to examine other power electronic topologies, whether from DC-DC converter literature or from motor control literature. Also, we must investigate other large signal stable feedback control techniques, as well as analyze the current sliding mode feedback control technique in-depth. Additionally, as the power amplifier modelling sub-project progresses, circuit

element non-idealities such as delay times and parasitic parameters must be included in the power amplifier models. In the long run, our research into power amplifiers will culminate in amplifiers for devices that help solve the structure-borne noise problem in future automobiles.

APPENDICES

Appendix A: EFC Damper and Test Jig Manufacturing and Assembly Process

The EFC damper fabrication process and the assembly of the EFC test jig are described in this appendix. The EFC fabrication process is explained first and followed by the EFC test jig assembly process.

EFC Damper Fabrication Process

The EFC damper fabrication process is extremely simple. The raw materials and apparatus required to make an EFC damper are listed below:

- Sylgard 184 liquid elastomer base and curing agent
- Dow Corning® 92-023 primer compound
- Elastomer mould and mounting plates/devices (elastomer is usually cast between two flat mounting plates or devices with flat metallic surfaces, such as the EM-R2 electromagnet)
- Alfa Aesar Stock # 00170 spherical iron powder
- Duct tape and/or black electrical tape
- Acetone
- Sand paper
- Glass crucible
- Glass stirring rod
- Mass Scale

- Vacuum chamber and pump
- Lab oven

The EFC damper manufacturing steps are as follows:

1. The EFC damper fabrication process starts with sanding down the EFC damper mounting plates/surfaces and cleaning out excessive dirt with acetone. The sanding and acetone wipe cleans out the mounting plate/surface so that the primer can provide a strong solid bond between the EFC damper and the mounting plates/surfaces.
2. A uniform coat of Dow Corning® 92-023 primer compound is applied to the EFC damper mounting plates/surfaces. The mounting plates/surfaces are then left to dry under a fume hood for 45 to 60 minutes. The primer compound bonds the EFC damper to the mounting plates/surfaces during the EFC damper curing process.
3. A 10:1 mass ratio of the Sylgard 184 liquid elastomer base and curing agent is poured into the glass crucible. The liquid elastomer base and curing agent is mixed well by hand with the glass stirring rod for at least 5 minutes until it takes on a uniform appearance.
4. The desired amount of Alfa Aesar Stock # 00170 spherical iron powder is then poured into the liquid elastomer and mixed well by hand with the glass stirring rod for at least 5 minutes.
5. The crucible of liquid EFC mixture is placed in a vacuum chamber and pumped down for 20 minutes to remove air bubbles.

6. After removal from the vacuum chamber, the EFC mixture is poured into the EFC damper mould, which has been pre-assembled and placed on one of the two mounting plates/surfaces inside a lab oven. The second mounting plate/surface is placed on top of the mould and EFC mixture. A mass is placed on top of the second mounting plate/surface to properly seal the EFC mixture into the mould.
7. Finally, the lab oven is set to 85°C and the EFC mixture is left to cure and bond to the two mounting plates/surfaces for at least 90 minutes.
8. After curing, the EFC damper assembly is removed from the oven and allowed to cool. After cooling and mould removal, the EFC damper assembly is ready for use.

The EFC damper manufacturing process was established with the first test damper we built using 33.98 grams of elastomer base, 3.4 grams of elastomer curing agent, and 84.34 grams of iron powder. We used scrap steel and aluminium plates to mount the EFC damper and we made our EFC damper mould from a 1.5" plastic pipefitting. The mounting plates and 1.5" plastic pipefitting are illustrated in Figure A 1 and Figure A 2, respectively.

The test damper mould, illustrated in Figure A 3, was made from the pipefitting in Figure A 2 and was subsequently cut with a hacksaw and machined down on a lathe to a 5.5cm diameter tube with a 1.6cm length. We then sawed this tube down the middle into two semi-circular pieces so that the mould could be removed after the EFC test damper had been fabricated. For fabrication, the mould was assembled by taping the two semi-circular pieces together with black electrical tape.

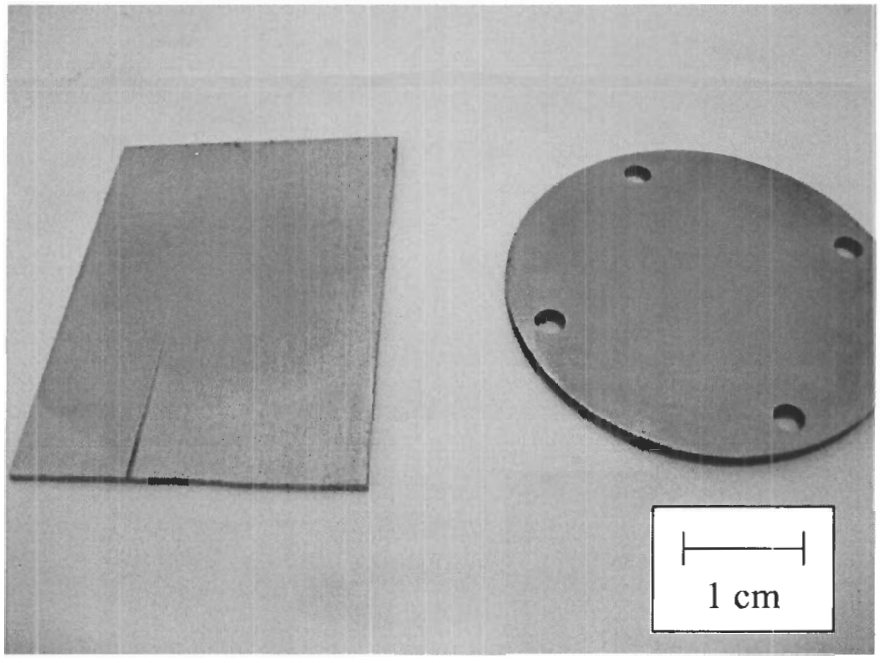

Figure A 1: Primer Coated EFC Test Damper Mounting Plates

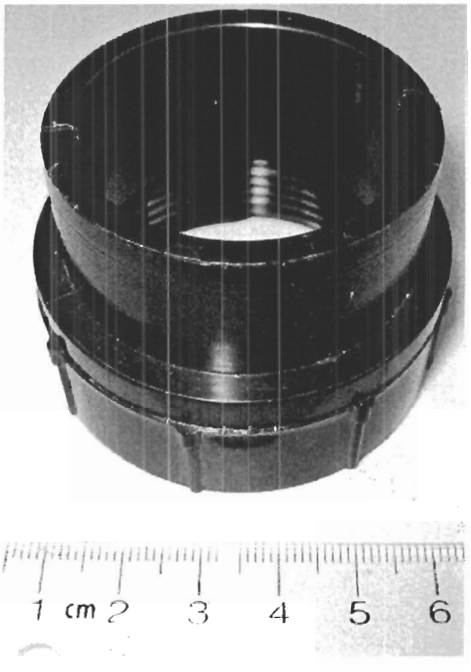

Figure A 2: 1.5" Plastic Pipefitting

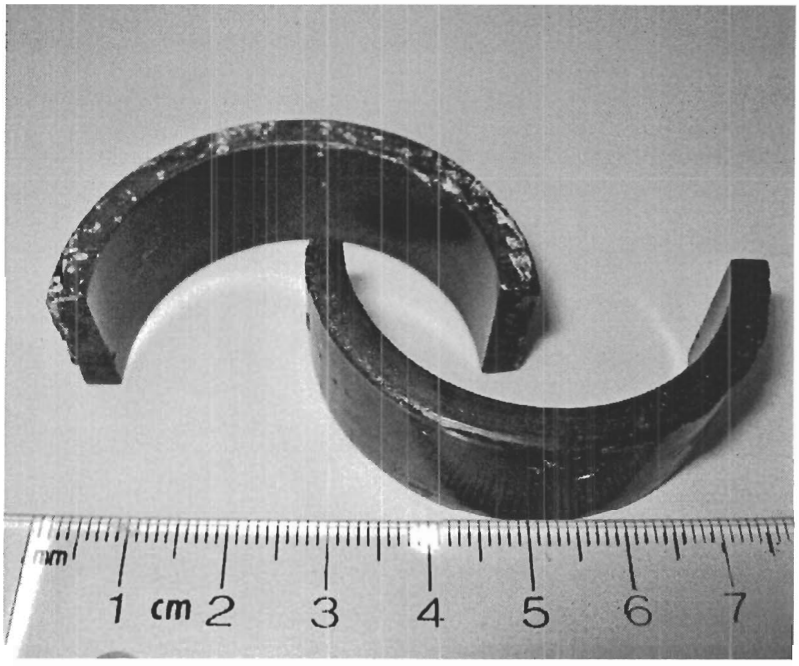

Figure A 3: EFC Test Damper Mould

The vacuum chamber for removing air bubbles from the EFC test damper mixture comprised a tupperware box lined with teflon tape along the lid seal and a 0.5" pipefitting glued to a hole in the tupperware lid. A pipe from the Welch vacuum pump was taped into the vacuum chamber pipefitting and the entire vacuum chamber was secured to a table with duct tape as shown in Figure A 4.

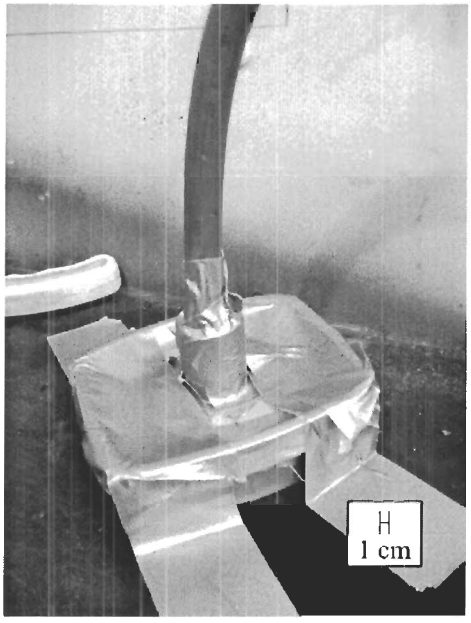

Figure A 4: EFC Test Damper Mixture in the Vacuum Chamber

The EFC damper was then cured in a Fisher Scientific lab oven for approximately 90 minutes. The cured EFC test damper assembly is illustrated in Figure A 5.

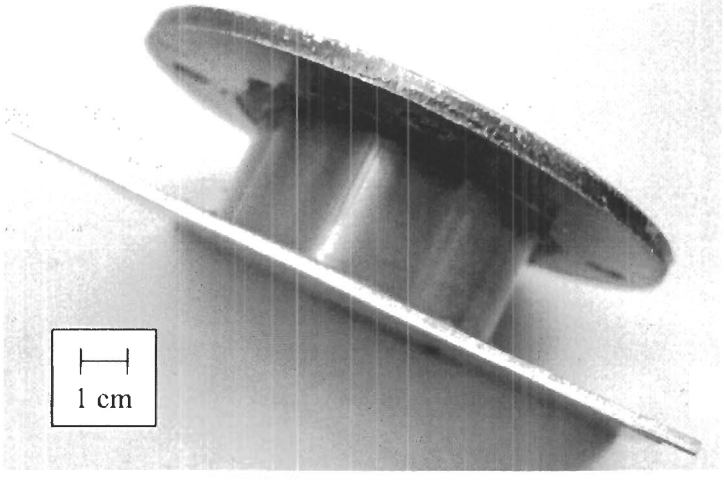

Figure A 5: Completed EFC Damper Assembly

The bond between the EFC test damper and the mounting plates was so strong that a tabletop vice was required to separate the EFC test damper from the mounting plates. The EFC test damper was then cut into three separate pieces, as illustrated in

Figure A 6, to examine the EFC material uniformity. The even distribution of iron powder in the test damper, as well as the lack of settling due to gravity proved to be satisfactory to proceed with the EFC damper test jig construction.

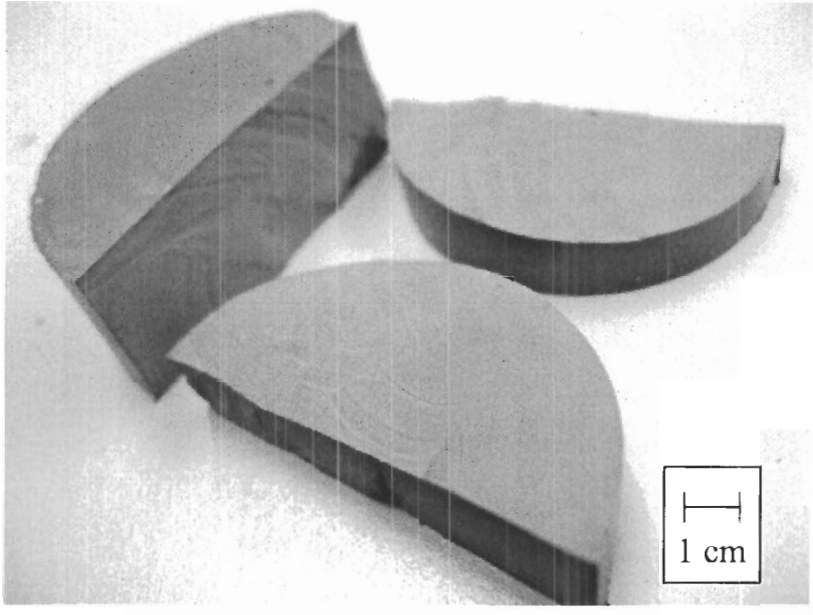

Figure A 6: Eviscerated EFC Test Damper

The damper mould for the EFC damper test jig was also machined from a 1.5" plastic pipefitting down to a 4cm diameter, 0.69cm thick mould which determined the final EFC damper dimensions as described in Chapter 2. Both the electromagnets were sanded, cleaned with acetone, coated with primer and then left under a fume hood for 94 minutes. The EFC mixture was comprised of 13.11 grams of elastomer base, 1.33 grams of elastomer curing agent, and 19.24 grams of iron powder. The iron powder mass was calculated such that the EFC mixture would be 30% iron powder by volume to maximize the magnetorheological effect in the EFC damper [23]. After it was mixed, the EFC mixture was placed in the vacuum chamber for 51 minutes. The EFC damper and electromagnet assembly was initially cured at approximately 82°C for 71 minutes in the

Fischer Scientific lab oven. Because of excessive liquid elastomer mixture seepage from around the damper mould area after removal from the lab oven, the assembly was placed back in the lab oven and cured for another 57 minutes at approximately 84°C. The left side and right side images of Figure A 7 show the completely cured EFC damper and electromagnet assembly before and after the removal of the EFC damper mould and subsequent cleanup, respectively.

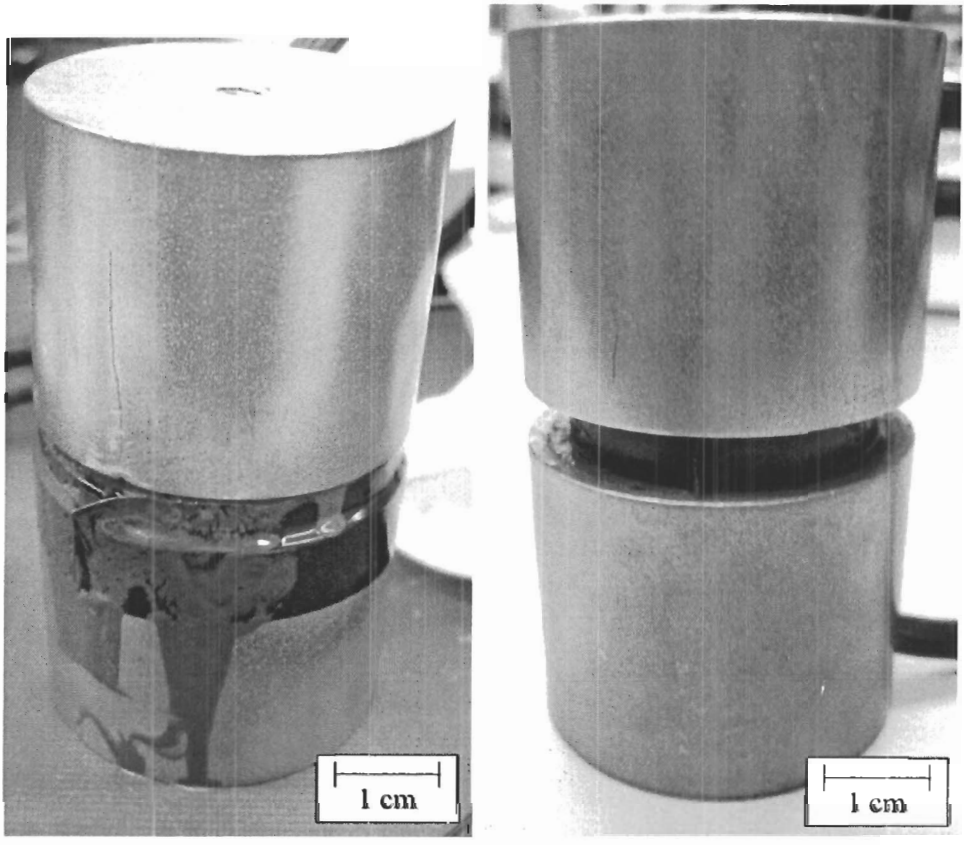

A B

Figure A 7: Post-curing EFC Damper and Electromagnet Assembly, Pre (A) and Post (B) Mould Removal

EFC Test Jig Assembly Process

After cleanup the EFC damper and electromagnet assembly was secured to a mounting plate to form the EFC damper test jig. A diagram of the test jig is shown in Figure A 8.

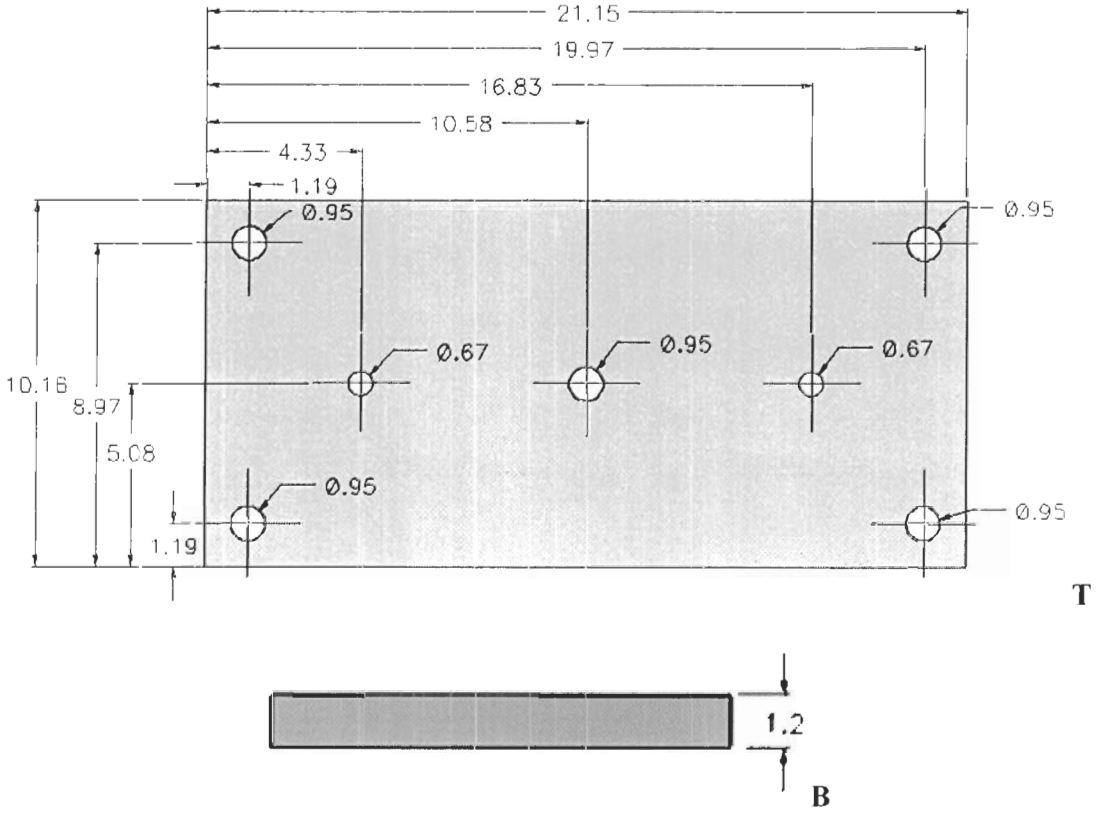

Figure A 8: EFC Damper Test Jig Mounting Plate Top (T) and Front (B) Views with Dimensions in Centimetres

The cured EFC damper and electromagnet assembly was secured to the mounting plate with a 3/8" long, 1/4-20 phillips pan head screw through one of the two 0.67cm diameter holes in the mounting plate. A three dimensional rendering of the completed test jig is shown in Figure A 9.

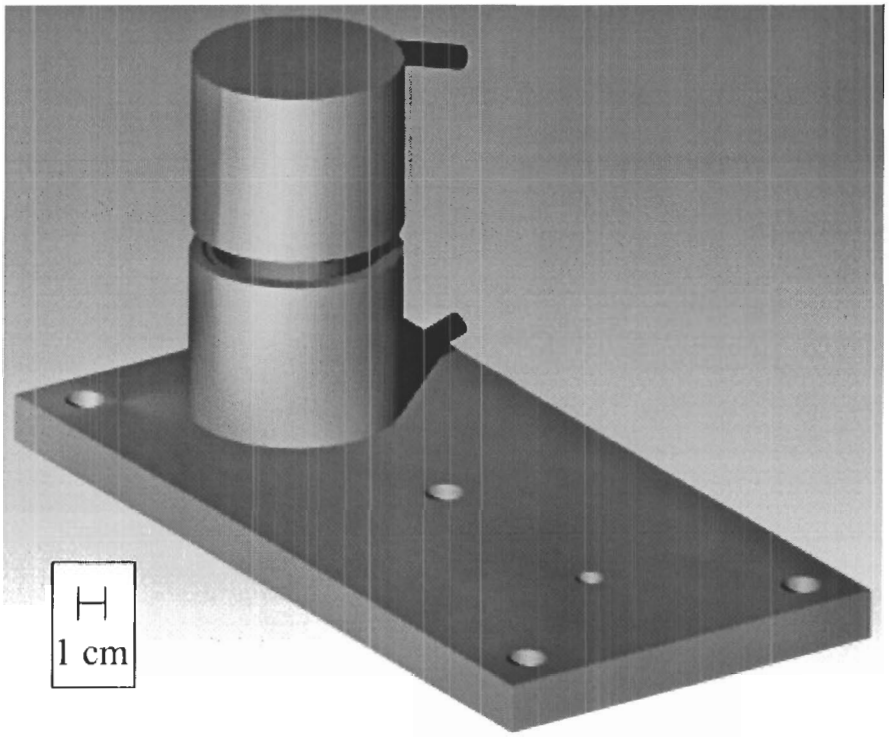

Figure A 9: EFC Damper Test Jig Illustration

The EFC damper test jig was secured to the shaker table we used for our experiments with five 3/8-16 bolts through the five 0.95cm diameter holes in the mounting plate. The five 0.95cm diameter holes in the mounting plate were drilled to align with 3/8-16 threaded, 5/8" deep mounting holes on the shaker table.

Appendix B: EM-R2 Electromagnet Field Strength Measurement

The magnetic field strength of both EM-R2 electromagnets was characterized using the equipment summarized in Table B 1.

Table B 1: Electromagnet Field Strength Measurement Equipment

Device	Vendor	Model Number
Digital Tesla Metre	Group 3	DTM-133
DC Power Supply	Circuit Test	PSB 3030
DMM	Fluke	Series 75

The magnetic field strength of each electromagnet was measured by placing the tesla metre probe 1mm above the centre of the electromagnet pole, as shown in Figure B 1, and then powering up the electromagnet with the DC power supply. Magnetic field strength readings were taken for electromagnet terminal voltages varying from 0V to 16V in 0.5V increments.

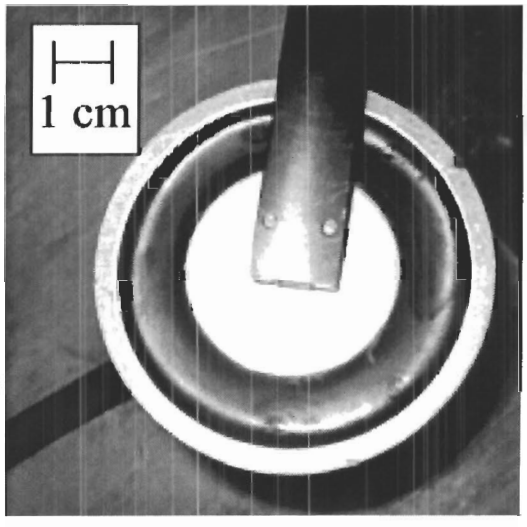

Figure B 1: Tesla Metre Probe Setup for EM-R2 Electromagnet Field Strength Measurement

The measured magnetic field strength data for the EFC damper test jig top and bottom electromagnets are shown in Table B 2 and Table B 3, respectively.

Table B 2: Top Electromagnet (Electromagnet 1) Field Strength Data

Voltage (V)	Measured Voltage (V)	Measured Current (A)	Magnetic Field Strength (T)
0	0	0	0.001
0.5	0.474	0.01	0.00205
1	0.973	0.03	0.0032
1.5	1.474	0.04	0.00445
2	1.972	0.06	0.0056
2.5	2.477	0.08	0.00685
3	2.975	0.1	0.00805
3.5	3.47	0.12	0.0093
4	3.97	0.14	0.01055
4.5	4.47	0.16	0.0118
5	4.97	0.18	0.013
5.5	5.47	0.2	0.01435
6	5.97	0.22	0.01555
6.5	6.47	0.24	0.0168
7	6.97	0.26	0.01805
7.5	7.47	0.27	0.0193
8	7.97	0.29	0.0206
8.5	8.47	0.31	0.02185
9	8.96	0.33	0.02305
9.5	9.46	0.35	0.0243
10	9.96	0.36	0.02555
10.5	10.46	0.38	0.0268
11	10.96	0.4	0.0281
11.5	11.46	0.42	0.02925
12	11.96	0.43	0.0305
12.5	12.46	0.45	0.03165
13	12.95	0.47	0.0328
13.5	13.45	0.49	0.03405
14	13.95	0.5	0.03525
14.5	14.45	0.52	0.0364
15	14.95	0.54	0.0376
15.5	15.45	0.55	0.03875
16	15.95	0.57	0.0398

Table B 3: Bottom Electromagnet (Electromagnet 2) Field Strength Data

Voltage (V)	Measured Voltage (V)	Measured Current (A)	Magnetic Field Strength (T)
0	0	0	0.0004
0.5	0.474	0.01	0.0015
1	0.973	0.03	0.0027
1.5	1.474	0.05	0.00395
2	1.972	0.06	0.0052
2.5	2.477	0.08	0.0064
3	2.975	0.1	0.00775
3.5	3.47	0.12	0.00905
4	3.97	0.14	0.0104
4.5	4.47	0.17	0.0118
5	4.97	0.18	0.0131
5.5	5.47	0.2	0.0144
6	5.97	0.22	0.01575
6.5	6.47	0.24	0.01705
7	6.97	0.26	0.01835
7.5	7.47	0.28	0.0196
8	7.97	0.3	0.02095
8.5	8.47	0.32	0.02225
9	8.96	0.34	0.02355
9.5	9.46	0.36	0.0249
10	9.96	0.37	0.0263
10.5	10.46	0.39	0.0276
11	10.96	0.41	0.0291
11.5	11.46	0.43	0.0304
12	11.96	0.45	0.03175
12.5	12.46	0.47	0.03295
13	12.95	0.49	0.0341
13.5	13.45	0.5	0.03535
14	13.95	0.52	0.0366
14.5	14.45	0.54	0.03775
15	14.95	0.55	0.0388
15.5	15.45	0.57	0.04005
16	15.95	0.59	0.0411

Data plots of magnetic field strength vs. measured electromagnet terminal voltage for both the top and bottom electromagnets are shown in Figure B 2 and Figure B 3, respectively.

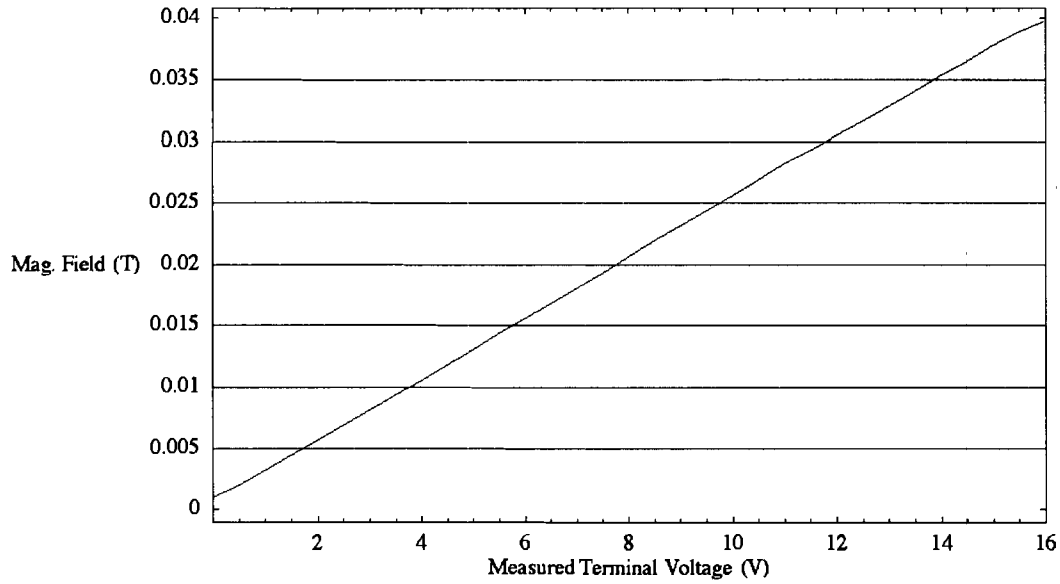

Figure B 2: Top Electromagnet Field Strength Data Plot

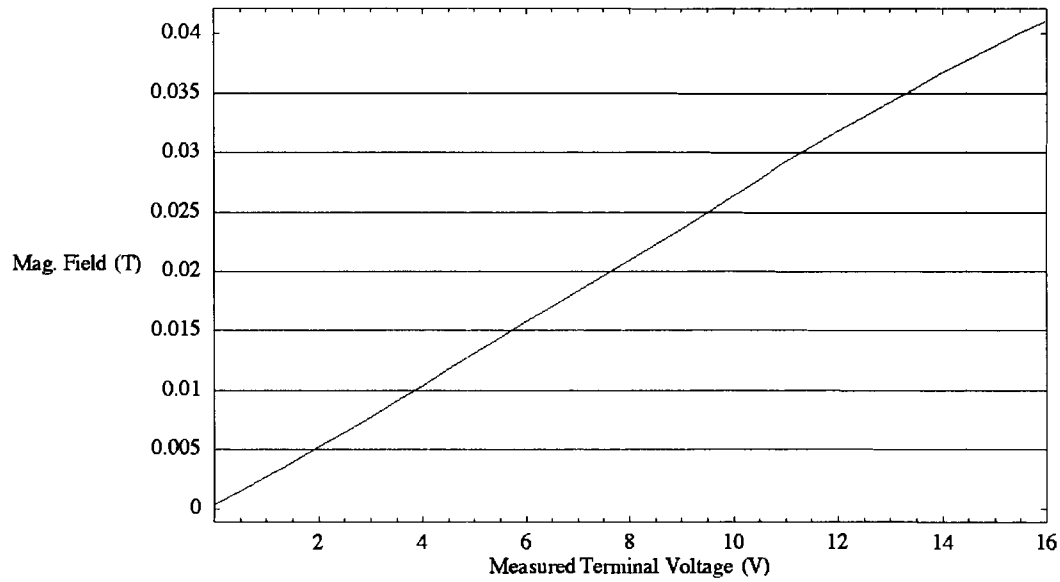

Figure B 3: Bottom Electromagnet Field Strength Data Plot

Appendix C: EFC Damper Strain Measurement

Recall from chapters 2 and 3 that in the presence of a magnetic field, an EFC damper will dilate. The EFC damper dilation was verified by measuring the circumferential strain of the EFC damper with a strain gauge connected to a strain gauge amplifier. The equipment used to measure the EFC damper circumferential strain is listed in Table C 1.

Table C 1: EFC Circumferential Strain Measurement Equipment

Device	Vendor	Model Number
Strain Gauge	Vishay	CEA-06-240UZ-120
Strain Gauge Amplifier	Vishay	Series 2100
DC Power Supply	Circuit Test	PSB 3030
DMM	Fluke	Series 75

The EFC damper circumferential strain measurement process steps were as follows:

1. After soldering wires to the strain gauge terminals, the strain gauge was mounted on the sidewall of the EFC Damper, as shown in Figure C 1, the strain gauge was mounted on the EFC damper with double sided tape and covered over with scotch tape.

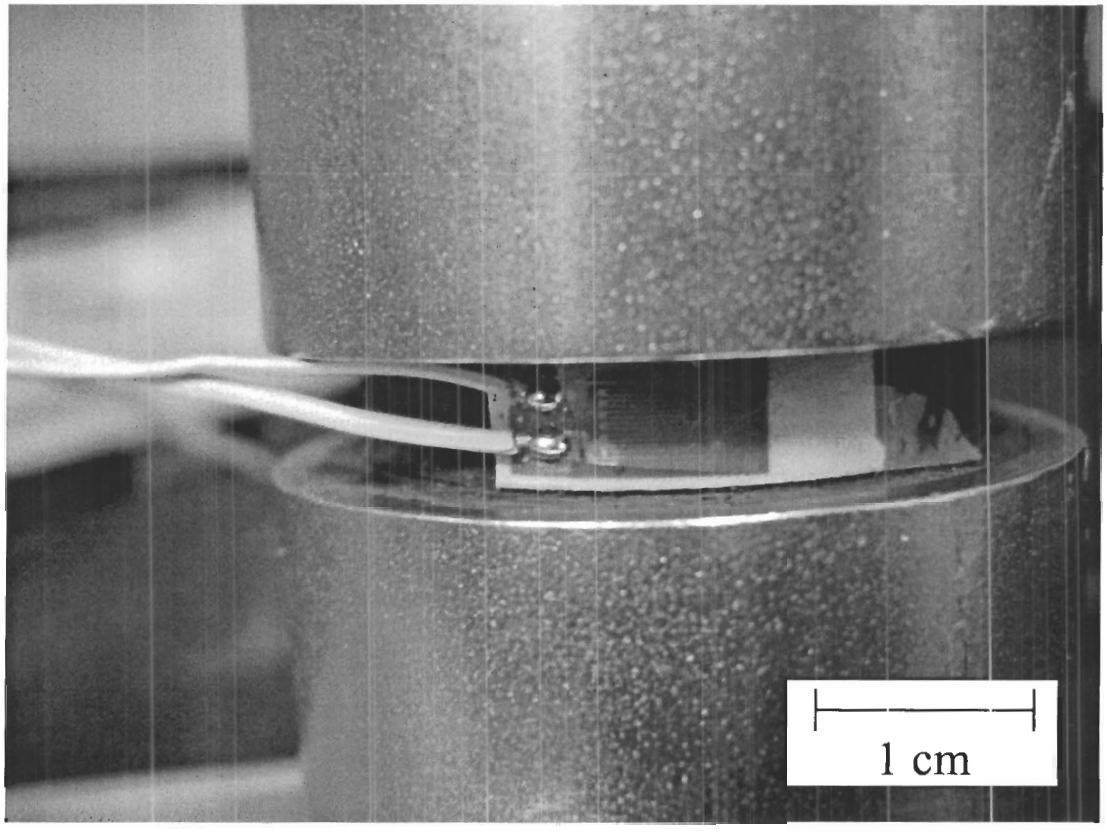

Figure C 1: Vishay Strain Gauge on EFC Damper

2. The strain gauge leads were attached to the Vishay strain gauge amplifier shown in Figure C 2. The strain gauge amplifier has an internal wheatstone bridge where the the strain gauge is attached to this bridge in a quarter bridge configuration as illustrated in Figure C 3. The strain gauge changes resistance as it experiences strain, which then changes the wheatstone balance voltage, Vout. The change in Vout can be used to determine the strain gauge resistance change and the corresponding strain experienced by the strain gauge. As shown in Figure C 2, the strain gauge amplifier internal wheatstone bridge excitation voltage was set to 2V and measured at 2.006V on the Fluke DMM.

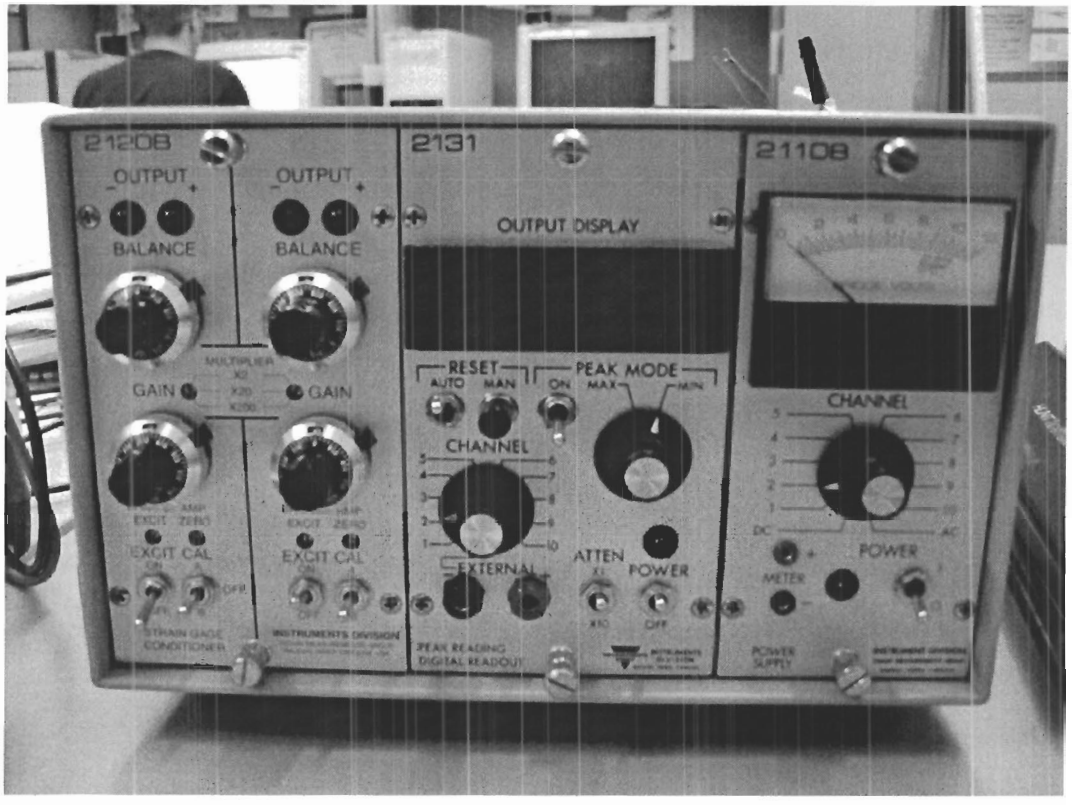

Figure C 2: Vishay Series 2100 Strain Gauge Amplifier

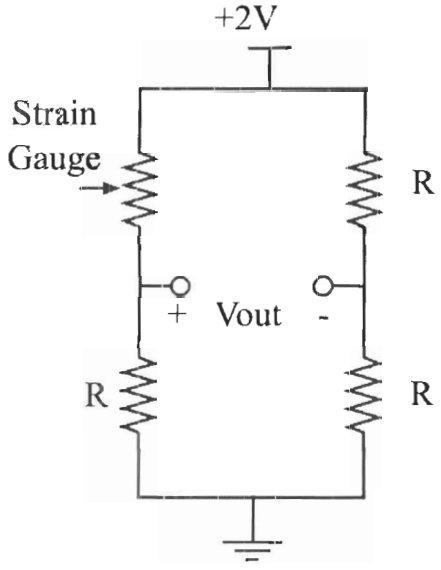

Figure C 3: Strain Gauge in Quarter Configuration Wheatstone Bridge

3. Vout is amplified with a gain of 2000 and then displayed.

4. After setting the wheatstone bridge excitation voltage and output gain, the strain gauge amplifier was balanced and calibrated to produce a null reading when zero power was applied to the EFC damper test jig electromagnets.

5. The electromagnets of the EFC damper test jig were connected to the DC power supply, which was set to16V. The resulting change in the strain gauge amplifier output was recorded over five trials.

The strain gauge amplifier gave a consistent output of +2V for all five trials. The strain gauge resistance was measured on the Fluke DMM and found to be 120.7Ω. Therefore, with the applied magnetic field, the new strain gauge resistance was calculated to be 120.5Ω, indicating that the strain gauge had experienced a tensile strain on the EFC damper side wall due to EFC damper dilation in the presence of a magnetic field. The exact strain, ϵ, can be calculated from

$$\epsilon = \frac{\Delta R}{S_s R} \quad [57] \qquad \textbf{Equation C 1}$$

where, R is the unstrained strain gauge resistance, ΔR is the change in strain gauge resistance due to strain, and S_s is the gauge factor of the strain gauge. The Vishay strain gauge has a gauge factor of 2.08 [58]. Using Equation C 1, the dilated EFC damper circumferential strain was calculated to be -796.6μstrain.

Appendix D: Complete EFC Damper Experimental Data and Mathematical Models

All the EFC damper experimental dataset plots and all mathematical model instances are presented in this appendix. The dataset plots comprise the vibration data for the shaker table, the EFC damper test jig mounting plate, and the EFC damper test jig top electromagnet for all frequency sweeps. For a given frequency sweep, a mathematical model instance comprises the relevant parameters or equations pertaining to the fitted function, a composite plot of the transmissibility data and the fitted function, as well as absolute and percentage error plots between the transmissibility data and the fitted function.

Data Plots

The dataset plots are shown first and are followed by all instances of the second order mathematical model, all instances of the linear viscoelastic model, and all instances of the quadratic viscoelastic model.

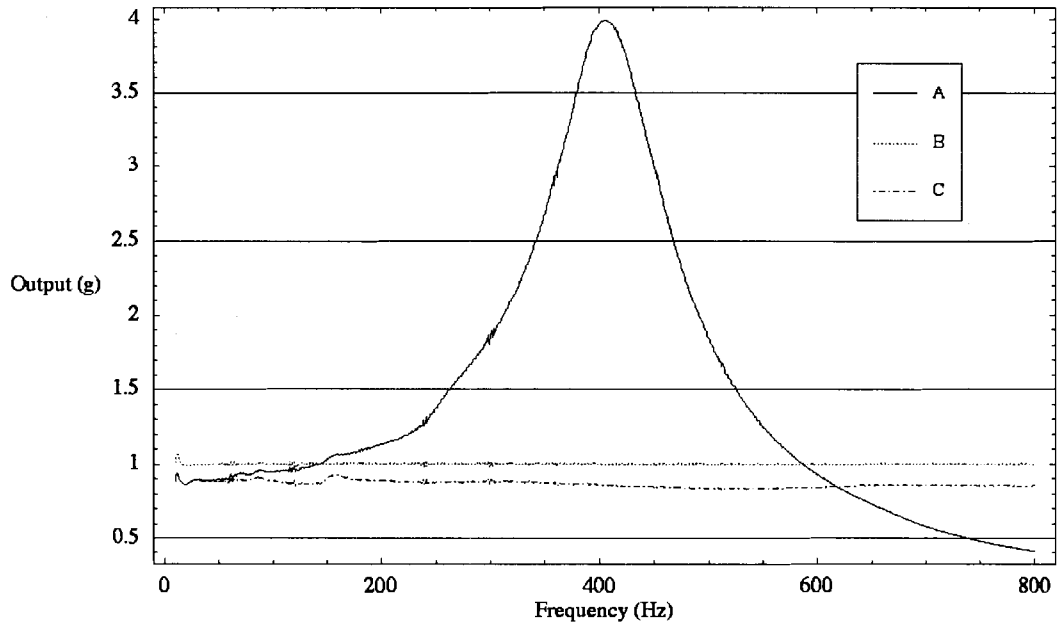

Figure D 1: 0V Sweep Measured Vibration Output, A – Top Electromagnet, B – Shaker Table, C – EFC Test Jig Base Plate

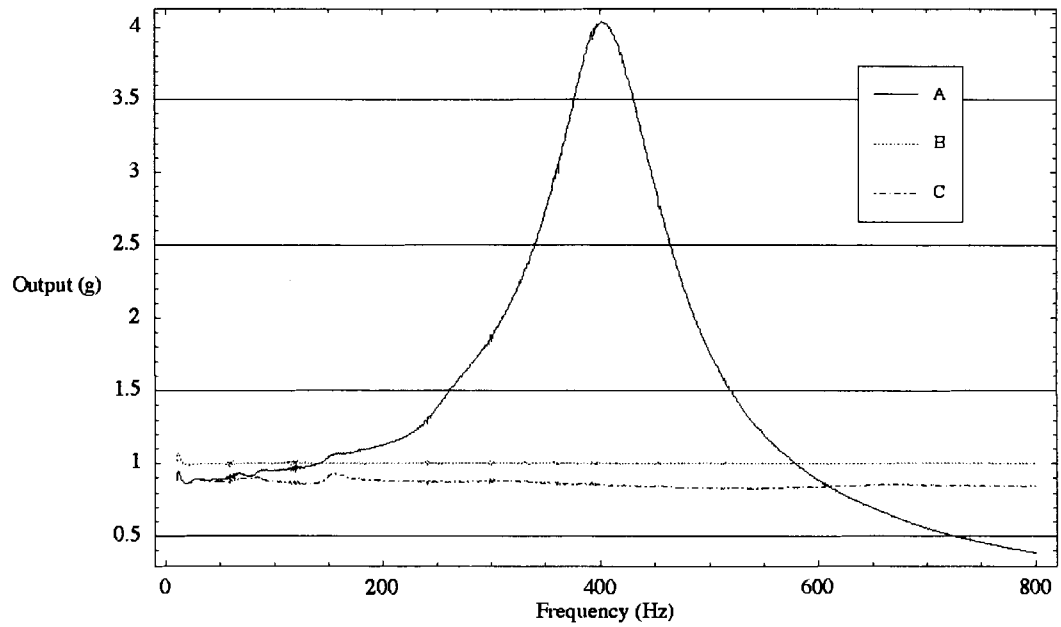

Figure D 2: 2V Sweep Measured Vibration Output, A – Top Electromagnet, B – Shaker Table, C – EFC Test Jig Base Plate

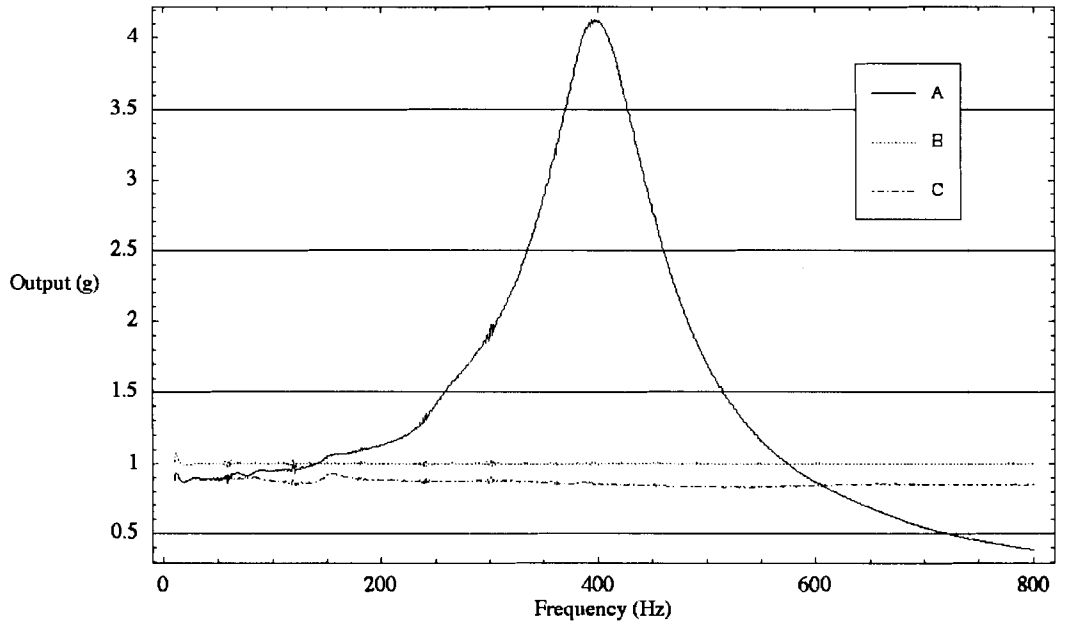

Figure D 3: 4V Sweep Measured Vibration Output, A – Top Electromagnet, B – Shaker Table, C – EFC Test Jig Base Plate

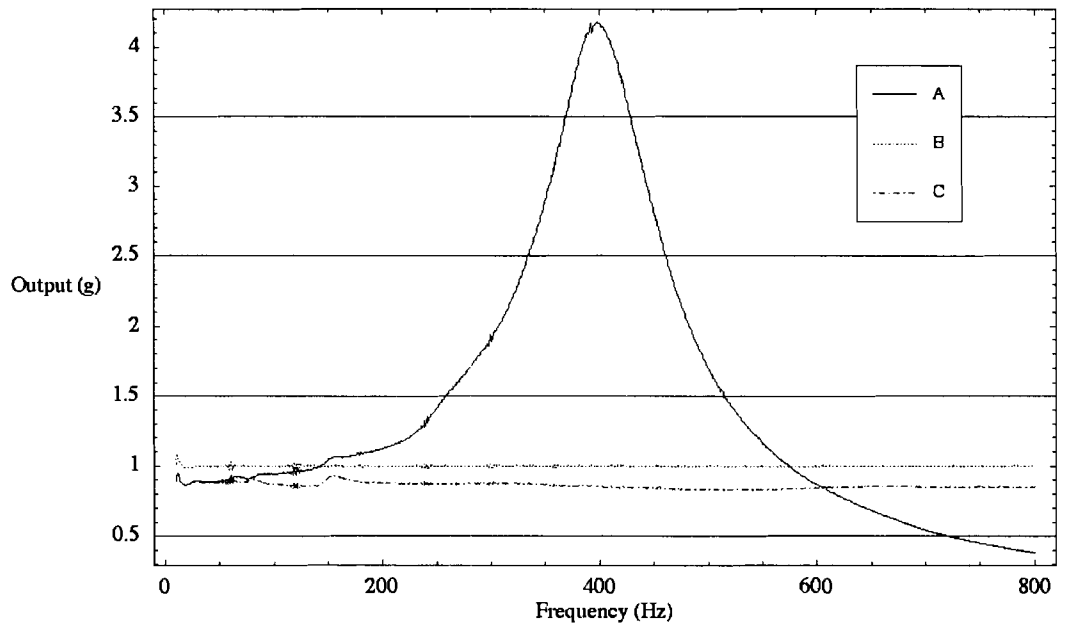

Figure D 4: 6V Sweep Measured Vibration Output, A – Top Electromagnet, B – Shaker Table, C – EFC Test Jig Base Plate

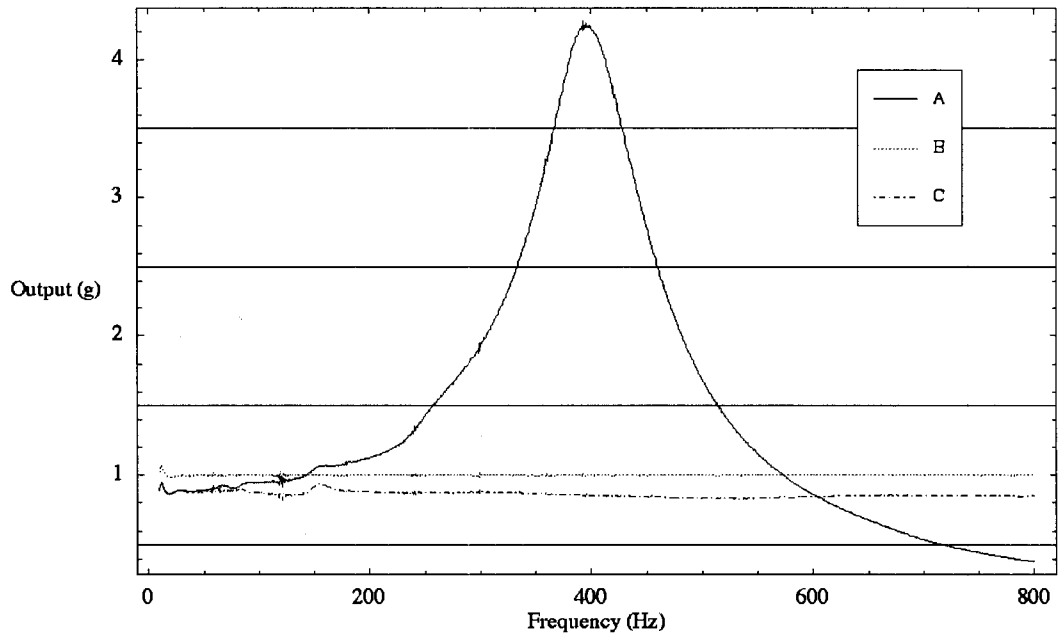

Figure D5: 8V Sweep Measured Vibration Output, A – Top Electromagnet, B – Shaker Table, C – EFC Test Jig Base Plate

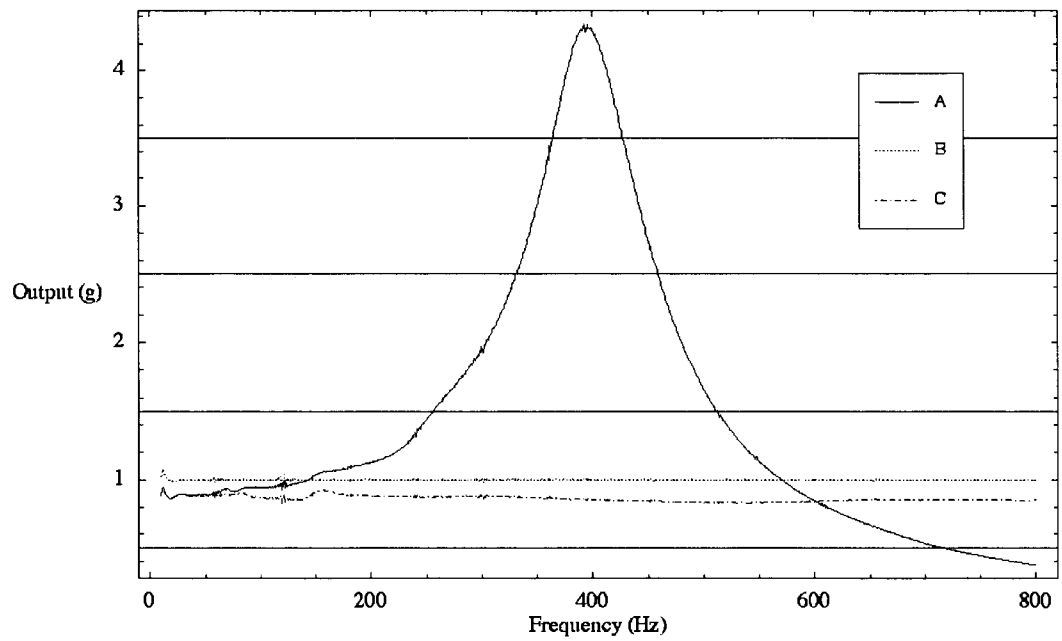

Figure D 6: 10V Sweep Measured Vibration Output, A – Top Electromagnet, B – Shaker Table, C – EFC Test Jig Base Plate

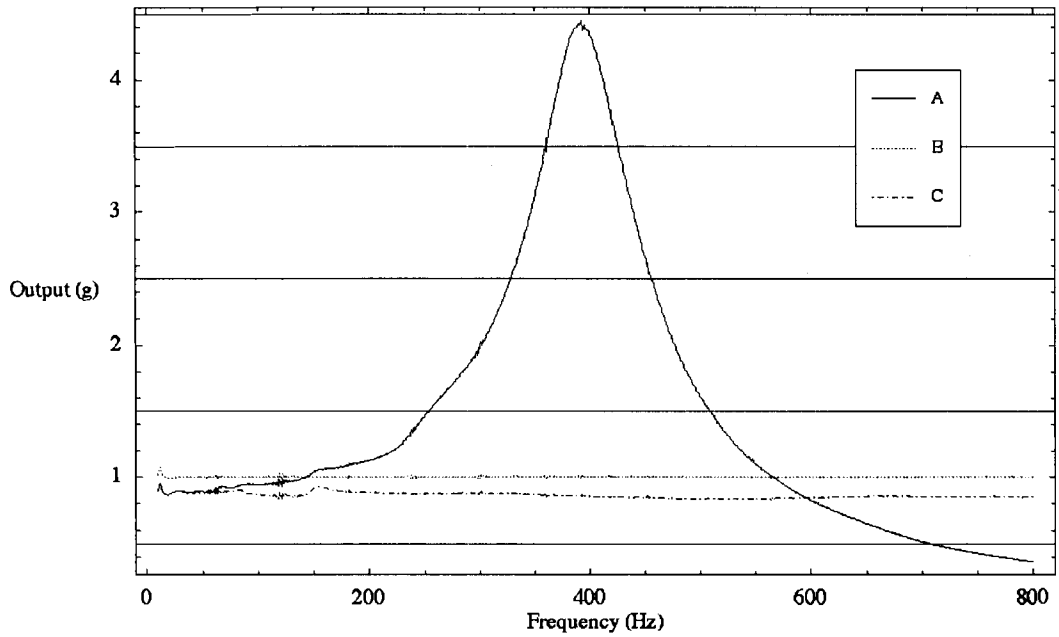

Figure D 7: 12V Sweep Measured Vibration Output, A – Top Electromagnet, B – Shaker Table, C – EFC Test Jig Base Plate

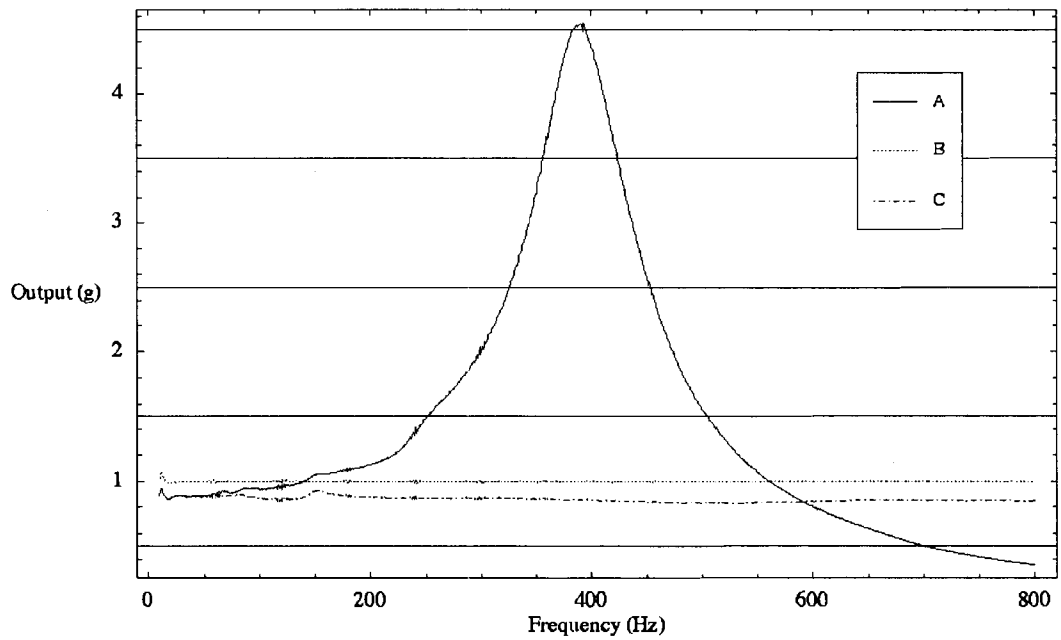

Figure D 8: 14V Sweep Measured Vibration Output, A – Top Electromagnet, B – Shaker Table, C – EFC Test Jig Base Plate

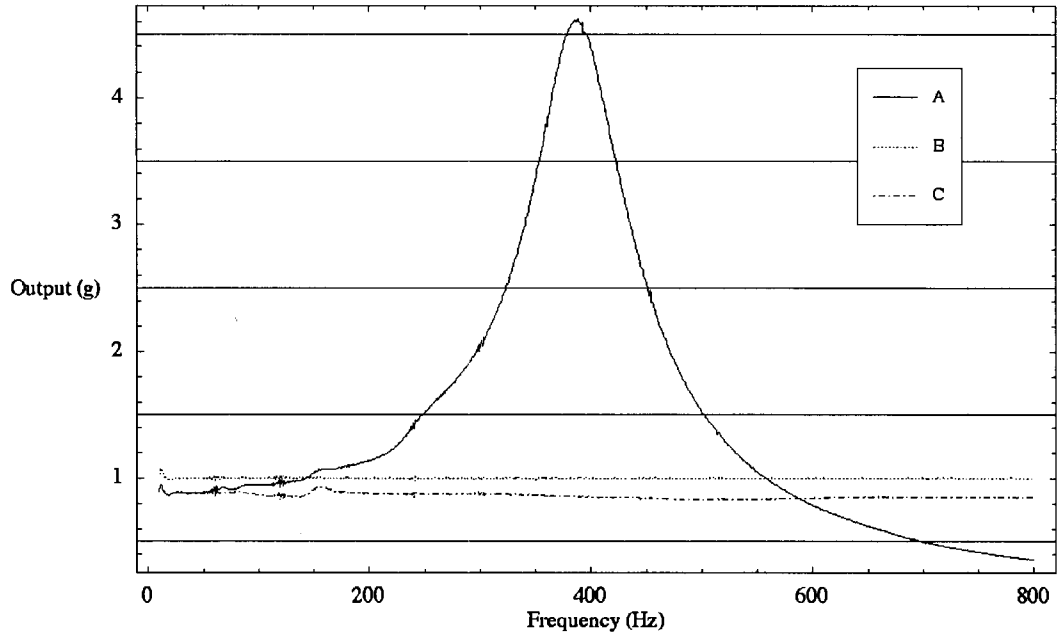

Figure D 9: 16V Sweep Measured Vibration Output, A – Top Electromagnet, B – Shaker Table, C – EFC Test Jig Base Plate

Mass Spring Damper Mathematical Model

Recall that the first mathematical model fit to the derived transmissibility data was the magnitude function for the second order mass spring damper model,

$$\left| \frac{C\,j\omega + k}{M\,j\omega^2 + C\,j\omega + k} \right|, \qquad \textbf{Equation D 1}$$

where, k is the spring constant in N/m, and C is the damping constant in N•sec/m. Both constants are shown in Table D 1 for the transmissibility datasets for all frequency sweeps.

Table D 1: Returned Spring and Damper Constants for Mass Spring Damper Mathematical Model Fit

Electromagnet Voltage (V)	k (N/m)	C (N•sec/m)
0	3.754×10^6	311.2
2	3.682×10^6	304.8
4	3.603×10^6	294.7
6	3.601×10^6	290.2
8	3.567×10^6	283.9
10	3.534×10^6	277.8
12	3.480×10^6	269.4
14	3.419×10^6	260.4
16	3.380×10^6	253.9

The plots corresponding to the mass spring damper model fit for each derived transmissibility dataset comprise a composite dataset and fitted mass spring damper model function plot, and a percentage error plot. Percentage error is given by

$$100 * \left| \frac{f - d}{d} \right|, \qquad \textbf{Equation D 2}$$

where, f is the second order magnitude function value, and d is the transmissibility dataset value for a given frequency.

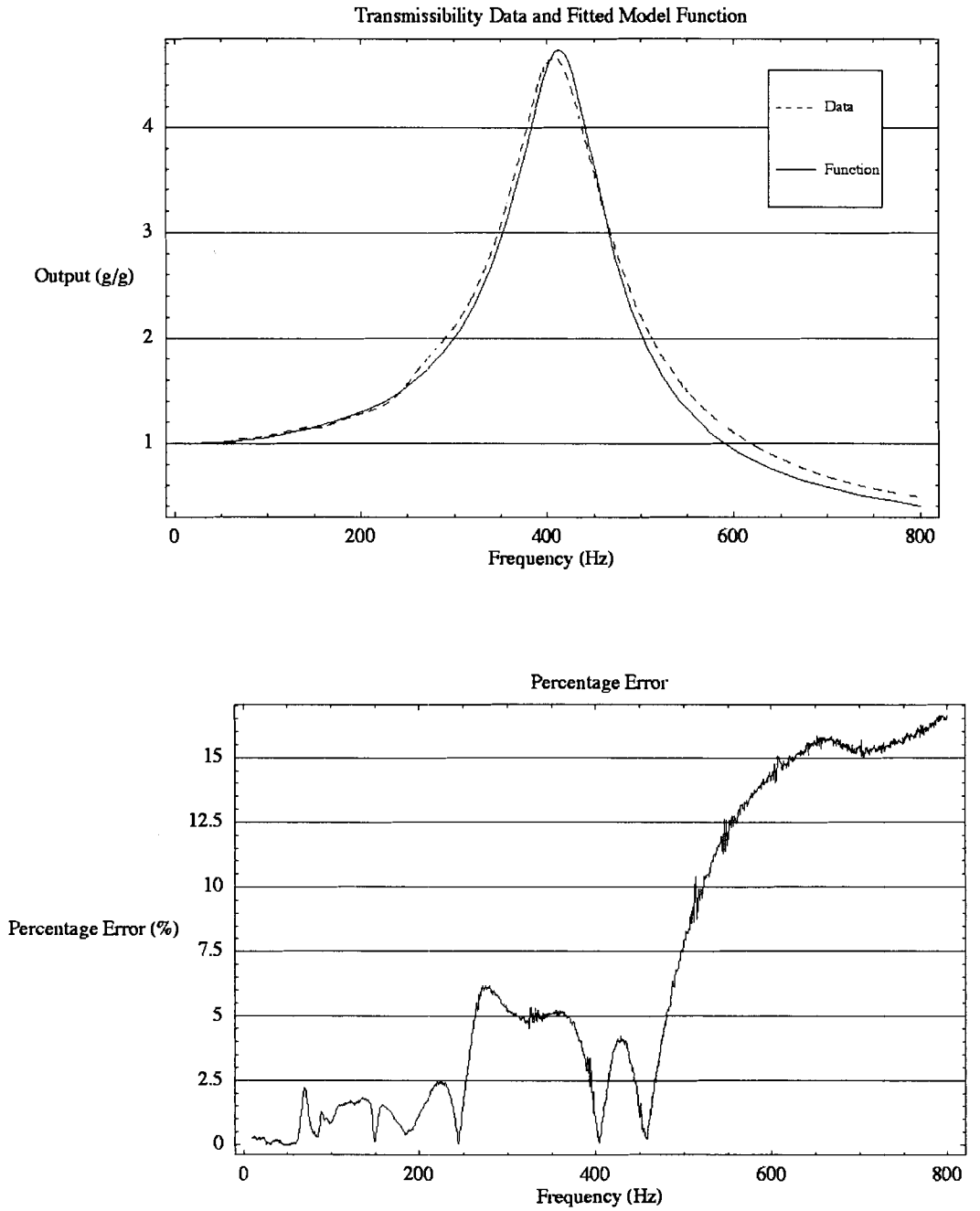

Figure D 10: 0V Sweep Mass Spring Damper Model Plots

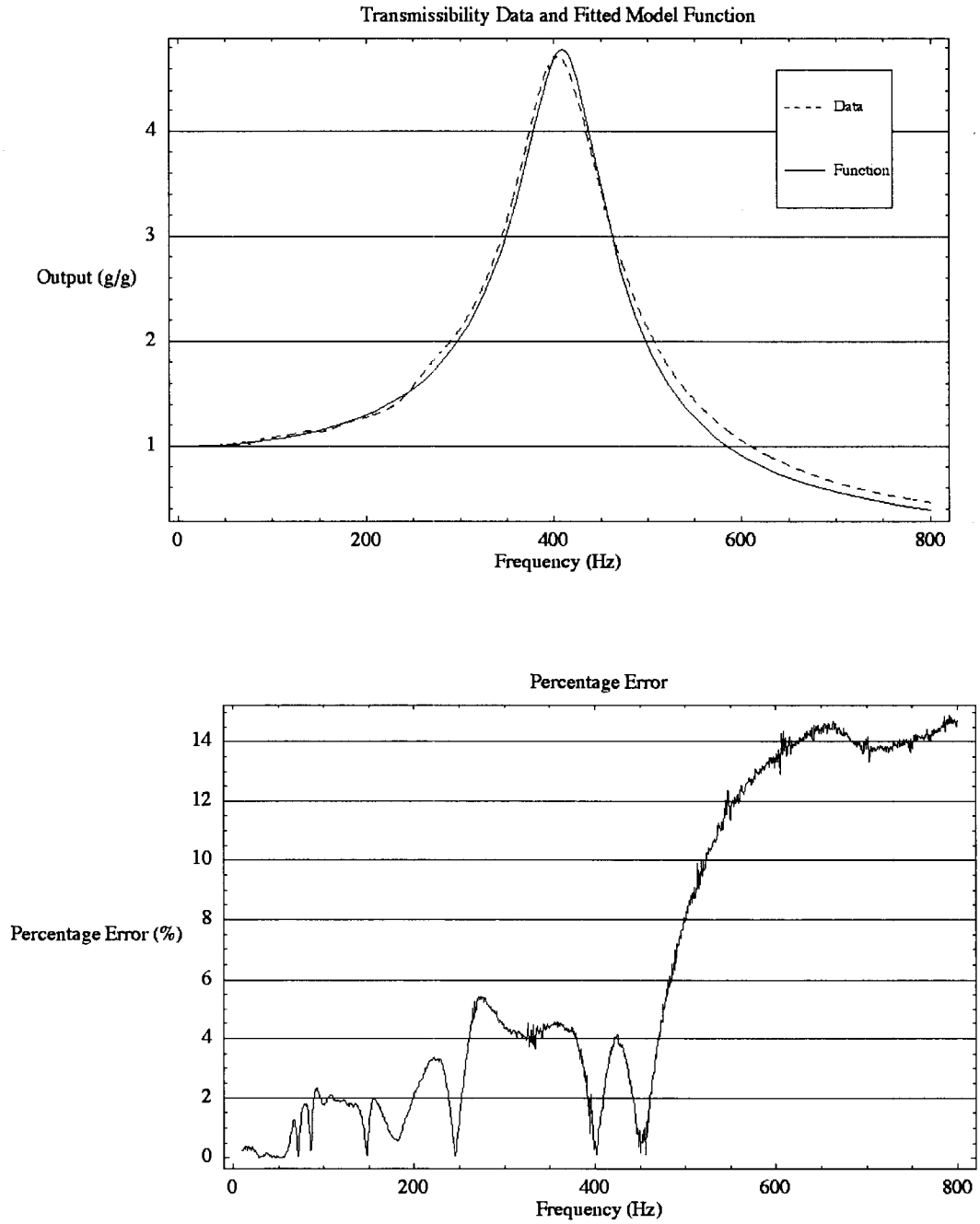

Figure D 11: 2V Sweep Mass Spring Damper Model Plots

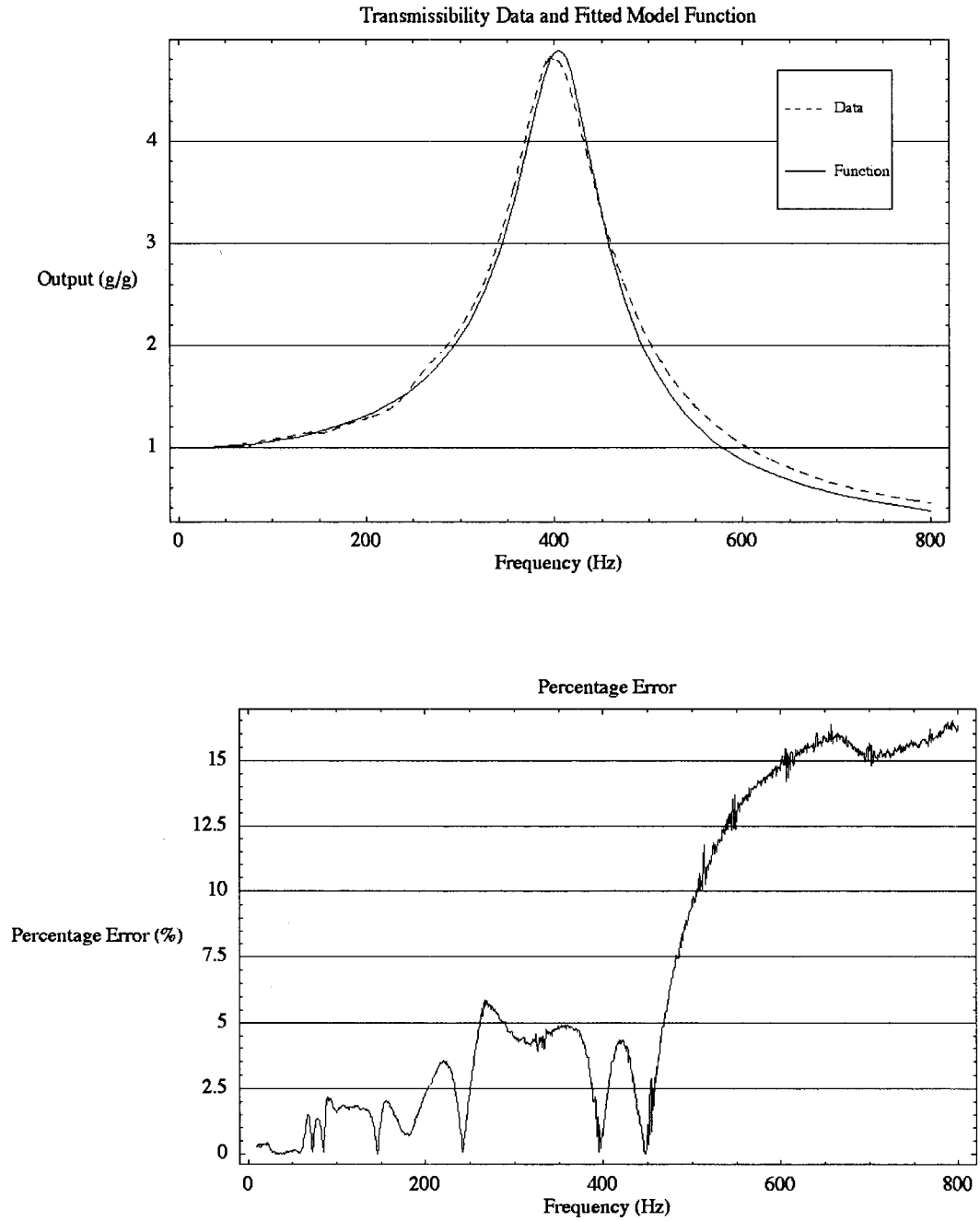

Figure D 12: 4V Sweep Mass Spring Damper Model Plots

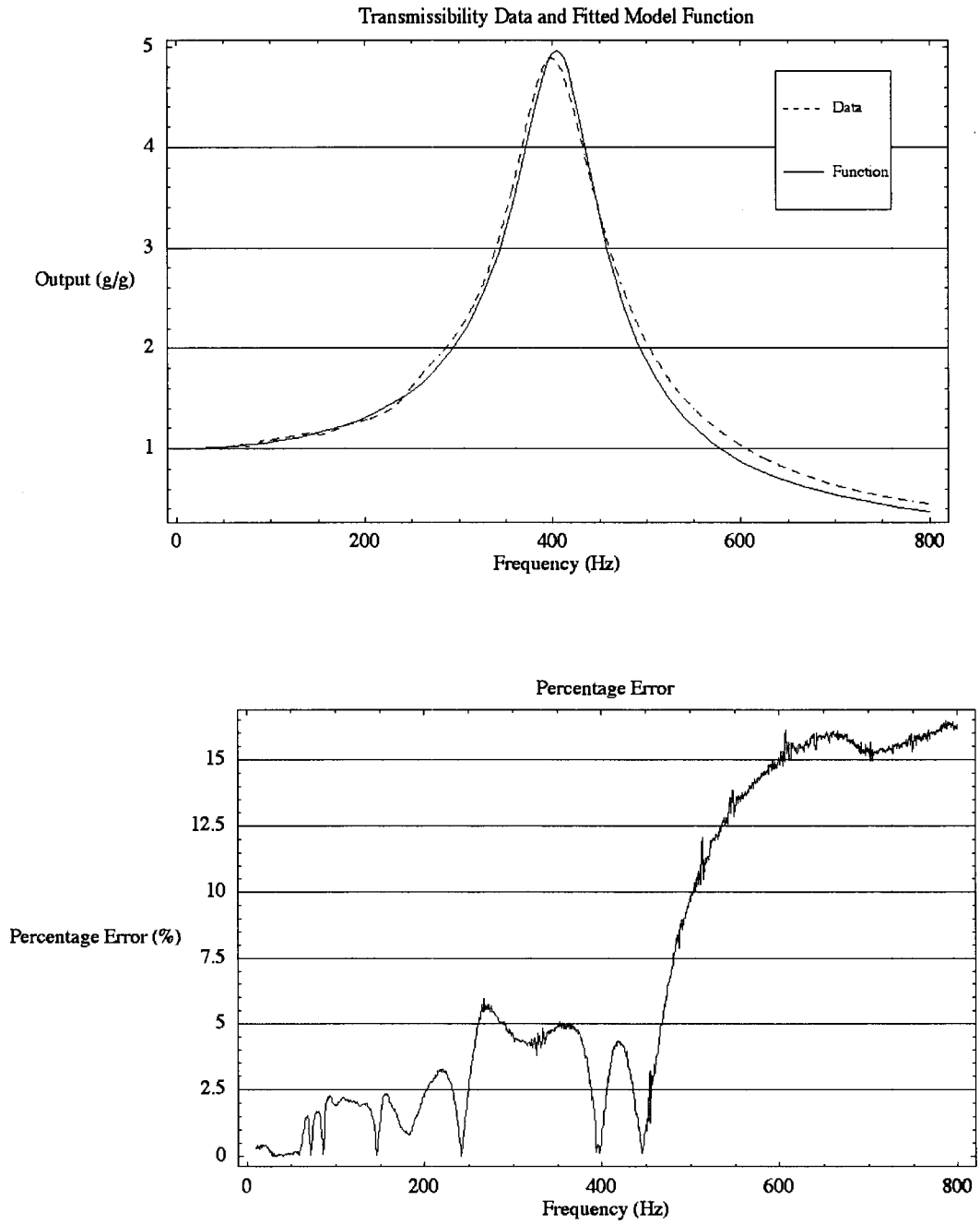

Figure D 13: 6V Sweep Mass Spring Damper Model Plots

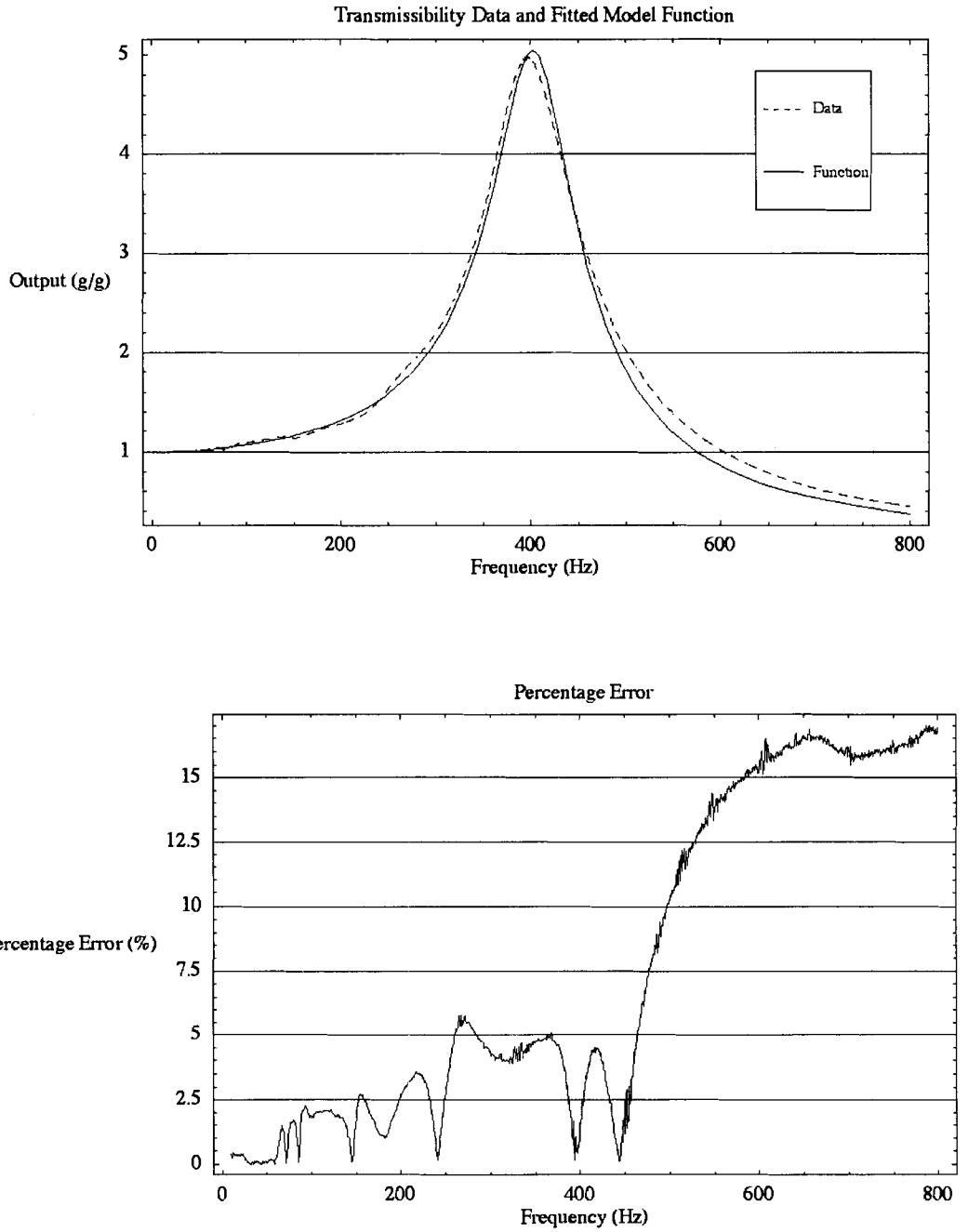

Figure D 14: 8V Sweep Mass Spring Damper Model Plots

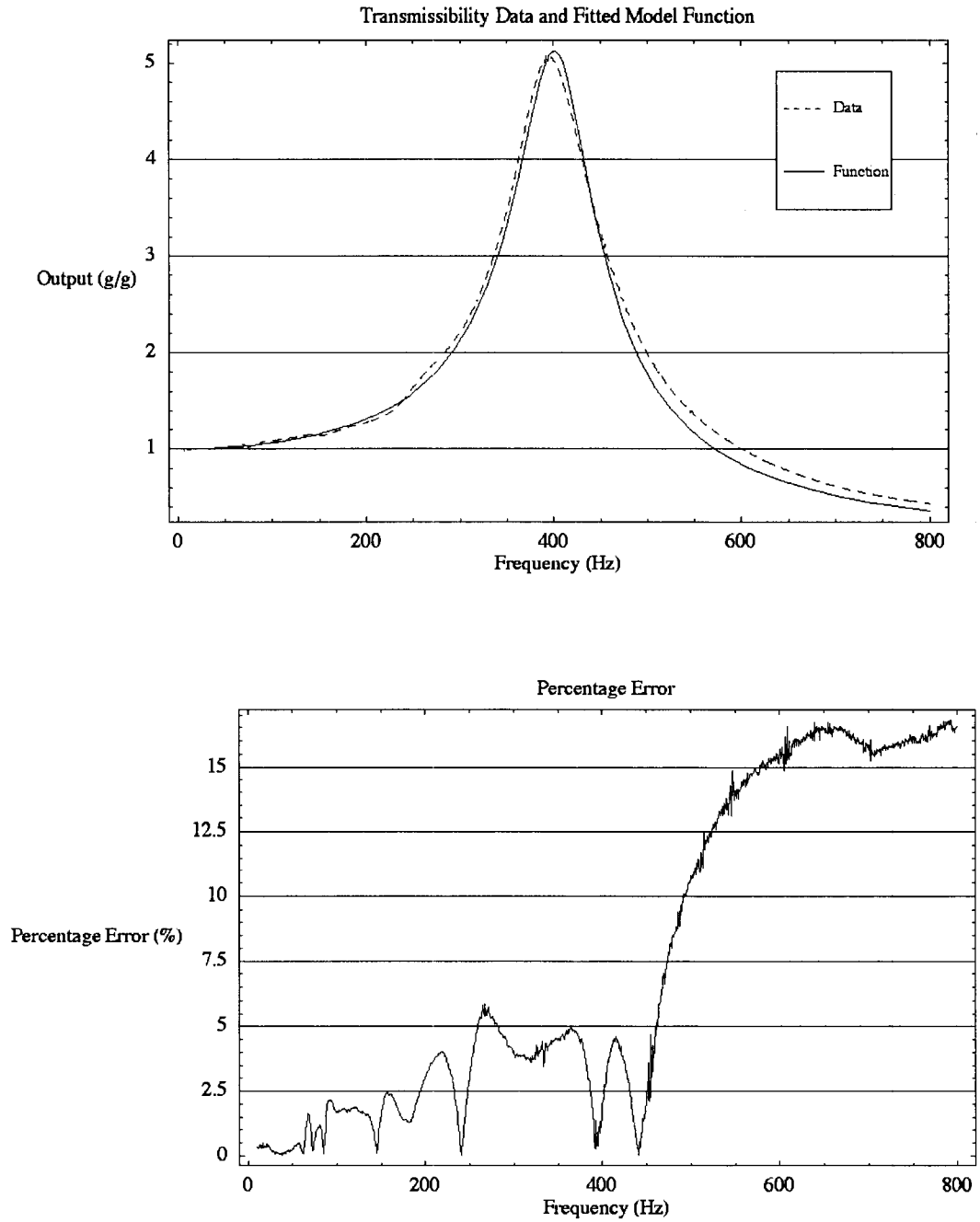

Figure D 15: 10V Sweep Mass Spring Damper Model Plots

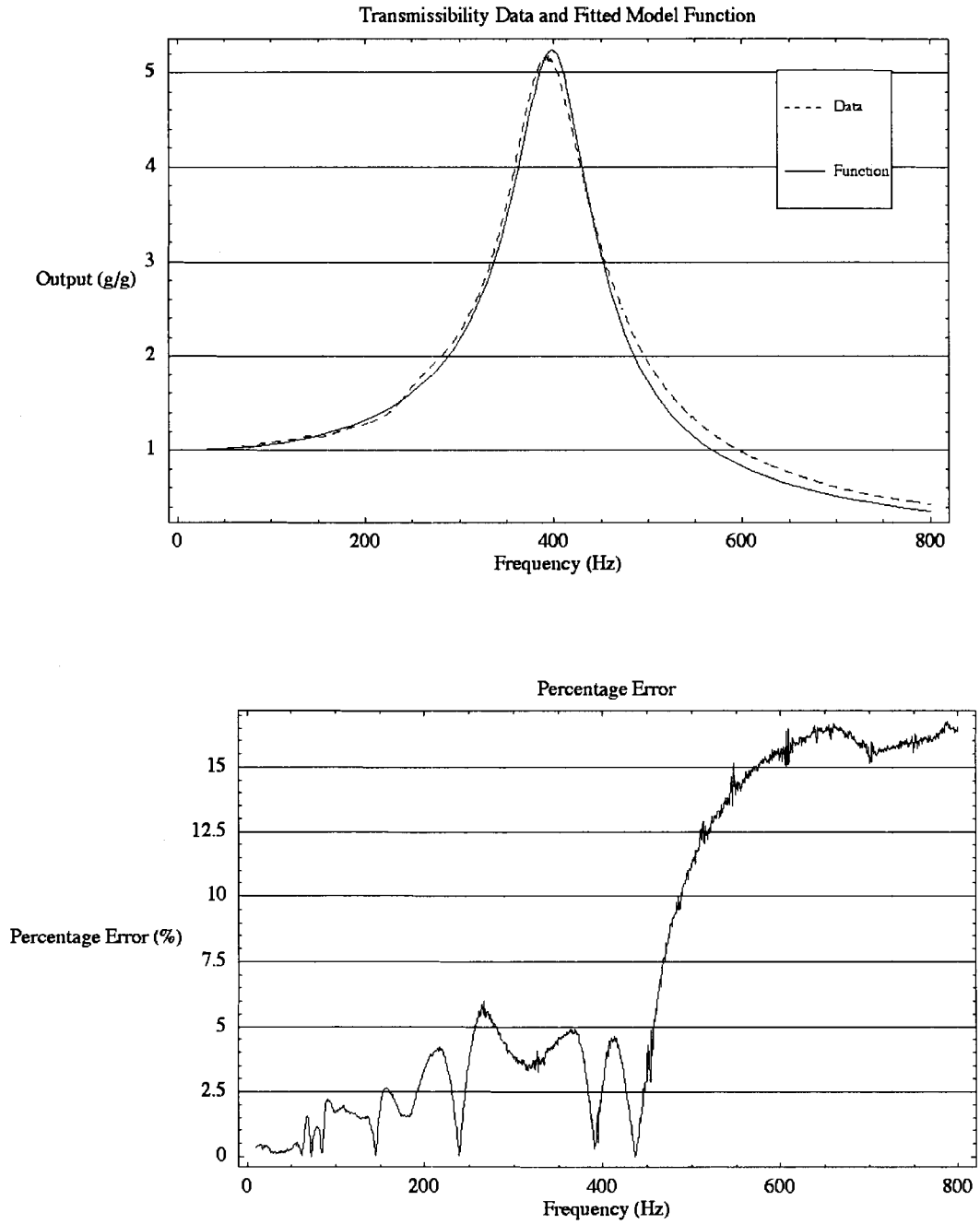

Figure D 16: 12V Sweep Mass Spring Damper Model Plots

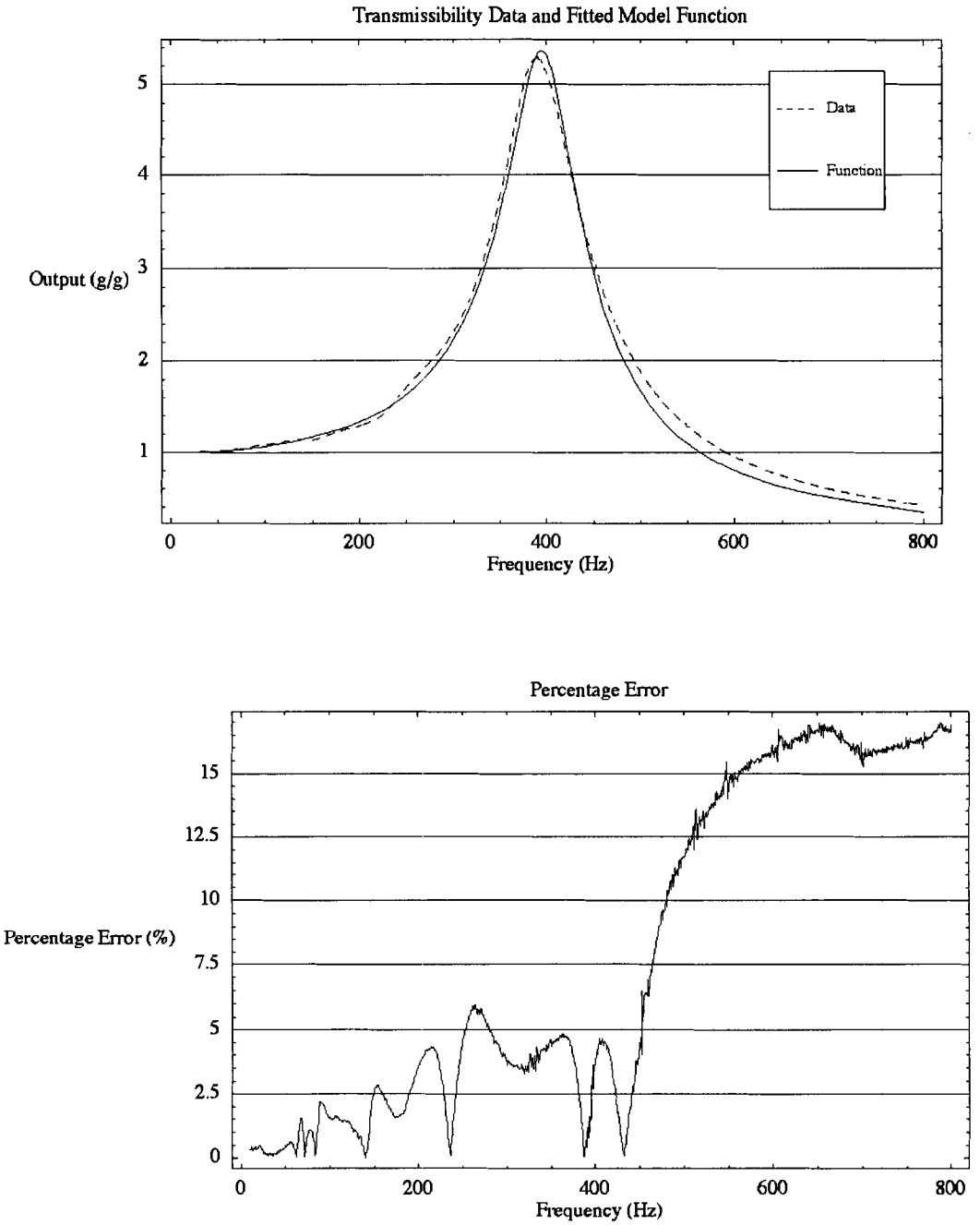

Figure D 17: 14V Sweep Mass Spring Damper Model Plots

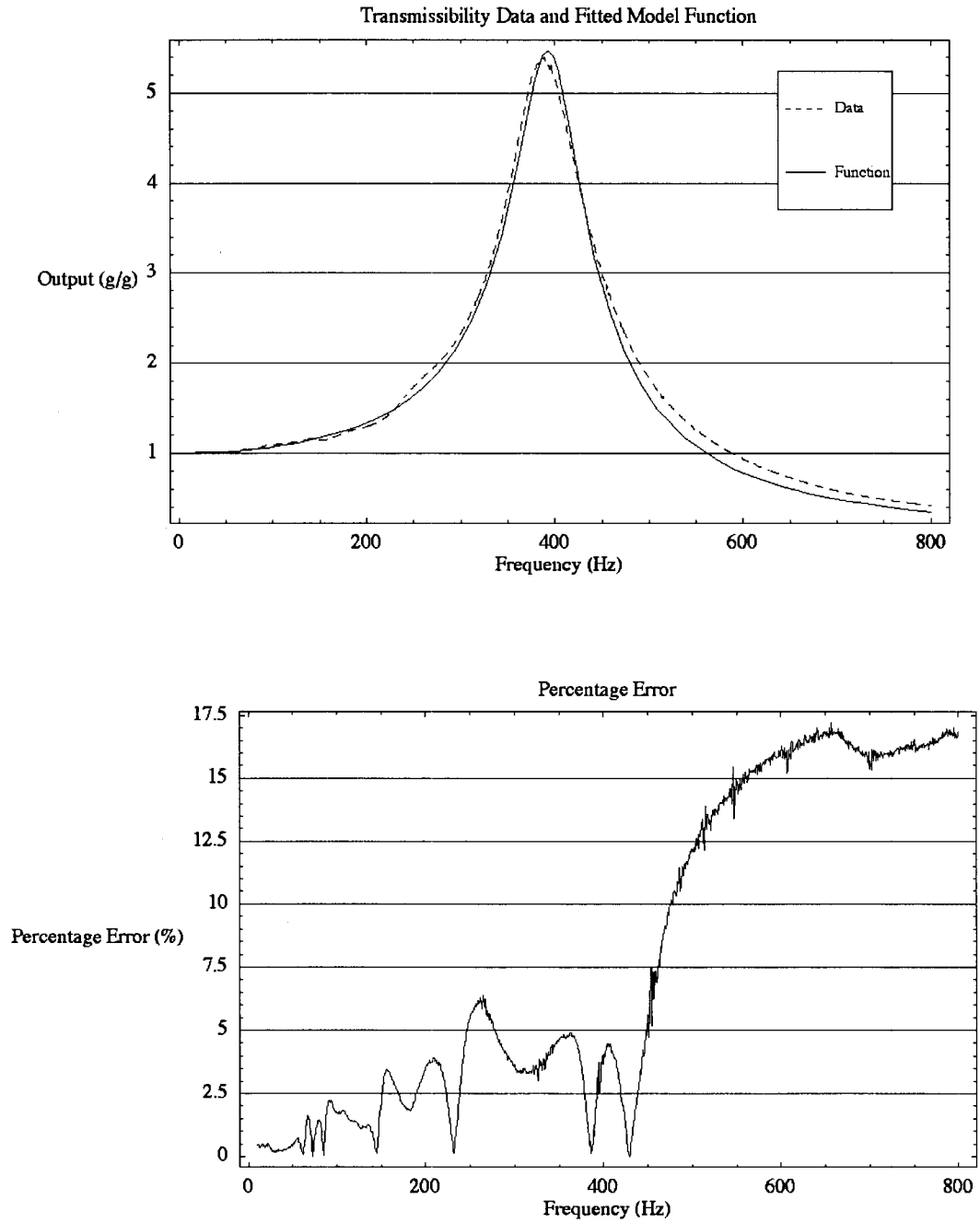

Figure D 18: 16V Sweep Mass Spring Damper Model Plots

Viscoelastic Material Mathematical Model

The final mathematical model fit to the derived transmissibility data was the magnitude function for the viscoelastic material model given by

$$\left| \frac{k[\omega]\,(j\eta[\omega] + 1)}{M\,(j\omega)^2 + k[\omega]\,(j\eta[\omega] + 1)} \right| . \qquad \textbf{Equation D 3}$$

Recall that two separate viscoelastic material models were fitted to the transmissibility data. The linear viscoelastic model assumes that the complex stiffness function is composed of linear real stiffness and complex loss functions, and the quadratic viscoelastic model assumes that the complex stiffness function is composed of quadratic real stiffness and complex loss functions. The equations and plots corresponding to each of the two viscoelastic material models are shown in the next two sub-sections.

Linear Viscoelastic Material Model

The linear viscoelastic model real stiffness and complex loss functions are given by

$$k[\omega] = k_1\,\omega + k_0 , \qquad \textbf{Equation D 4}$$

and

$$\eta[\omega] = \frac{C_1\,\omega + C_0}{k_1\,\omega + k_0} . \qquad \textbf{Equation D 5}$$

A table of all function and equation coefficients is shown in Table D 2.

Table D 2: Linear Viscoelastic Model Equation and Function Coefficients

Electromagnet Voltage (V)	k_0	k_1	C_0	C_1
0	2.098×10^6	517.1	1.956×10^6	-475.8
2	2.132×10^6	486.1	1.955×10^6	-488.2
4	2.021×10^6	504.7	1.953×10^6	-505.6
6	2.031×10^6	502.7	1.935×10^6	-501.7
8	1.985×10^6	509.5	1.978×10^6	-529.2
10	1.985×10^6	501.8	1.977×10^6	-537.6
12	1.980×10^6	490.8	1.950×10^6	-539.2
14	1.969×10^6	480.7	1.894×10^6	-530.1
16	1.982×10^6	467.8	1.835×10^6	-514.7

The resonant frequencies and corresponding transmissibility magnitude acquired from the fitted liner viscoelastic magnitude function for each transmissibility dataset are shown in Table D 3.

Table D 3: Acquired Resonant Frequencies from the Linear Viscoelastic Transmissibility Models

Electromagnet Voltage (V)	Resonant Frequency (Hz)	Transmissibility Magnitude	Resonant Frequency Percentage Change (%)
0	409.3	4.647	N/A
2	405.8	4.706	-0.842
4	401.5	4.803	-1.907
6	401.5	4.869	-1.893
8	399.8	4.950	-2.324
10	398.2	5.034	-2.706
12	395.4	5.145	-3.377
14	392.3	5.267	-4.157
16	390.2	5.364	-4.649

The plots corresponding to the linear viscoelastic model fit for each derived transmissibility dataset comprise a composite dataset and fitted function plot, and a percentage error plot.

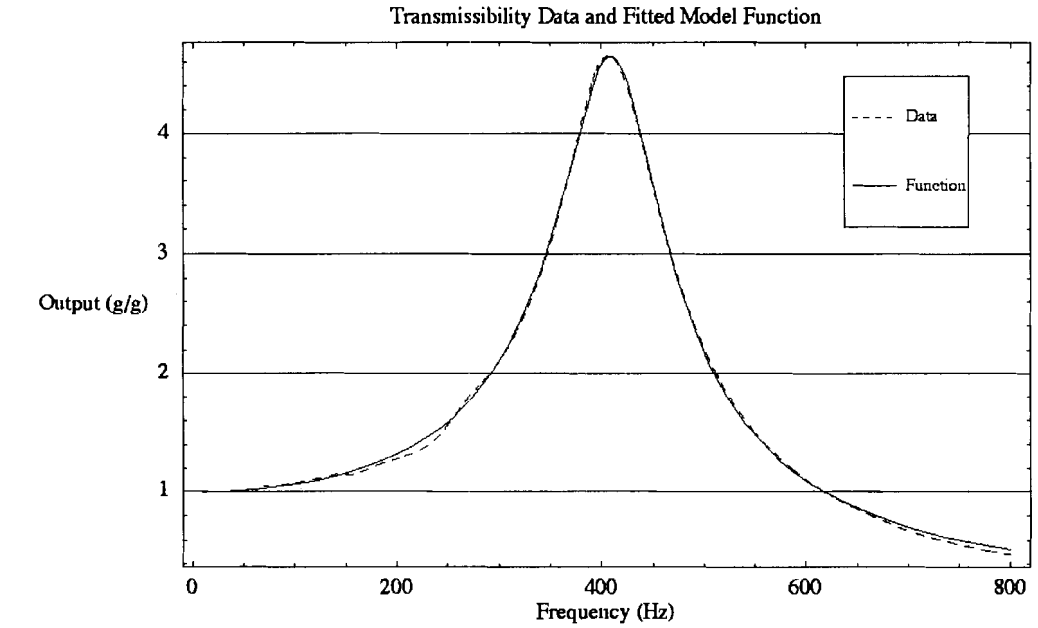

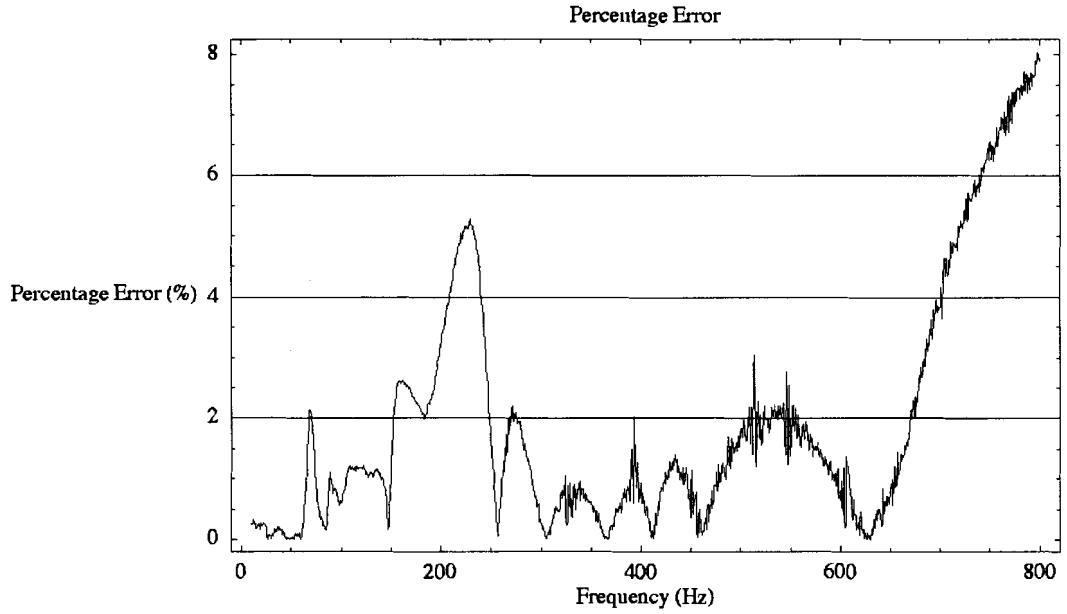

Figure D 19: 0V Sweep Linear Viscoelastic Model Plots

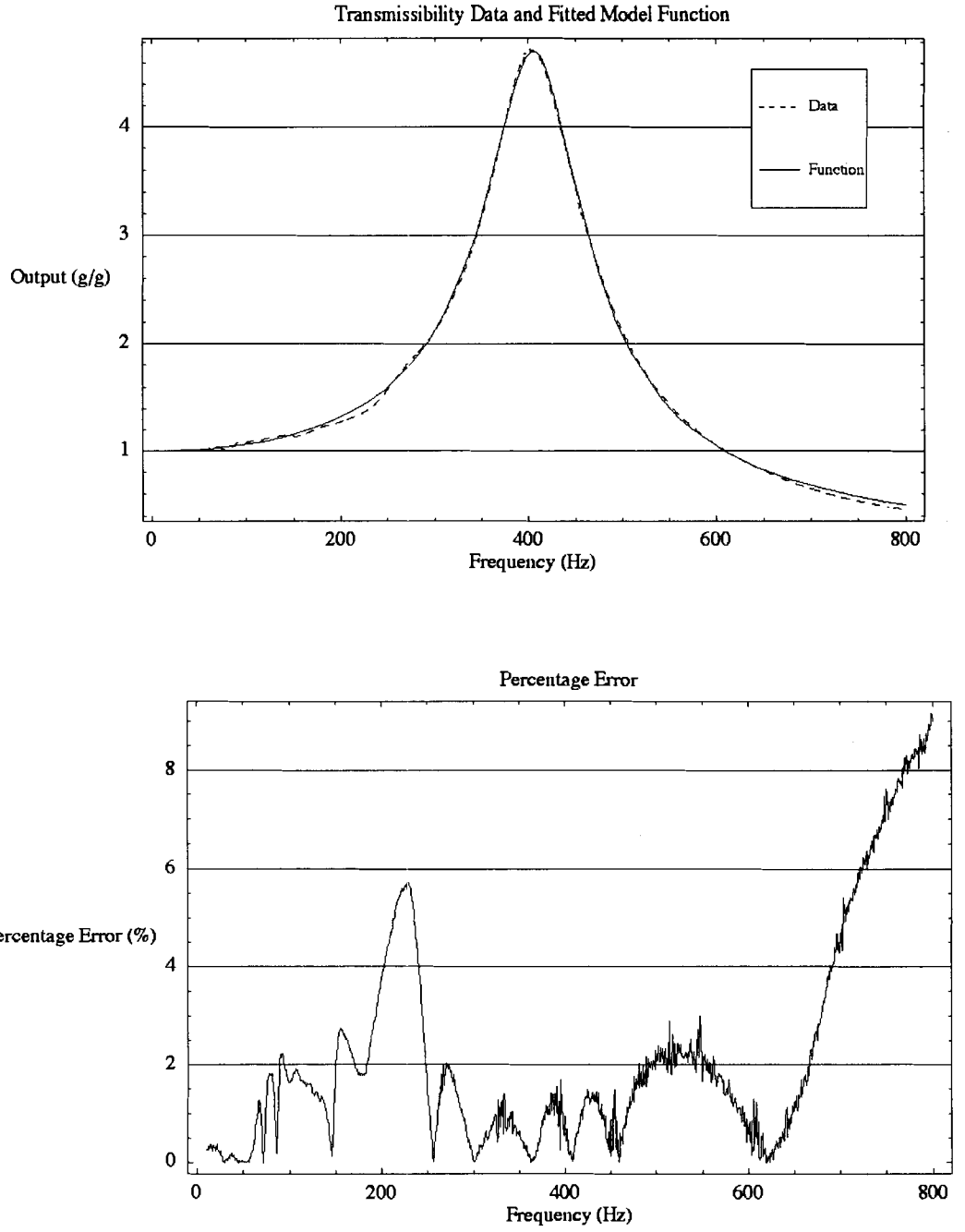

Figure D 20: 2V Sweep Linear Viscoelastic Model Plots

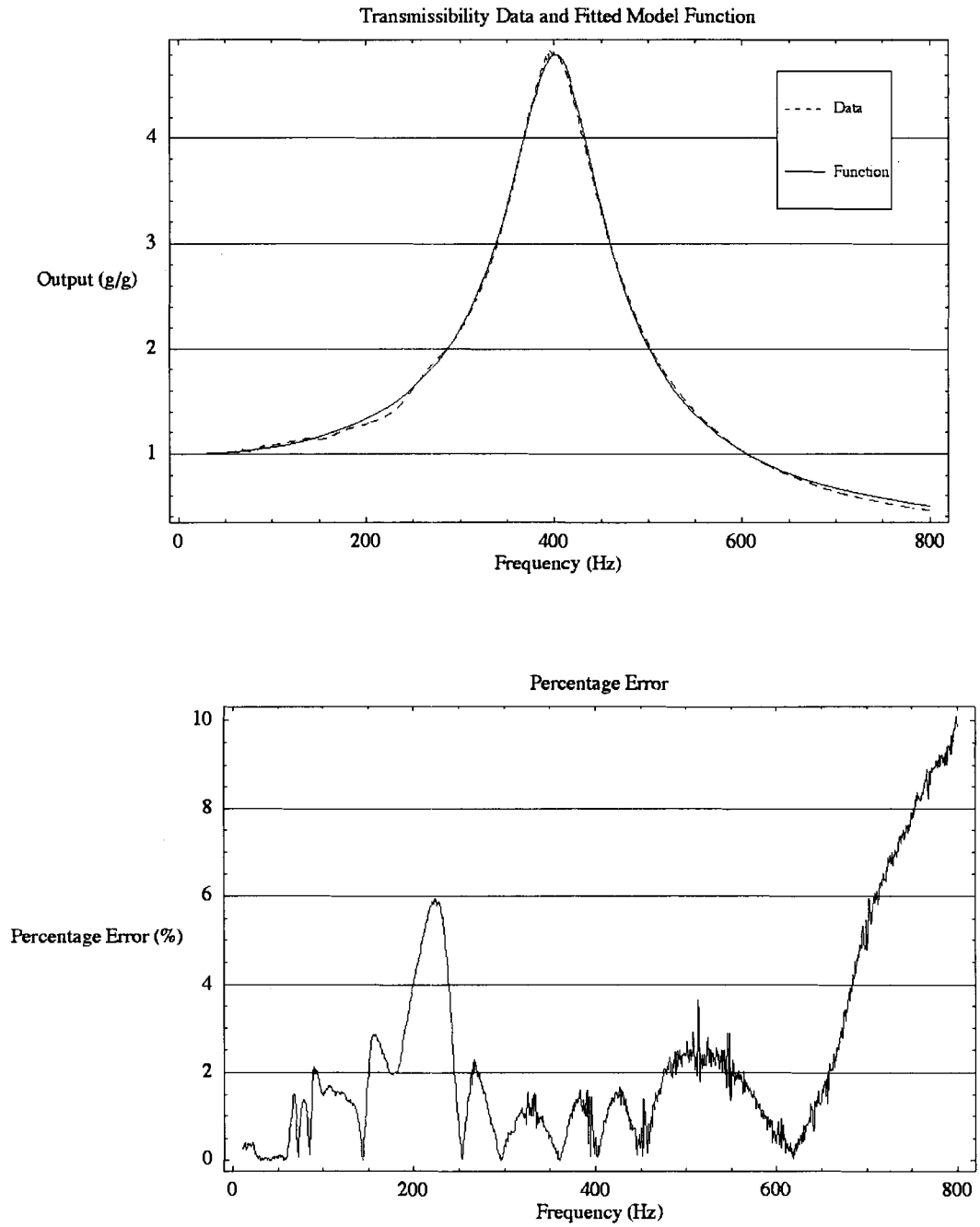

Figure D 21: 4V Sweep Linear Viscoelastic Model Plots

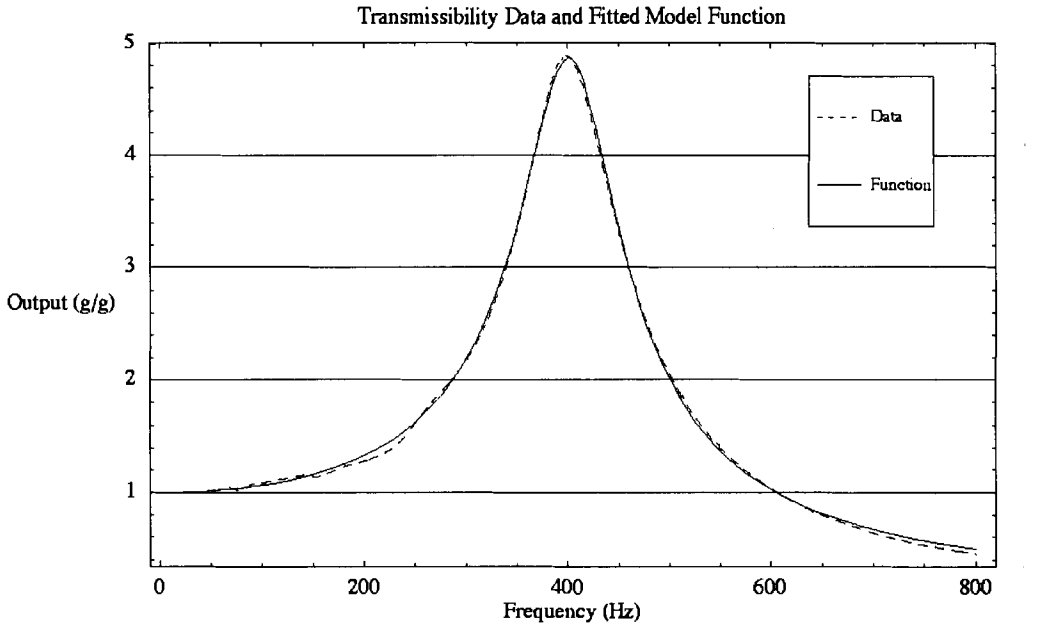

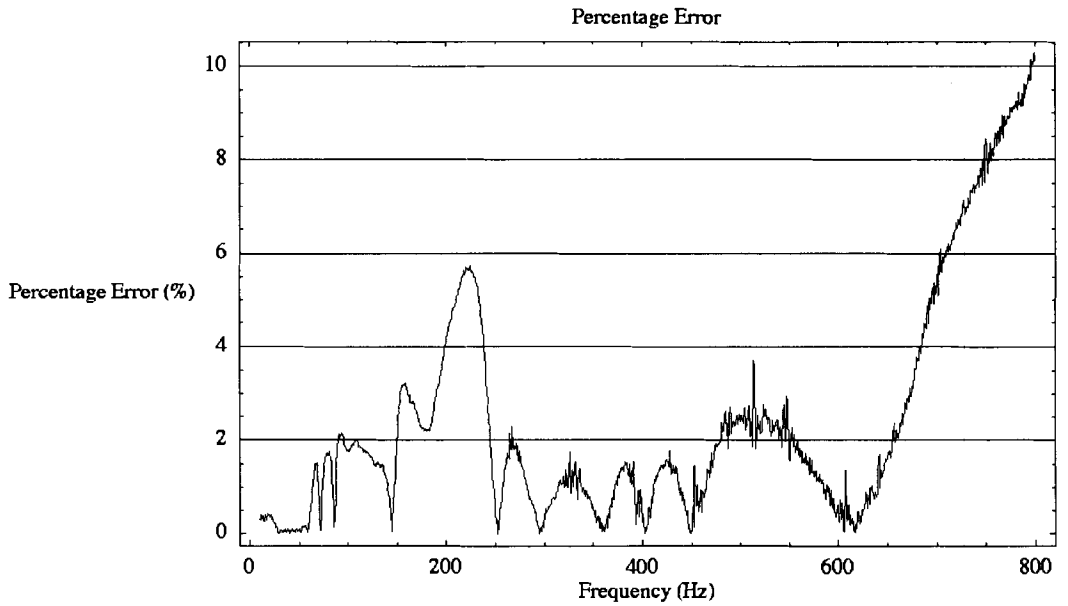

Figure D 22: 6V Sweep Linear Viscoelastic Model Plots

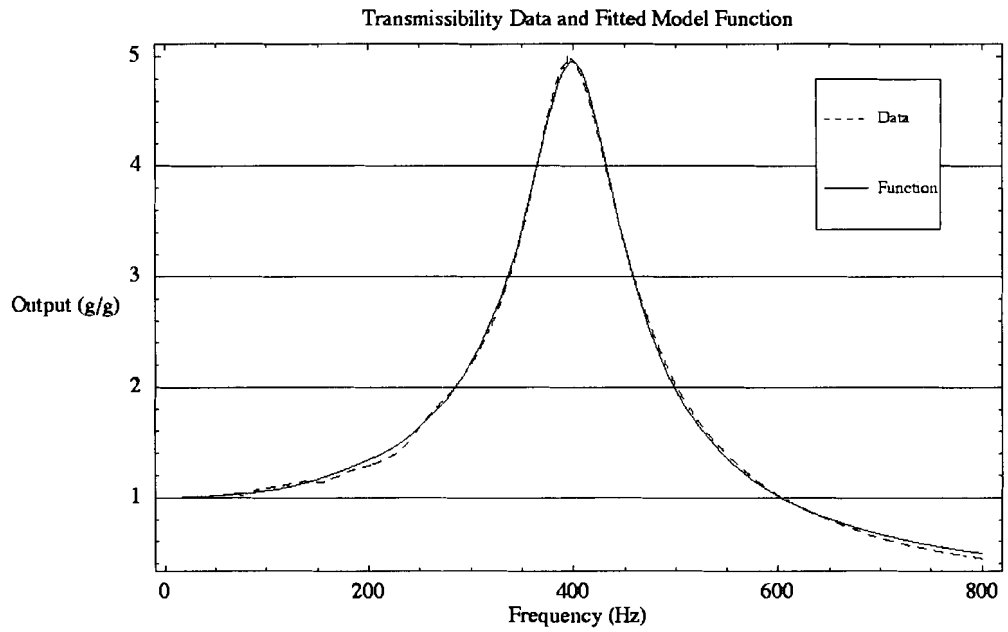

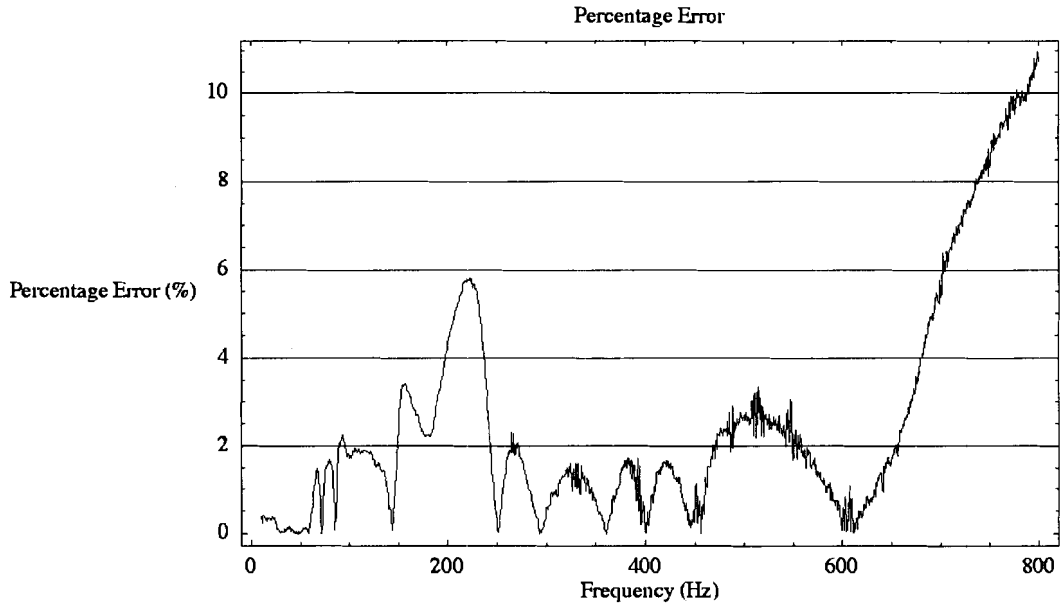

Figure D 23: 8V Sweep Linear Viscoelastic Model Plots

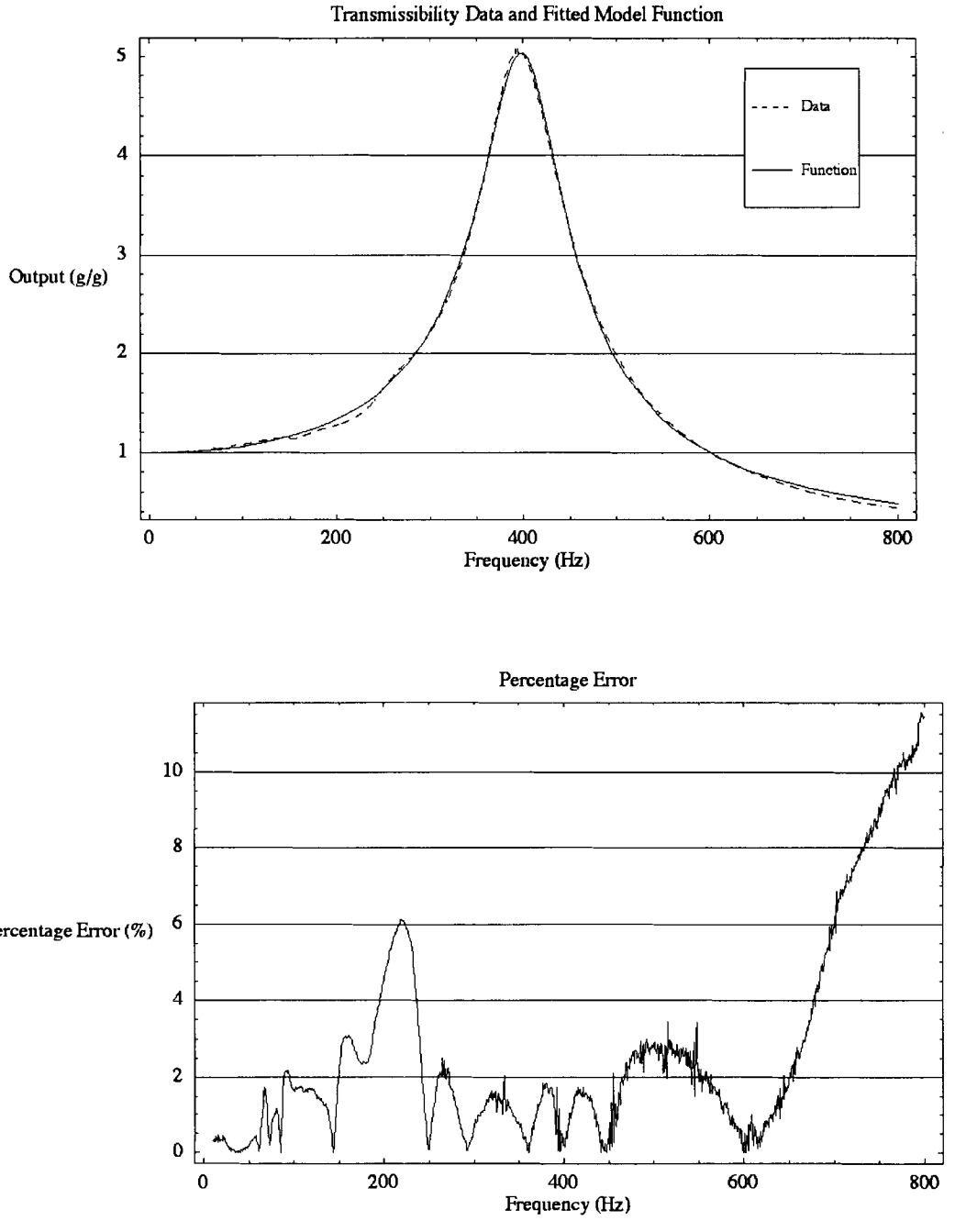

Figure D 24: 10V Sweep Linear Viscoelastic Model Plots

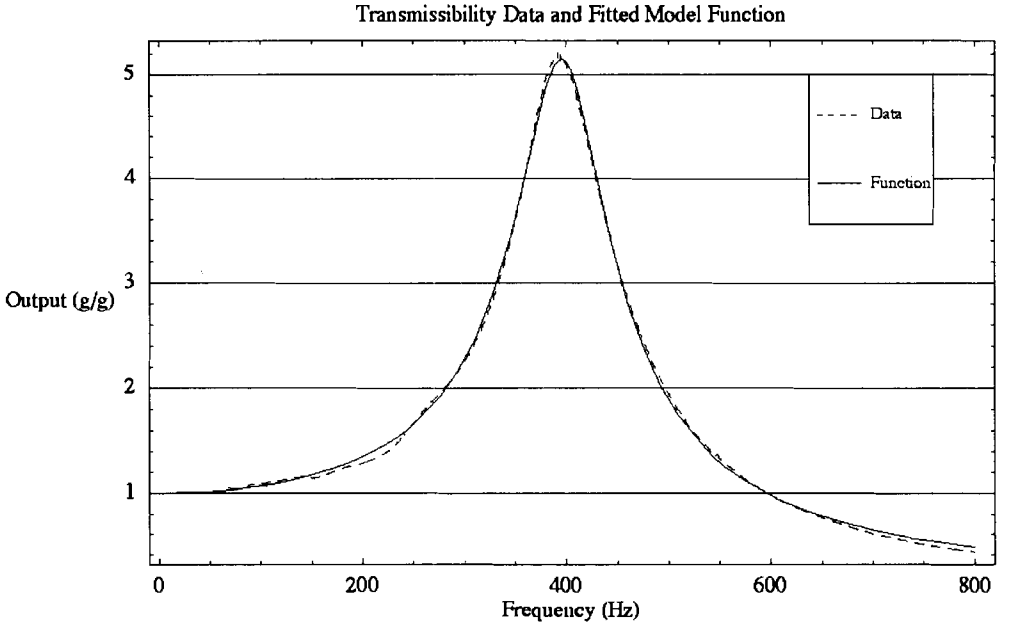

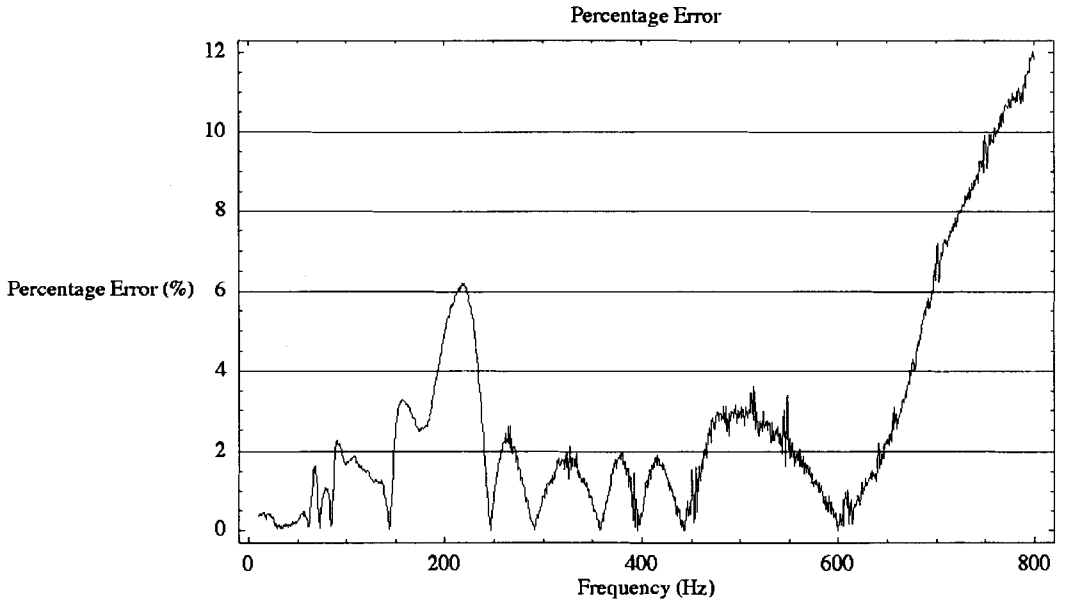

Figure D 25: 12V Sweep Linear Viscoelastic Model Plots

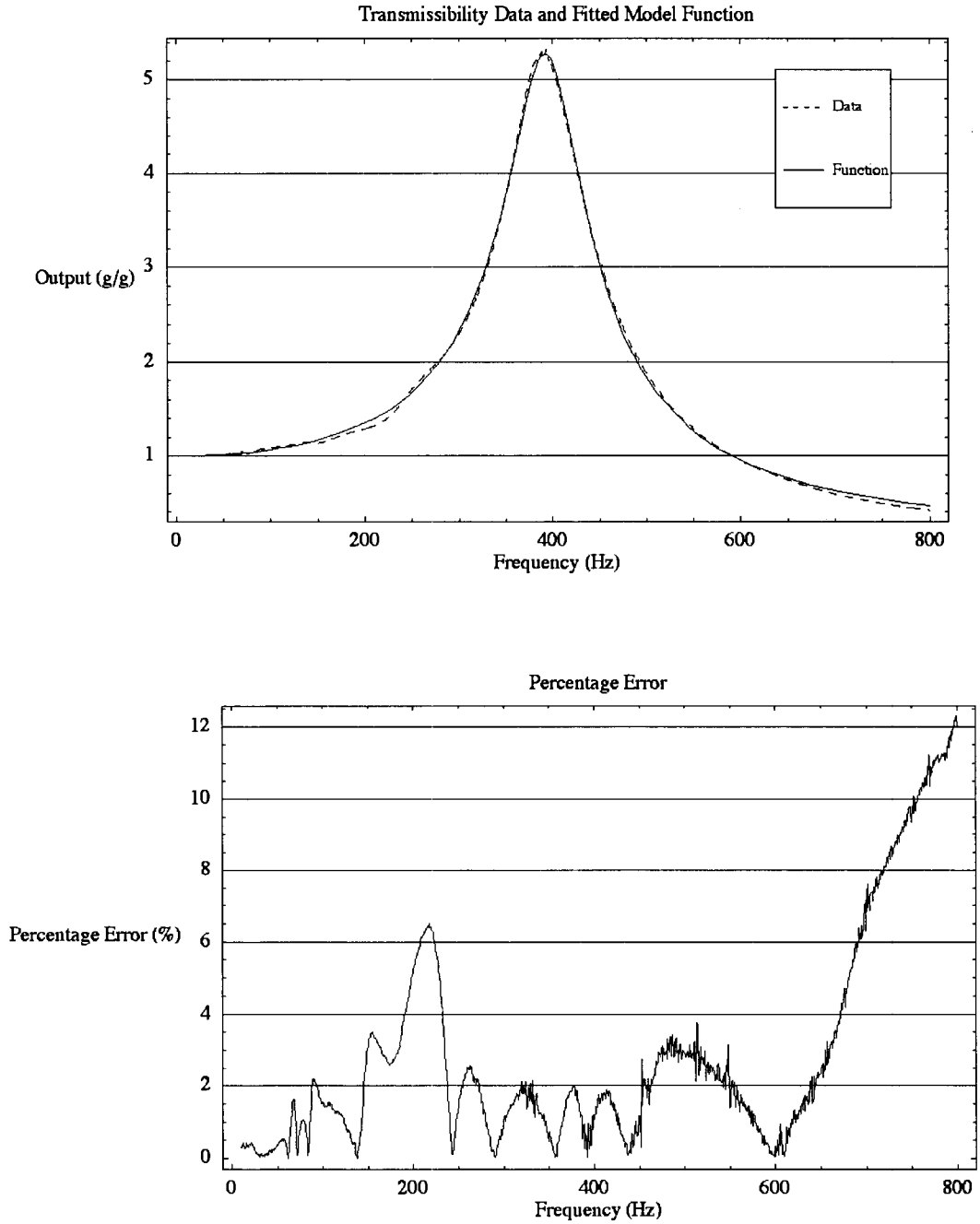

Figure D 26: 14V Sweep Linear Viscoelastic Model Plots

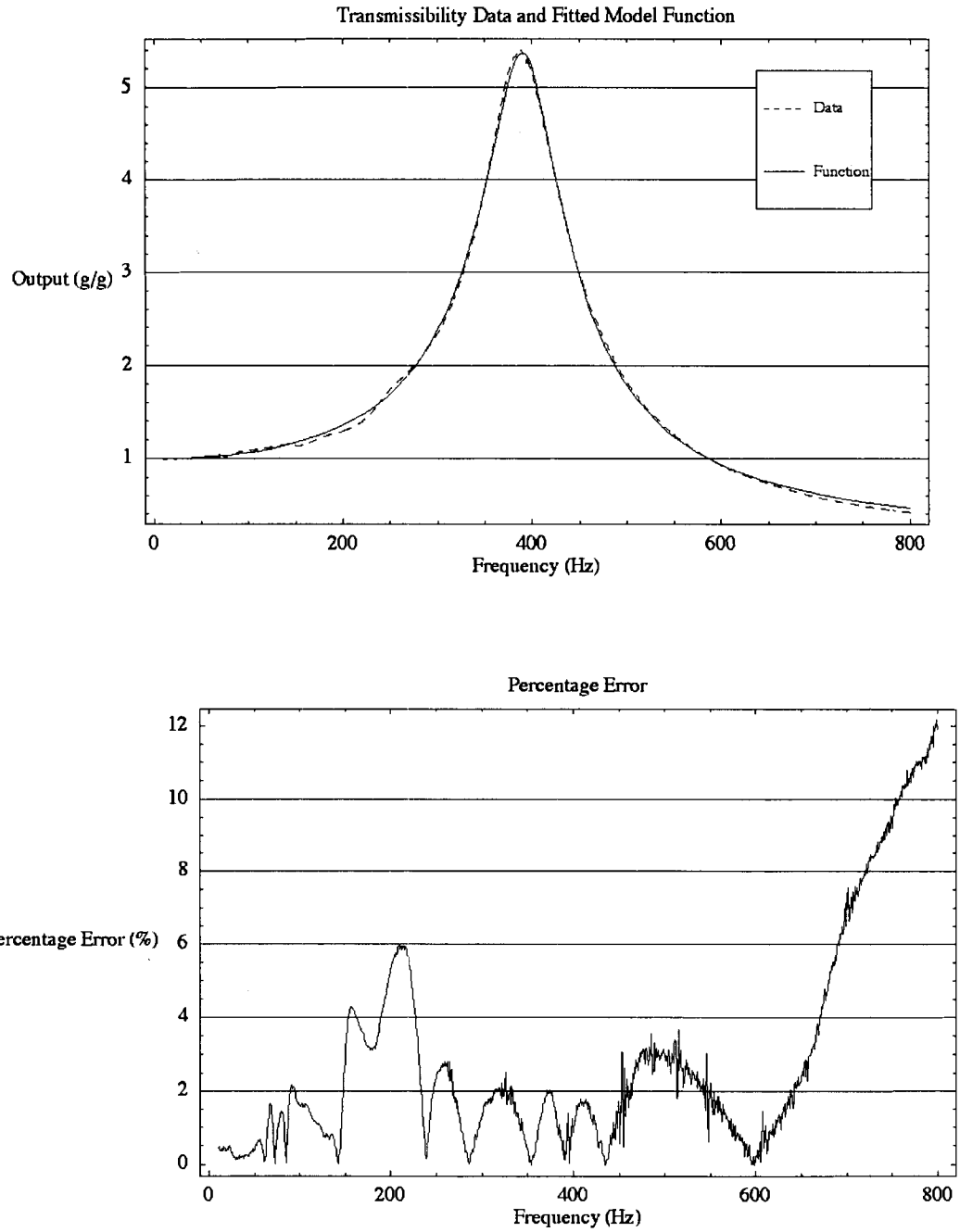

Figure D 27: 16V Sweep Linear Viscoelastic Model Plots

Quadratic Visco-Elastic Material Model

The quadratic viscoelastic model real stiffness and complex loss functions are given by

$$k[\omega] = k_2 \omega^2 + k_1 \omega + k_0, \qquad \textbf{Equation D 6}$$

and

$$\eta[\omega] = \frac{C_2 \omega^2 + C_1 \omega + C_0}{k_2 \omega^2 + k_1 \omega + k_0}. \qquad \textbf{Equation D 7}$$

A table of all function and equation coefficients is shown in Table D 4.

Table D 4: Quadratic Visco-Elastic Model Equation and Function Coefficients

Electromagnet Voltage (V)	k_0	k_1	k_2	C_0	C_1	C_2
0	3.121×10^6	383.5	-3.308×10^{-2}	3.327×10^6	2.242×10^{-1}	-2185
2	3.133×10^6	358.0	-3.406×10^{-2}	3.490×10^6	2.461×10^{-1}	-2304
4	3.008×10^6	376.9	-3.377×10^{-2}	3.562×10^6	2.568×10^{-1}	-2357
6	2.975×10^6	393.8	-3.582×10^{-2}	3.567×10^6	2.571×10^{-1}	-2356
8	2.934×10^6	401.1	-3.655×10^{-2}	3.652×10^6	2.622×10^{-1}	-2399
10	2.907×10^6	402.3	-3.745×10^{-2}	3.696×10^6	2.679×10^{-1}	-2427
12	2.850×10^6	408.4	-3.902×10^{-2}	3.679×10^6	2.685×10^{-1}	-2418
14	2.762×10^6	427.2	-4.194×10^{-2}	3.615×10^6	2.657×10^{-1}	-2383
16	2.716×10^6	430.8	-4.276×10^{-2}	3.453×10^6	2.504×10^{-1}	-2277

The resonant frequencies and corresponding transmissibility magnitude acquired from the fitted quadratic viscoelastic magnitude function for each transmissibility dataset are shown in

Table D 5.

Table D 5: Acquired Resonant Frequencies from the Quadratic Viscoelastic Transmissibility Models

Electromagnet Voltage (V)	Resonant Frequency (Hz)	Transmissibility Magnitude	Resonant Frequency Percentage Change (%)
0	408.5	4.633	N/A
2	405.0	4.692	-0.861
4	400.6	4.788	-1.937
6	400.7	4.853	-1.920
8	398.9	4.935	-2.353
10	397.4	5.018	-2.737
12	394.6	5.129	-3.406
14	391.5	5.251	-4.181
16	389.5	5.349	-4.657

The plots corresponding to the quadratic viscoelastic model fit for each derived transmissibility dataset comprise a composite dataset and fitted function plot, and a percentage error plot.

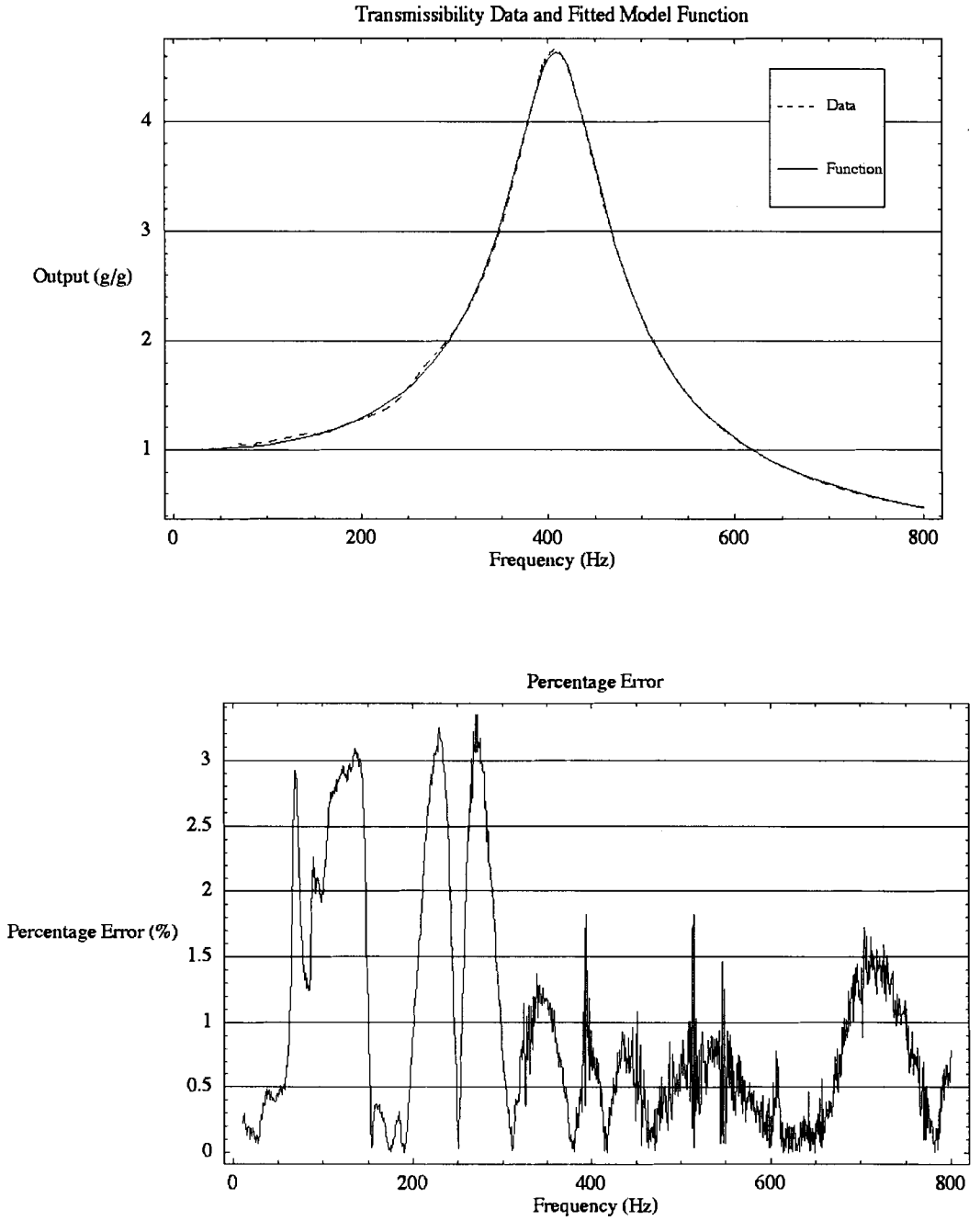

Figure D 28: 0V Sweep Quadratic Viscoelastic Model Plots

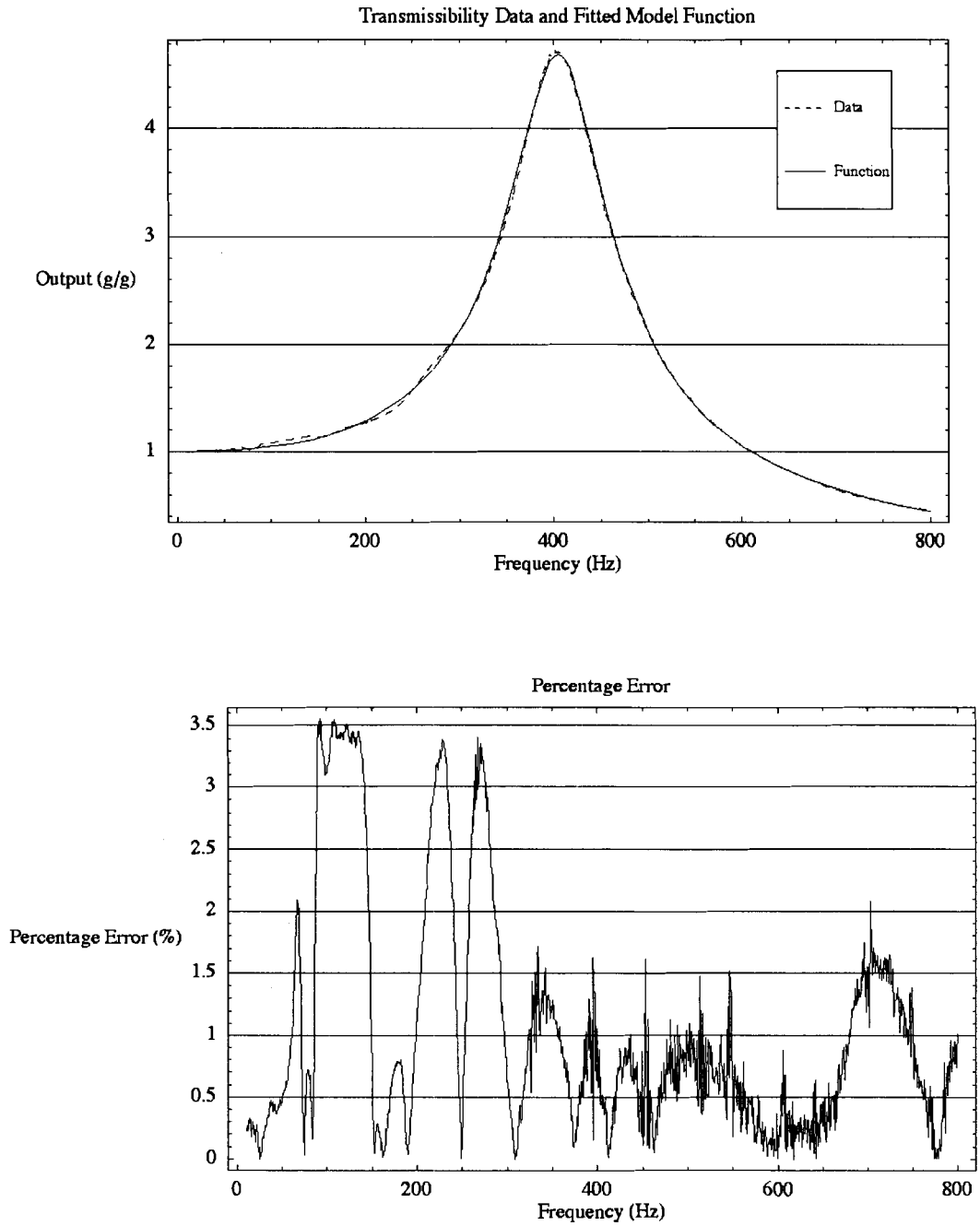

Figure D 29: 2V Sweep Quadratic Viscoelastic Model Plots

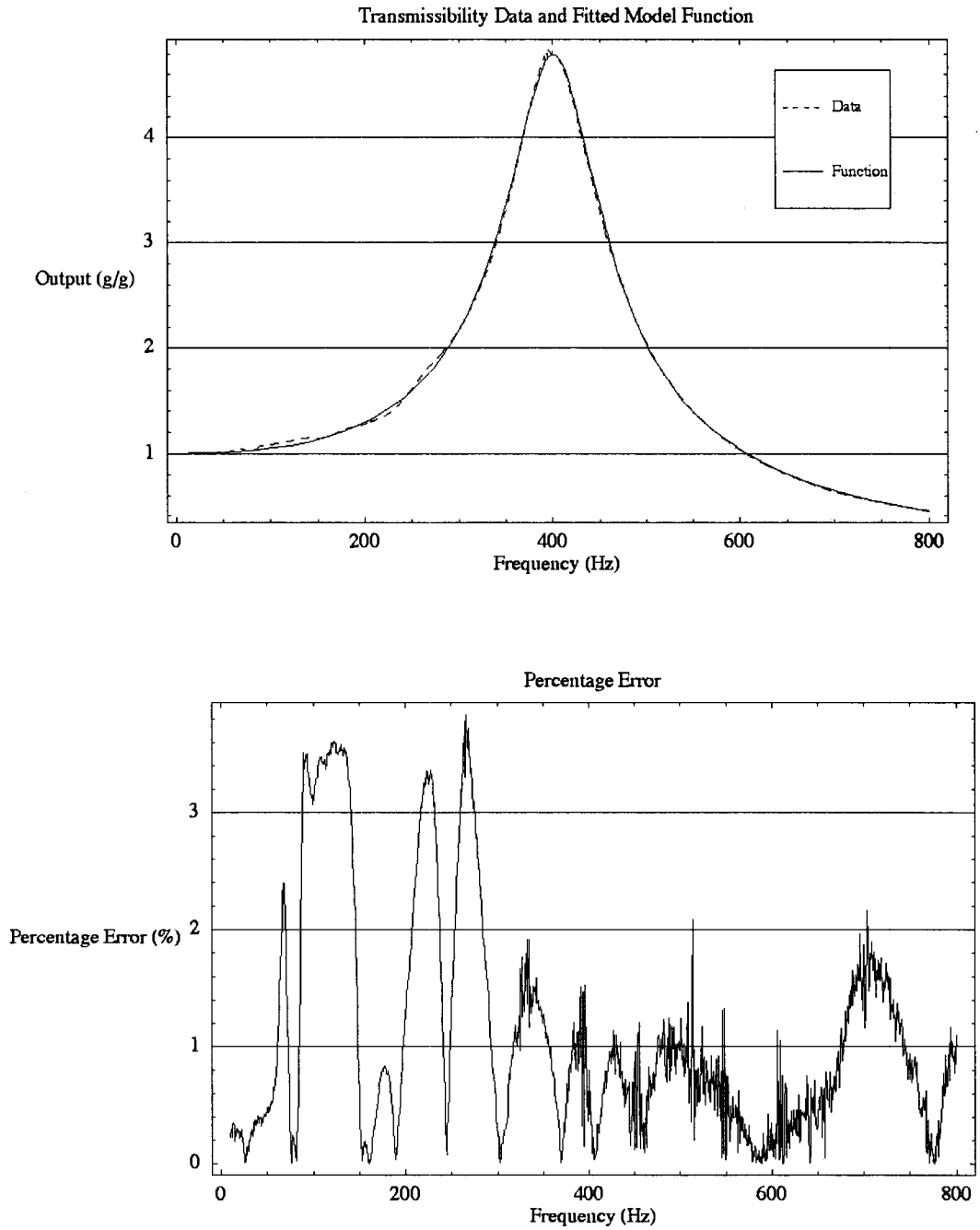

Figure D 30: 4V Sweep Quadratic Viscoelastic Model Plots

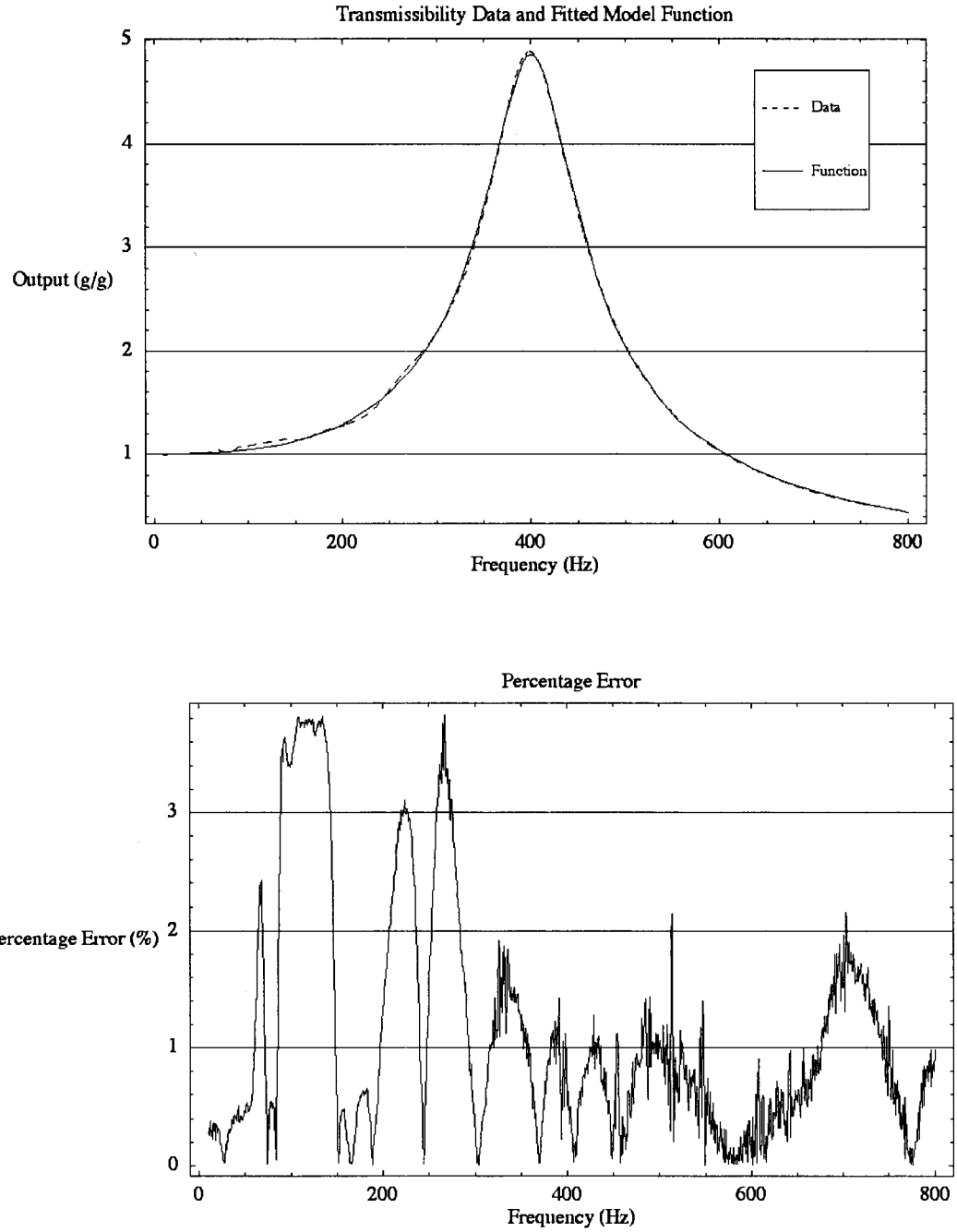

Figure D 31: 6V Sweep Quadratic Viscoelastic Model Plots

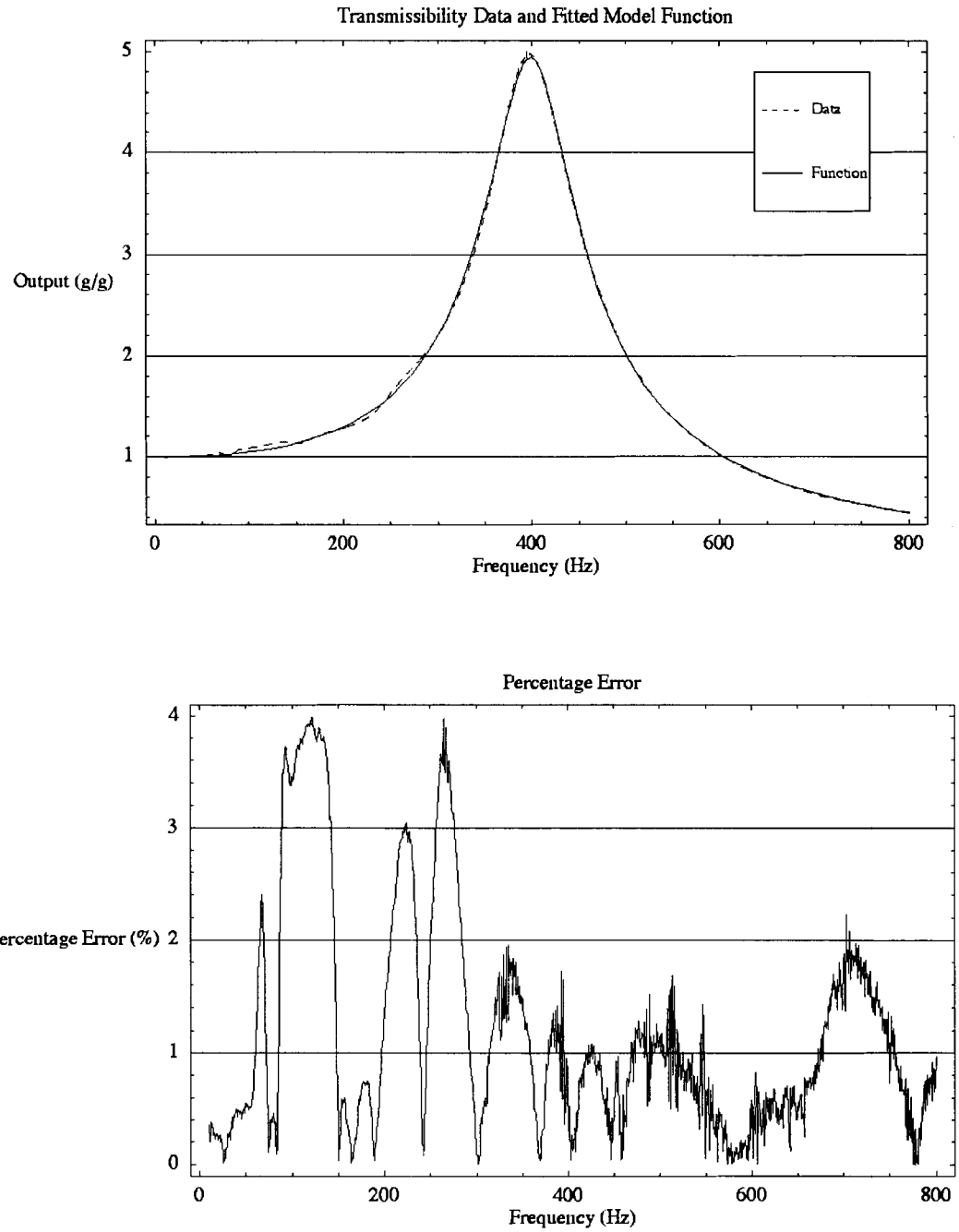

Figure D 32: 8V Sweep Quadratic Viscoelastic Model Plots

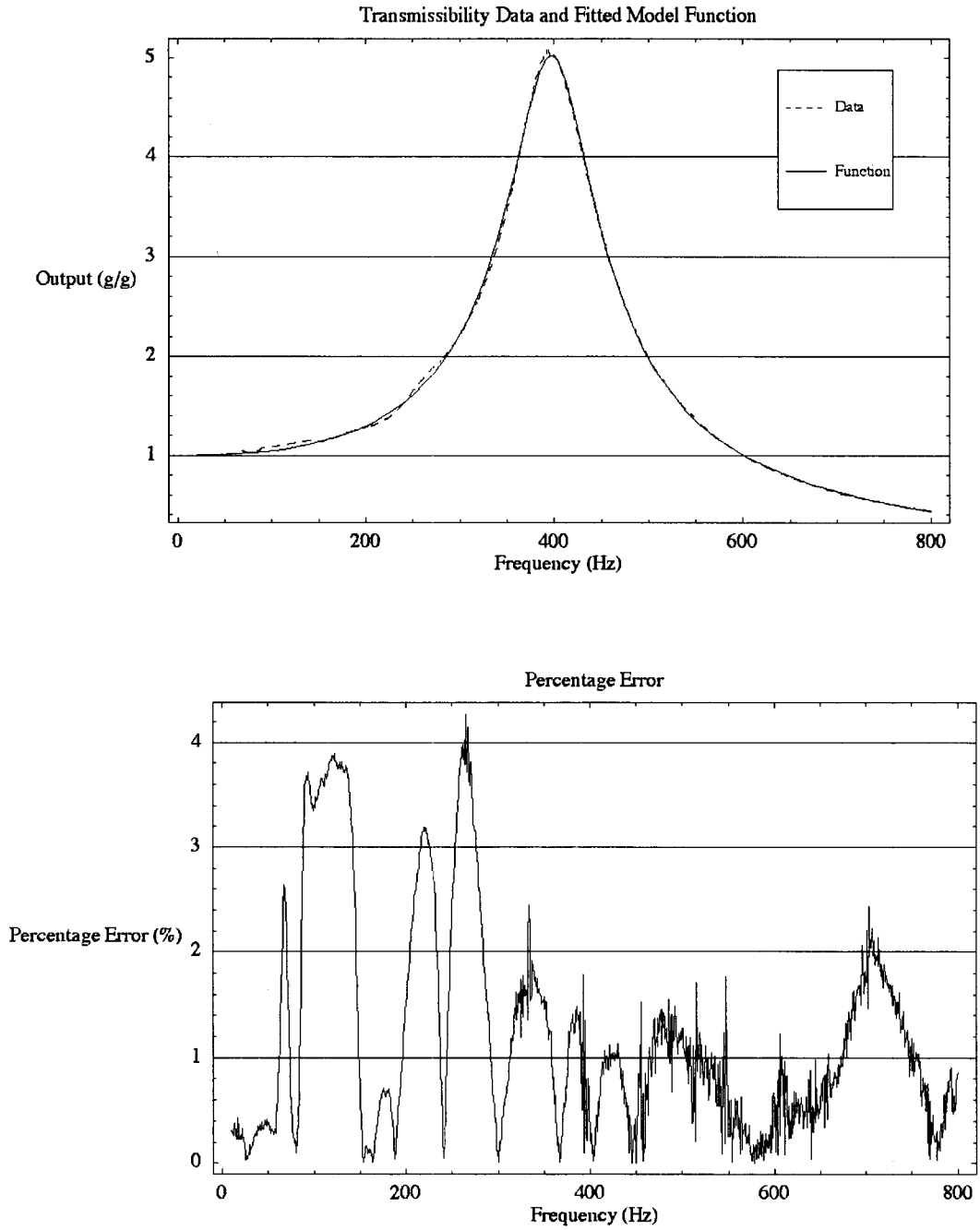

Figure D 33: 10V Sweep Quadratic Viscoelastic Model Plots

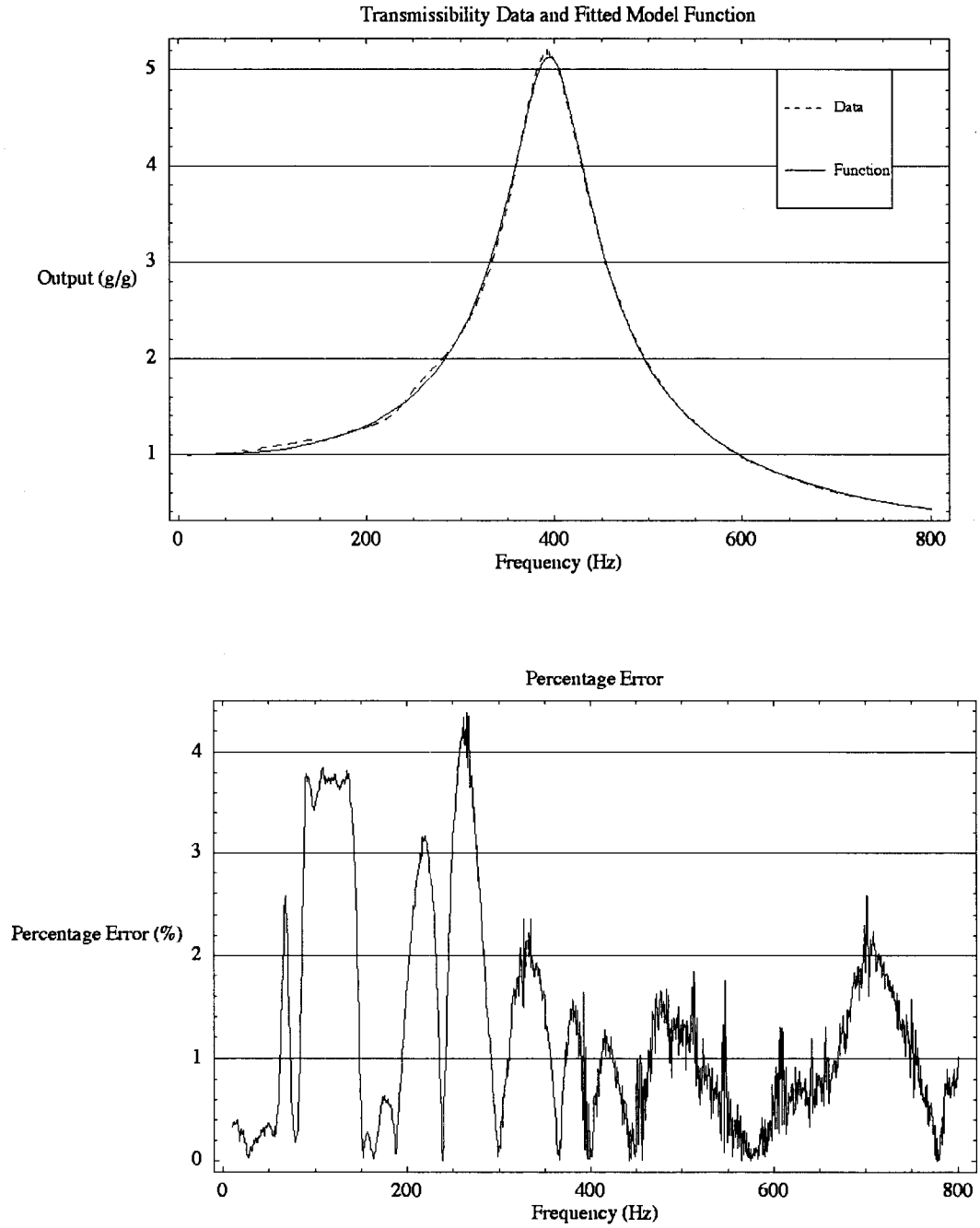

Figure D 34: 12V Sweep Quadratic Viscoelastic Model Plots

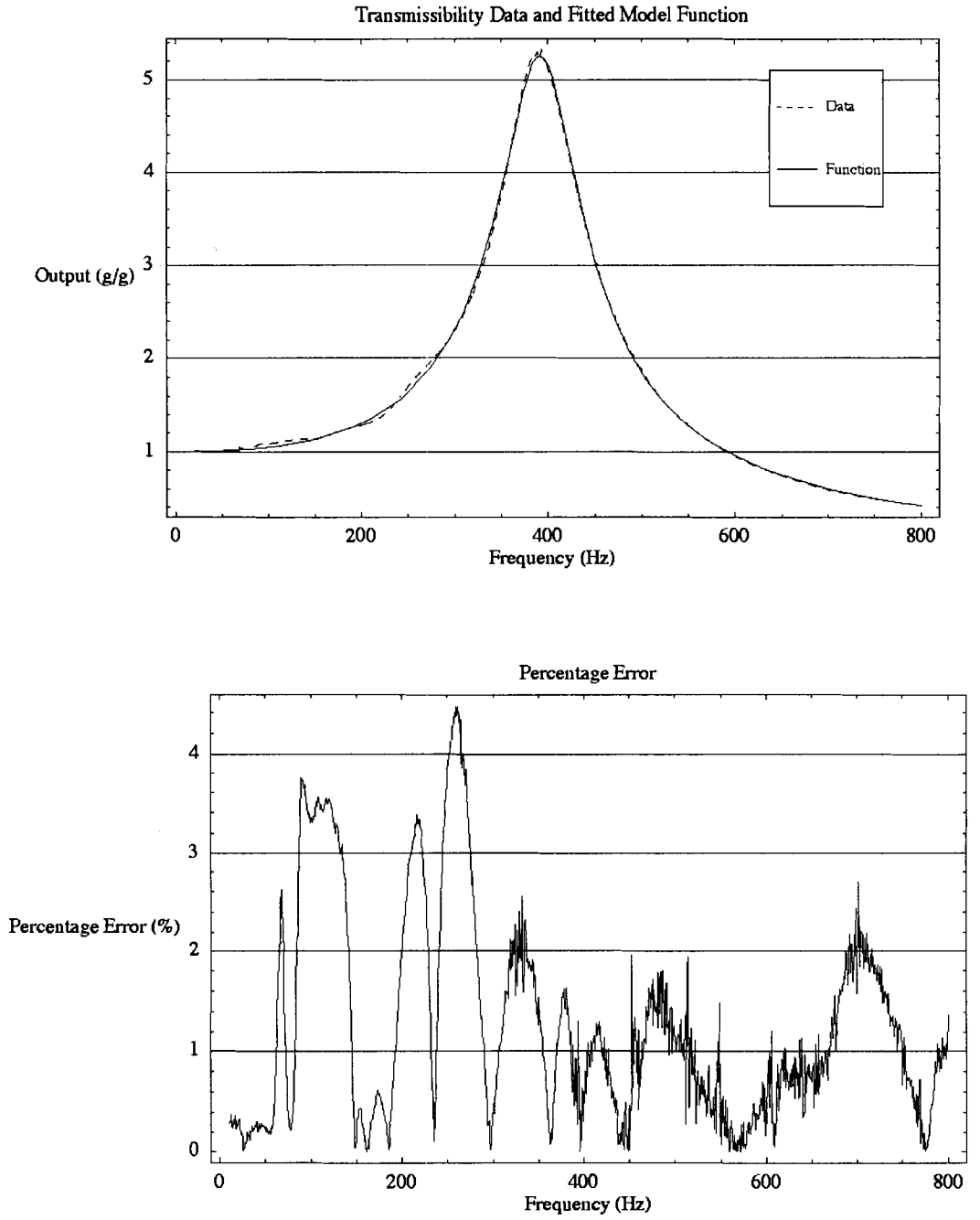

Figure D 35: 14V Sweep Quadratic Viscoelastic Model Plots

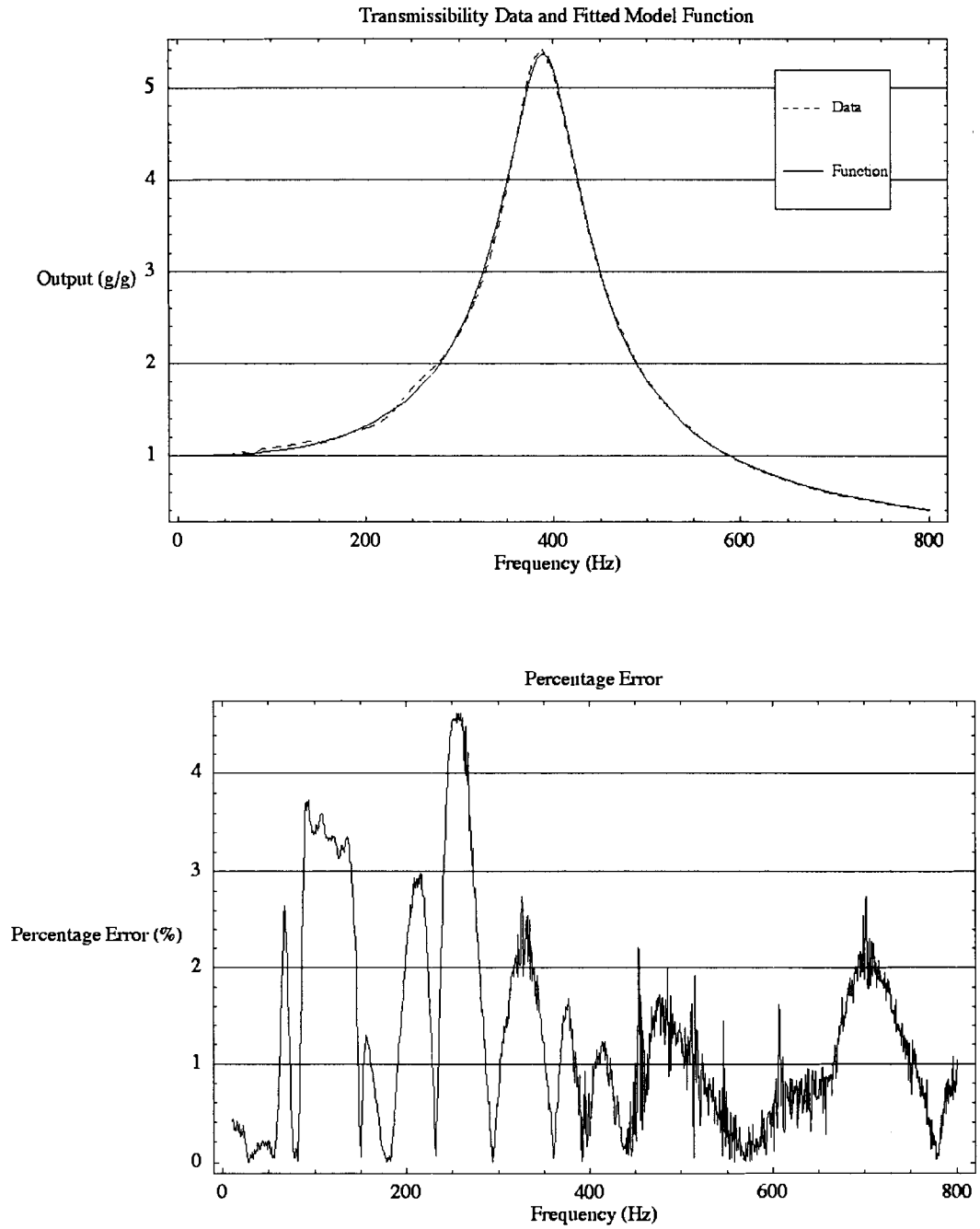

Figure D 36: 16V Sweep Quadratic Viscoelastic Model Plots

REFERENCE LIST

[1] R. Shoureshi and T. Knurek, "Automotive applications of a hybrid active noise and vibration control," *IEEE Control Syst.Mag.(USA),* vol. 16, pp. 72, 1996/12.

[2] P. Feraboli and A. Masini, "Development of carbon/epoxy structural components for a high performance vehicle," *Compos.B, Eng.(UK),* vol. 35B, pp. 323, 2004.

[3] Z. Zeng, Y. Zhang, Y. Zhou and Q. Jin, "Superplastic forming of aluminum alloy car body panels," *Mater.Sci.Forum (Switzerland),* vol. 475-479, pp. 3025, 2005.

[4] K. Shibata, T. Iwase, H. Sakamoto, F.H. Dausinger, B. Hohenberger, M. Muller, A. Matsunawa and N. Seto, "Process stabilization by dual focus laser welding of aluminum alloys for car body," *Proc.SPIE - Int.Soc.Opt.Eng.(USA),* vol. 5121, pp. 376, 2003.

[5] A. Seeds, D. Nardini and F. Cassese, "Aluminum takes center stage at Ferrari [spot welding]," *Mach.Des.(USA),* vol. 61, pp. 85, 1989/10/12.

[6] M.H. Sjoerdsma, "Controlling Structure Borne Noise in Automobiles using Magnetorheological Components," 2005.

[7] D. Hrovat, "Survey of advanced suspension developments and related optimal control applications," *Automatica,* vol. 33, pp. 1781, 1997/10.

[8] B. Riley and M. Bodie, "An adaptive strategy for vehicle vibration and noise cancellation," *Proceedings of the IEEE 1996 National Aerospace and Electronics Conference NAECON 1996 (Cat.no.96CH35934),* vol. vol.2, pp. 836, 1996.

[9] S.P. Nagarkatti, "Keeping the noise down in confined spaces," *IEEE Potentials,* vol. 20, pp. 29, 2001/08.

[10] T.J. Sutton and S.J. Elliot, "Active control of interior road noise," *Noise Vib.Worldw.(UK),* vol. 25, pp. 14, 1994/02.

[11] B. Rafaely and S.J. Elliott, "$H_2/H_{\∞}$ active control of sound in a headrest: design and implementation," *IEEE Trans.Control Syst.Technol.(USA),* vol. 7, pp. 79, 1999/01/.

[12] Jung-Shan Lin and I. Kanellakopoulos, "Nonlinear design of active suspensions," *Proceedings of the 34th IEEE Conference on Decision and Control (Cat.no.95CH35803),* vol. vol.4, pp. 3567, 1995.

[13] R.A. Williams and A. Best, "Control of a low frequency active suspension," *International Conference on Control '94 (Conf.Publ.no.389),* vol. vol.1, pp. 338, 1994.

[14] R.S. Sharp, "Variable geometry active suspension for cars," *Comput.Control Eng.J.(UK),* vol. 9, pp. 217, 1998/10.

[15] M. Appleyard and P.E. Wellstead, "Active suspensions: some background," *IEE Proc., Control Theory Appl.(UK),* vol. 142, pp. 123, 1995/03.

[16] J. Li and W.A. Gruver, "An electrorheological fluid damper for vibration control," *Proceedings.1998 IEEE International Conference on Robotics and Automation (Cat.no.98CH36146),* vol. vol.3, pp. 2476, 1998.

[17] H.R. O'Neill and G.D. Wale, "Semi-active suspension improves rail vehicle ride," *Comput.Control Eng.J.(UK),* vol. 5, pp. 183, 1994/08.

[18] A. Titli, S. Roukieh and E. Dayre, "Three control approaches for the design of car semi-active suspension (optimal control, variable structure control, fuzzy control)," *Proceedings of the 32nd IEEE Conference on Decision and Control (Cat.no.93CH3307-6),* vol. vol.3, pp. 2962, 1993.

[19] S. Sassi, K. Cherif and M. Thomas, "On the design and testing of a smart car damper based on electro-rheological technology," *Smart Mater Struct,* vol. 12, pp. 873-880, 2003.

[20] S. Rakheja and S. Sankar, "Vibration and shock isolation performance of a semi-active `on-off' damper," *Trans.ASME, J.Vib.Acoust.Stress Reliab.Des.(USA),* vol. 107, pp. 398, 1985/10.

[21] H. Douville, "An approach using active structural acoustic control for the reduction of structure-borne road noise," 2003.

[22] G.Y. Zhou, "Shear properties of a magnetorheological elastomer," *Smart Mater.Struct.(UK),* vol. 12, pp. 139, 2003/02.

[23] M. Lokander and B. Stenberg, "Performance of isotropic magnetorheological rubber materials," *Polym.Test.(UK),* vol. 22, pp. 245, 2003.

[24] A. Albanese and K.A. Cunefare, "Smart fabric adaptive stiffness for active vibration absorbers," *Proc.SPIE - Int.Soc.Opt.Eng.(USA),* vol. 5383, pp. 490, 2004.

[25] A.J. Margida, K.D. Weiss and J.D. Carlson, "Magnetorheological materials based on iron alloy particles," *Proceedings of the 5th International Conference on Electro-Rheological Fluids, Magnetorheological Suspensions and Associated Technology,* pp. 544, 1996.

[26] J.M. Ginder, M.E. Nichols, L.D. Elie and J.L. Tardiff, "Magnetorheological elastomers: properties and applications," *Proc.SPIE - Int.Soc.Opt.Eng.(USA),* vol. 3675, pp. 131, 1999.

[27] L. Borcea and O. Bruno, "On the magneto-elastic properties of elastomer-ferromagnet composites," *J.Mech.Phys.Solids,* vol. 49, pp. 2877-2919, DEC. 2001.

[28] G.Y. Zhou, "Complex shear modulus of a magnetorheological elastomer," *Smart Mater Struct,* vol. 13, pp. 1203-1210, 2004.

[29] D.I.G. Jones, *Handbook of viscoelastic vibration damping,* Chichester; New York: J. Wiley, 2001.

[30] G.Y. Zhou and Z.Y. Jiang, "Deformation in magnetorheological elastomer and elastomer-ferromagnet composite driven by a magnetic field," *Smart Mater.Struct.(UK),* vol. 13, pp. 309, 2004/04.

[31] PCB Piezotronics, "Accelerometer, ICP®: 353B03 Datasheet," 2002.

[32] M.R. Jolly, J.D. Carlson and B.C. Munoz, "A model of the behavior of magnetorheological materials," *Smart Mater.Struct.(UK),* vol. 5, pp. 607, 1996/10.

[33] J.M. Ginder, W.F. Schlotter and M.E. Nichols, "Magnetorheological elastomers in tunable vibration absorbers," *Proc.SPIE - Int.Soc.Opt.Eng.(USA),* vol. 4331, pp. 103, 2001.

[34] A. Occhiuzzi, M. Spizzuoco and G. Serino, "Experimental analysis of magnetorheological dampers for structural control," *Smart Mater.Struct.(UK),* vol. 12, pp. 703, 2003/10.

[35] M. Yalcintas and Heming Dai, "Vibration suppression capabilities of magnetorheological materials based adaptive structures," *Smart Mater.Struct.(UK),* vol. 13, pp. 1, 2004/02.

[36] G.Y. Zhou and J.R. Li, "Dynamic behavior of a magnetorheological elastomer under uniaxial deformation: I. Experiment," *Smart Mater.Struct.(UK),* vol. 12, pp. 859, 2003/12.

[37] G.Y. Zhou and Z.Y. Jiang, "Dynamic deformation in MR elastomer driven by magnetic field," *Proc.SPIE - Int.Soc.Opt.Eng.(USA),* vol. 5053, pp. 603, 2003.

[38] T. Teratani, K. Kuramochi, H. Nakao, T. Tachibana, K. Yagi and S. Abou, "Development of Toyota Mild Hybrid System (THS-M) with 42V PowerNet," 2003, pp. 3-10 vol.1.

[39] A. Williams, "Power on the move," *IEE Review,* vol. 50, pp. 38-41, 2004.

[40] N. Mohan, T.M. Undeland and W.P. Robbins, *Power electronics: converters, applications, and design,* Hoboken, NJ: John Wiley & Sons, 2003.

[41] R.W. Erickson, *Fundamentals of power electronics,* New York: Chapman & Hall, 1997.

[42] N. Kawasaki, H. Nomura and M. Masuhiro, "A new control law of bilinear DC-DC converters developed by direct application of Lyapunov," *IEEE Trans.Power Electron.(USA),* vol. 10, pp. 318, 1995/05.

[43] F. Chen and X.S. Cai, "Design of feedback control laws for switching regulators based on the bilinear large signal model," *IEEE Trans.Power Electron.(USA),* vol. 5, pp. 236, 1990/04.

[44] R. Leyva, L. Martinez-Salamero, H. Valderrama-Blavi, J. Maixe, R. Giral and F. Guinjoan, "Linear state-feedback control of a boost converter for large-signal stability," *IEEE Trans.Circuits Syst.I, Fundam.Theory Appl.(USA),* vol. 48, pp. 418, 2001/04.

[45] V.M. Nguyen and C.Q. Lee, "Indirect implementations of sliding-mode control law in buck-type converters," 1996, pp. 111-115 vol.1.

[46] Chao-Cheng Wu and Chung-Ming Young, "A new PWM control strategy for the buck converter," 1999, pp. 157-162 vol.1.

[47] Shoei-Chuen Lin and Ching-Chih Tsai, "Adaptive voltage regulation of PWM buck DC-DC converters using backstepping sliding mode control," 2004, pp. 1382-1387 Vol.2.

[48] J. Mahdavi, A. Emadi and H.A. Toliyat, "Application of state space averaging method to sliding mode control of PWM DC/DC converters," *IAS '97.Conference Record of the 1997 IEEE Industry Applications Conference Thirty-Second IAS Annual Meeting (Cat.no.97CH36096),* vol. vol.2, pp. 820, 1997.

[49] V. Utkin, "Variable structure systems with sliding modes," *Automatic Control, IEEE Transactions on,* vol. 22, pp. 212-222, 1977.

[50] V.I. Utkin, "Sliding mode control in dynamic systems," 1993, pp. 2446-2451 vol.3.

[51] V.I. Utkin, *Sliding modes and their application in variable structure systems,* Moscow: Mir Publishers, 1978.

[52] V.I. Utkin, *Sliding modes in control and optimization,* Berlin ; New York: Springer-Verlag, 1992.

[53] K.D. Young, V.I. Utkin and U. Ozguner, "A control engineer's guide to sliding mode control," *Control Systems Technology, IEEE Transactions on,* vol. 7, pp. 328-342, 1999.

[54] H. Sira-Ramirez, "Sliding motions in bilinear switched networks," *IEEE Trans.Circuits Syst.(USA),* vol. CAS-34, pp. 919, 1987/08.

[55] H.J. Sira-Ramirez, "Switched control of bilinear converters via pseudolinearization," *IEEE Trans.Circuits Syst.(USA),* vol. 36, pp. 858, 1989/06.

[56] V.I. Utkin, J. Guldner and J. Shi, *Sliding mode control in electromechanical systems,* London ; Philadelphia, PA: Taylor & Francis, 1999.

[57] C.W. De Silva, *Control sensors and actuators,* Englewood Cliffs, N.J.: Prentice Hall, 1989.

[58] Measurements Group Inc., "Precision Strain Gages: CEA-06-240UZ-120 Datasheet," 1998

[59] A.W. Burton, "Active vibration control in automotive chassis systems", *Computing & Control Engineering Journal*, vol. 4, no. 5, pp. 225-232, October 1993.

[60] Powersim Inc., "http://www.powersimtech.com"

[61] M. Jolicoeur, J. Roumy, S. Vanreusel, D. Dionne, H. Douville, B. Boulet, H. Michalska, P. Masson and A. Berry, "Reduction of structure-borne noise in automobiles by multivariable feedback," in 2005, pp. 1397-1402.